2018

Optimization Of Nuclear Magnetic Resonance Spectroscopy Methods For Measuring Protein Hydration In Reverse Micelles

Christine Jorge
University of Pennsylvania, christineajorge@gmail.com

Optimization Of Nuclear Magnetic Resonance Spectroscopy Methods For Measuring Protein Hydration In Reverse Micelles

Abstract
Water is fundamental to all aspects of protein function including folding, stability, catalysis, and dynamics. The unique characteristics of water make it the ideal solvent for supporting life but also make it incredibly difficult to study. While much has been learned about the role of water in protein function, a site resolved understanding of these interactions has remained elusive thereby leaving a large hole in the biophysical puzzle. Experimental techniques that provide a site-resolved view of protein hydration without mutation of the protein are necessary to understand the thermodynamic role of water on protein function. It has been shown that the combination of Nuclear Magnetic Resonance (NMR) spectroscopy and encapsulation of proteins within the core of reverse micelles can satisfy these requirements. The goal of this thesis is to apply and expand upon currently established techniques to make it generally applicable to all protein systems. First, previously established methods were used to examine the internal hydration patterns of staphylococcal nuclease variants with internal ionizable groups. The results demonstrate that water penetrates the hydrophobic core to stabilize buried ionizable groups. This study illustrates the utility of NMR detected hydration measurements for longstanding biophysical questions. Next, two methods to reduce data collection times were implemented for hydration dynamics measurements. This necessary time savings provides a platform for assessing the reproducibility and precision of NMR derived hydration measurements. A new data fitting method that allows for quantitative hydration dynamics measurements of protein regions generally contaminated by hydrogen exchange is introduced. Finally, one of the remaining artifacts associated with hydration dynamics measurements detected by NMR is addressed: hydrogen exchange relayed artifacts. This was accomplished by developing experiments to decouple the relaying spin and applying a new data fitting method. These methods allow for the first site and time resolved study of protein hydration in the absence of artifact is presented. These techniques introduced were applied to Ubiquitin encapsulated in AOT reverse micelles. The majority of slowed waters reside in concave regions of the protein surface. This suggests surface curvature is one of the contributing factors for the slowing of hydration waters. The experiments presented demonstrate the utility of using NMR for measuring protein-water interactions. The work presented expands and improves upon existing methodologies and provides a framework for artifact free site resolved measurement of protein water-interactions in all protein systems.

Degree Type
Dissertation

Degree Name
Doctor of Philosophy (PhD)

Graduate Group
Biochemistry & Molecular Biophysics

First Advisor
A. J. Wand

Keywords
NMR, NOE, Protein Hydration, Reverse Micelles

Subject Categories
Biophysics

OPTIMIZATION OF NUCLEAR MAGNETIC RESONANCE SPECTROSCOPY METHODS FOR MEASURING PROTEIN HYDRATION IN REVERSE MICELLES

Christine Jorge

A DISSERTATION

in

Biochemistry and Molecular Biophysics

Presented to the Faculties of the University of Pennsylvania

in

Partial Fulfillment of the Requirements for the

Degree of Doctor of Philosophy

2018

Supervisor of Dissertation

_____

A. Joshua Wand, PhD.

Benjamin Rush Professor of Biochemistry and Biophysics

Graduate Group Chairperson

_____

Kim A. Sharp, Ph.D.

Associate Professor of Biochemistry and Biophysics

Dissertation Committee

Kim A. Sharp, PhD., Associate Professor of Biochemistry and Biophysics (Committee Chair)
Ronen Marmorstein, PhD., George W. Raiziss Professor in Biochemistry and Molecular Biophysics
Feng Gai, PhD., Edmund J. and Louise W. Kahn Endowed Term Professor of Chemistry
Nathaniel V. Nucci, Ph.D., Assistant Professor in Molecular & Cellular Biosciences and Physics & Astronomy

OPTIMIZATION OF NUCLEAR MAGNETIC RESONANCE SPECTROSCOPY METHODS FOR MEASURING PROTEIN HYDRATION IN REVERSE MICELLES

For my mother… because nothing I have ever accomplished could have been done without you.

ACKNOWLEDGMENTS

I find this section extremely difficult to write. As I was nearing the end of my high school education I didn't even think I would get into college, let alone go through the PhD process. The unraveling of events from undergrad through graduate school has taken a mountain of people; far too many for me to possibly acknowledge in this one section. In that vein, I wish to thank the people that have had the most direct impact on my path. I offer my sincerest apologies to anyone I may have forgotten in this list.

First and foremost, I would like to thank my thesis mentor Josh Wand. Over the past several years in his lab I have learned more than I could have ever imagined possible. The intellectual freedom his lab fosters has put good use to my stubborn tenacity and I leave his lab with the confidence that I can figure out most problems put in front of me. I would also like to thank Nathaniel Nucci for helping me through the extremely steep learning curve of NMR, protein hydration, and most importantly navigating the Wand Lab and graduate school. I would like to thank Kathy Valentine, Sabrina Bedard, and Li Liang for keeping the lab alive. I must offer my deepest gratitude to Matt Stetz who has become my go-to person for troubleshooting, pulse sequence and NMR questions, and bouncing ideas off of. I'd like to acknowledge Bryan Marques with whom I have navigated this entire process nearly hand-in-hand with. And finally to the entire Wand/Tommos Lab members past and present including Cecilia, John, Vonni, Igor, Ellen, Vignesh, Yao, Kyle, Starla, Brian, Evan, Shannen, Sravya, and Nikki. I would like to thank my thesis committee members, Drs. Kim Sharp, Ronen Marmorstein, Feng Gai for helpful discussion. And of course to the ladies in the BMB office that really keep everything in the department running smoothly – Ruth, Angie, Kelli, and Sanjukta specifically.

I must also offer my deepest gratitude to my undergraduate research advisor Ewan McNay. If not for Ewan I would not have known research was an option, and I definitely would not have applied to graduate school without his continued encouragement and support.

And finally to all of the people that have kept me sane (and sometimes insane) over the past 10 years. My family, though relatively small, is the greatest source of support I could ever imagine. My mother, to whom this is dedicated, is the most amazing person I know and I am so grateful to have her as my mother. To my grandmother and Mikey for always being there for me and believing in me. To significant others past and present; Dan, Jiah, and Kenny who have put up with the neurotic and crazy person that I am. I must personally thank Natie who through grad school and climbing has become one of my best friends. To all the friends, dirtbags, f***-ups I know that I have chilled, partied, boated, climbed, boarded, biked with etc. – who have (either knowingly or unknowingly) helped keep me sane and have taught me more about life than academics ever could. And last, but not least, I must acknowledge the tiny human named Case. You are brilliant, adorable, fun, sweet, and stubborn as a mule. You have the entire world at your disposal and I can't wait to see the things you do. I hope that if I can do anything in this life it is to teach you how to be brave, do something that scares you every day, and to tackle every obstacle head-on. If you do that you will have everything you will ever desire.

ABSTRACT

OPTIMIZATION OF NUCLEAR MAGNETIC RESONANCE SPECTROSCOPY METHODS FOR MEASURING PROTEIN HYDRATION IN REVERSE MICELLES

Christine Jorge

A. Joshua Wand

Water is fundamental to all aspects of protein function including folding, stability, catalysis, and dynamics. The unique characteristics of water make it the ideal solvent for supporting life but also make it incredibly difficult to study. While much has been learned about the role of water in protein function, a site resolved understanding of these interactions has remained elusive thereby leaving a large hole in the biophysical puzzle. Experimental techniques that provide a site-resolved view of protein hydration without mutation of the protein are necessary to understand the thermodynamic role of water on protein function. It has been shown that the combination of Nuclear Magnetic Resonance (NMR) spectroscopy and encapsulation of proteins within the core of reverse micelles can satisfy these requirements. The goal of this thesis is to apply and expand upon currently established techniques to make it generally applicable to all protein systems. First, previously established methods were used to examine the internal hydration patterns of staphylococcal nuclease variants with internal ionizable groups. The results demonstrate that water penetrates the hydrophobic core to stabilize buried ionizable groups. This study illustrates the utility of NMR detected hydration measurements for

longstanding biophysical questions. Next, two methods to reduce data collection times were implemented for hydration dynamics measurements. This necessary time savings provides a platform for assessing the reproducibility and precision of NMR derived hydration measurements. A new data fitting method that allows for quantitative hydration dynamics measurements of protein regions generally contaminated by hydrogen exchange is introduced. Finally, one of the remaining artifacts associated with hydration dynamics measurements detected by NMR is addressed: hydrogen exchange relayed artifacts. This was accomplished by developing experiments to decouple the relaying spin and applying a new data fitting method. These methods allow for the first site and time resolved study of protein hydration in the absence of artifact is presented. These techniques introduced were applied to Ubiquitin encapsulated in AOT reverse micelles. The majority of slowed waters reside in concave regions of the protein surface. This suggests surface curvature is one of the contributing factors for the slowing of hydration waters. The experiments presented demonstrate the utility of using NMR for measuring protein-water interactions. The work presented expands and improves upon existing methodologies and provides a framework for artifact free site resolved measurement of protein water-interactions in all protein systems.

TABLE OF CONTENTS

LIST OF TABLES

LIST OF FIGURES

Chapter 1: Introduction

Protein Hydration

Water is necessary for life, and it is generally accepted that water contributes to many aspects of protein function including structure and folding, stability, dynamics, and catalysis (1-16). As the biological solvent water has been the subject of extensive study for decades; research spans from simple atomistic details of water structure and hydrogen bonding networks through small molecule interactions to large macromolecular complexes (17-29). Despite this, the knowledge of interactions between protein and water have remained elusive due to lack of experimental methods that provide site and time resolution of native protein.

Several aspects of water that make it flexible enough to support life also make it incredibly difficult to study. Water is a small molecule (2.8 Å) and has very rapid rotational and translational motions (1-2 ps in bulk, 10-100 ps at interface) (9) which requires experimental techniques with resolution on the ps time scale. Furthermore, water is ubiquitous with a typical biochemical sample containing 10^4-10^7 times more water molecules than protein molecules. A typical biochemical protein sample will have two different types of water that behave differently; the hydration layer which consists of 2-3 water layers surrounding the protein (28, 30-37), and the bulk aqueous phase. Though distinct, the water molecules can readily exchange in and out between hydration waters and bulk solvent. Furthermore the population of the hydration layer relative to bulk solvent is incredibly small making the deconvolution of these two species difficult using most spectroscopic techniques. Finally the hydrogen bonding patterns of water are extremely dynamic and make water a very unique molecule. Water is normally involved

in four intermolecular hydrogen bonds in a tetrahedral geometry though this is highly dynamic (9). The number of hydrogen bonding partners, the angles and lengths of the hydrogen bonds, and the number of protons attached to a given oxygen atom are highly variable (38, 39). This variability depends on many factors of the local environment including temperature, solute hydrophobicity, solute size and curvature, and local charges (17, 21, 23, 26, 30, 38, 40-42). While no experimental techniques can address all of these problems simultaneously, a collective understanding of protein hydration in a global sense has been accomplished through piecewise analysis of many different studies.

One of the most studied aspects of water on protein function is through the hydrophobic effect. The term, coined by Kauzmann in 1959, describes the favorable entropic gain attributed to desolvation of hydrophobic molecules (43-45). It has been implicated as the major driving force in protein folding and stability (*i.e.,* burial of hydrophobic amino acids in the hydrophobic core of the protein) (46-50). The hydrophobic effect raises important questions regarding protein-protein recognition and the motions of the hydration layer (51). Studies have suggested that interfaces responsible for protein binding have slowed hydration dynamics relative to the rest of the protein hydration shell and contribute to thermodynamics of macromolecular interactions (5, 39, 52). To understand the role of the hydration layer on macromolecular recognition it is necessary to understand what features of the protein slow hydration waters.

In addition to surface waters, buried waters have been shown to contribute to different aspects of enzyme function (25, 53-55). Internal water molecules can serve structural roles by hydrogen bonding to the protein backbone. Waters present in active sites of

enzymes act as hydrogen bonding scaffolds, H^+ donors, and are essential for catalysis(56-59). Buried polar groups and ionizable groups play key roles in enzyme catalysis and energy transduction and are generally solvated (60, 61). Membrane proteins have been shown to have water wires that facilitate H^+ and e^- transfer through the protein to facilitate signal transduction(57). A precise understanding of how these waters contribute to protein function require a site resolved view of native protein hydration dynamics. The surface of a protein is topologically and chemically heterogeneous, thus precluding predictions of the hydrogen bonding patterns surrounding the protein (46). The protein surface is decorated with charged and polar residues which will affect the local hydrogen bonding pattern of water to protein (19, 23, 62). Hydrophobic regions of the protein surface will be devoid of hydrogen bonded water. The local surface curvature will affect the local geometry of water hydrogen bonding partners (41, 63, 64). This contrasting behavior has led to models of both hydrophilic and hydrophobic hydration. Results from the study of the water-hydrogen bond network around small molecules suggest that the hydrogen bond network is not disturbed around hydrophilic molecules, but form ice-like structures around hydrophobic molecules (9, 18, 27, 65-68). Chandler has described the contrasting behavior of the hydrophobic effect around small versus long length scales (46) (69). In small molecules the hydrogen bond network of water isn't broken, but rather rearranged. Around larger hydrophobic regions >1 nm in length the hydrogen bonds must be broken resulting in dewetted vapor-like interfaces. It is clear that the heterogeneous nature of the protein surface precludes ability to predict the thermodynamic contribution

of water to the protein. Experimental measures are necessary to understand the intricate interplay between water and the protein surface.

Many techniques have described the global nature of the hydration layer, but a site-resolved understanding is lacking. Amongst these, neutron scattering studies have shown that protein dynamics are quenched in the absence of water, and that at least 2-3 layers of hydration water are needed to restore movement (70). The hydration layer is generally thought to consist of the first 2-3 layers surrounding the protein, but other studies have suggested much longer hydration shells (33). Neutron scattering, x-ray scattering, infrared spectroscopy and magnetic relaxation dispersion have shown that the hydration layer surrounding the protein is slowed relative to bulk. The estimation of the degree to which the hydration layer is slowed varies from two times to two fold slower than bulk (17, 30, 33, 34, 71-78). The degree to which the water is slowed in the hydration shell varies across the protein surface and will depend on the local environment. In order to understand the characteristics of the protein surface that result in slowing of waters a site resolved view of water dynamics is necessary.

The majority of site-resolved investigations of water have been from X-ray crystallographic studies or molecular dynamics studies. X-ray crystallography has provided a wealth of knowledge about the locations of water, but offers no insight into either hydration dynamics or protein dynamics (37, 79, 80). Similarly, comparisons of the same protein under different crystallographic conditions have shown that waters at the protein surface vary considerably and maybe artifactual (52). Molecular dynamics (MD) simulations have provided the majority of our understanding of the behavior of these

hydration waters; however, the lack of experimental evidence makes simulation data difficult to interpret (21, 81). Similarly, due to the complex nature of water, computational water models have proven to be insufficient to define the role of hydration on protein function. It remains unclear as to what aspects of local density, hydrogen bonding patterns, or rotational and translational motion of the water are the predominant forces in affecting protein dynamics. As such over 400 different water models for MD simulations have been reported (82). Experimental methods such as Overhauser dynamic nuclear polarization (83-86) (87) and tryptophan fluorescence (36, 88) provide site and dynamic resolution of hydration, but only report on one region of the protein. These methods also require mutation for the incorporation of probes which may alter the local hydration of a protein. While these techniques offer site resolution they are insufficient to describe the entire protein surface and offer little insight into the collective role of water on protein function. Additionally, these techniques measure the different relaxation rates of the incorporated probe which is highly sensitive to local environment. Therefore, for partially solvent exposed sites the protein itself is capable of affecting these measurements.

Nuclear magnetic resonance (NMR) spectroscopy methods have also been used to probe the motions of hydration waters (53, 89-93). These methods take advantage of the dipolar interaction between nearby spins via the nuclear Overhauser effect (NOE). NMR spectroscopy is unique in that it allows for site-specific resolution of dynamical processes. Unfortunately several aspects of the behavior of bulk water have resulted in numerous seemingly insurmountable artifacts and has restricted this approach to bound

structural waters. (31, 75, 93). However, recent technological and methodological advancements have shown that these artifacts can be overcome by encapsulating proteins within the hydrophilic core of a reverse micelle. The goal of this thesis is to expand and improve upon these methodologies to develop a framework for artifact free site resolved measurement of protein-water interactions of all protein systems.

NMR for protein hydration

Over 30 years ago Wüthrich and coworkers identified that the dynamics of protein water interactions can be measured by through space dipolar interactions between the protein and water spins via the nuclear Overhauser effect (NOE) (94). The NOE can be measured in the laboratory (NOE) or the rotating (ROE) (95-98) reference frames. While the NOE and ROE are mechanistically similar their cross relaxation rates (σ^{NOE} and σ^{ROE}, respectively) differ as a function of the correlation time between the protein and water molecules. Dynamic information about the water interaction requires taking the ratio of the NOE and ROE cross relaxation rates(89-91, 93). Due to the different reference frames of detection they have varied dependence on their spectral density functions (Equations 1-1 and 1-2)

$$\sigma^{NOE} = q[6J(2\omega_o) - J(0)] \quad 1\text{-}1$$

$$\sigma^{ROE} = q[3J(\omega_o) - 2J(0)] \quad 1\text{-}2$$

Where $q=\gamma^4\hbar^2/10[\mu_o/(4\pi)]^2 = 5.7\text{x}10^{10}$ Å^6 s^{-1}. Therefore q is a prefactor of fundamental constants including the gyromagnetic ratio of protons(γ) and Plank's constant ($\hbar$), ω is the proton Larmor frequency, and $J(\omega)$ is the power spectral density function defined:

$$J(\omega) = \int C(t)\cos(\omega t)\,dt \qquad 1\text{-}3$$

where C(t) is the sum of the auto-correlation function of the magnetic dipole-dipole interactions between two spins that are sufficiently close.

$$C(\mathrm{t}) = \sum_j \left\langle \frac{Y_{20}(r_j(0))}{r_j^3(0)} \frac{Y_{20}(r_j(\mathrm{t}))}{r_j^3(\mathrm{t})} \right\rangle \qquad 1\text{-}4$$

Where $Y_{20}(r_j) = \sqrt{5/16\pi} \times (3\cos^2\theta - 1)$ is a normalized spherical harmonic function that describes the internuclear vector between the two adjacent spins. The auto-correlation function (Equation 1-4) is therefore a convolution of the time dependence and length and orientation of the two interacting spin systems, and makes a detailed interpretation of the σ^{NOE} and σ^{ROE} challenging.

The cross-relaxation rates as a function of the interaction time between protein and water by using the "rigid sphere" model are illustrated in Figure 1-1. This assumes no internal motion between the protein and water bond vector and can be described by the reduced spectral density function:

$$J(\omega) = \frac{1}{r^6} \frac{\tau_c}{1 + \omega^2 \tau_c^2} \qquad 1\text{-}5$$

Where r is the distance between two interacting spins and τ_c includes the mean residence time (τ_{res}) of water and the rotational correlation time of the solute (τ_m) such that $1/\tau_c = 1/\tau_{res} + 1/\tau_m$. This model does not describe any diffusional or rotational movement of water about the protein and is therefore insufficient to extract τ_{res}.

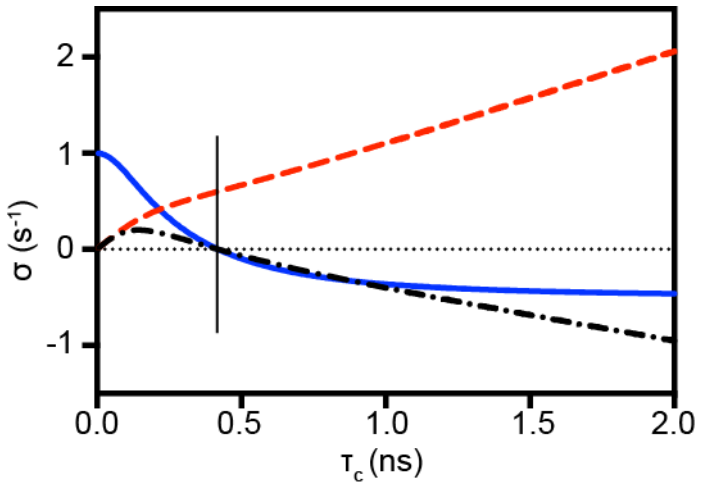

Figure 1-1: A) Dependence of σ^{NOE} in black and σ^{ROE} in red as a function of the correlation time of the protein water interaction. The ratio of the σ^{NOE} and σ^{ROE} rates is shown in blue. The black vertical line shows the zero-crossing point (356) for the NOE, which is the minimum detectable correlation time for the intermolecular NOE. Fortuitously, the dynamics of water in the reverse micelle core is on this time scale of the null of the NOE, which reduces the expected range of the NOE from 0 to -0.5. Rates were calculated using a distance of 2.2 Å, a magnetic field strength of 14.6 T (^{1}H 600 MHz) and the rigid rotor spectral density (Equation 1-5).

Although it is difficult to de-convolute the many contributions to the intermolecular NOE (dipole-dipole coupling strength and rate of modulation of the dipole-dipole vectors), there are several models that describe the use of the intermolecular NOE to extract information about rotational and translation motions of water near the surface of a protein. One of the earlier models developed by Ayant *et al*. describes the relaxation between nearby spins located on spherical particles of unequal radii undergoing uniform translational (99) and rotational diffusion (100). Brüschweiler and Wright used this formulation (among others) to demonstrate the inherent difference between intra- and inter-molecular NOEs and to present an approximate theoretical range of timescales of

differential water dynamics (101). More recently, Halle expanded upon this model to incorporate non-uniform diffusion of water near the protein surface eventually concluding that the intermolecular protein-water NOE near the surface of the protein is contaminated by bulk solvent (102); however, this has been shown to not necessarily be the case(103).

The simpler rigid sphere model does not factor in internal dynamics of the protein but is sufficient to describe the waters movements ranging from fast (300ps) to slow (~10ns). In the case of slow water with a long correlation time the $\sigma^{NOE}/\sigma^{ROE}$ ratio approaches -0.5, whereas fast water approaches an NOE/ROE ratio of 1 (Figure 1-1)(93). The rotational correlation time of water in the reverse micelle is substantially slowed relative to bulk aqueous solvent and the τ_c will never be slower than the null crossing point for the NOE. Therefore, in the reverse micelle, slow water NOE/ROE ratios approach -0.5, and fast water approaches 0.

The cross relaxation rate can be calculated from the peak height intensity (I_{NOE}) of the crosspeak. The intensity takes the form:

$$I_{NOE} = A_o[e^{-R_1\tau_m}(1-e^{-\sigma_{NOE}\tau_m})] \quad 1\text{-}6$$

$$I_{ROE} = A_o[e^{-R_{1\rho}\tau_m}(1-e^{-\sigma_{ROE}\tau_m})] \quad 1\text{-}7$$

Where A_o is a prefactor, R_1 is the longitudinal relaxation rate, and τ_m is the mixing time. The ROE crosspeak intensity follows the same form but undergoes transverse ($R_{1\rho}$) relaxation (94).

There are three types of magnetization transfer that can be detected by the NOE (Figure 1-2). The first is the direct dipolar magnetization transfer from the protein to the water,

which is the measurement of interest. The second is the case of direct hydrogen exchange between the protein and water. The observed cross relaxation rate takes the form(94, 104):

$$\sigma_{NOE}^{obs} = \sigma_{NOE} + k_{ex} \quad 1\text{-}8$$

$$\sigma_{ROE}^{obs} = \sigma_{ROE} + k_{ex} \quad 1\text{-}9$$

Where k_{ex} is the hydrogen exchange rate. The sign of σ^{NOE} and k_{ex} term are both negative, whereas the sign of σ^{ROE} is positive (104). Magnetization transfer from direct hydrogen exchange can easily be detected because the ROE crosspeak is the same sign as the NOE (i.e. same sign as the diagonal peak) (95, 105).

The third type of magnetization transfer occurs from exchange-relayed NOEs. In this case water will exchange hydrogens with a labile protein proton, which can then undergo an NOE transfer to a nearby protein. This type of exchange is spectrally indistinguishable from direct dipolar magnetization exchange and is the major artifact of NOE-detected hydration experiments (106, 107). The $\sigma^{NOE}/\sigma^{ROE}$ ratio in the case of exchange-relayed NOEs is always artificially lower than in the absence of relay. Often times this causes the $\sigma^{NOE}/\sigma^{ROE}$ ratio to be outside of the theoretical limits. The observed cross-relaxation rate is defined by(94, 95, 108):

$$\sigma_{NOE}^{obs} = \sigma_{NOE} + (\Sigma k_{ex} \bullet \sigma_{NOE}^{intra}) \quad 1\text{-}10$$

$$\sigma_{ROE}^{obs} = \sigma_{ROE} + (\Sigma k_{ex} \bullet \sigma_{ROE}^{intra}) \quad 1\text{-}11$$

Depending on the question of interest NOE and ROE experiments at multiple mix times can be measured to solve for the σ^{NOE} and σ^{ROE}.

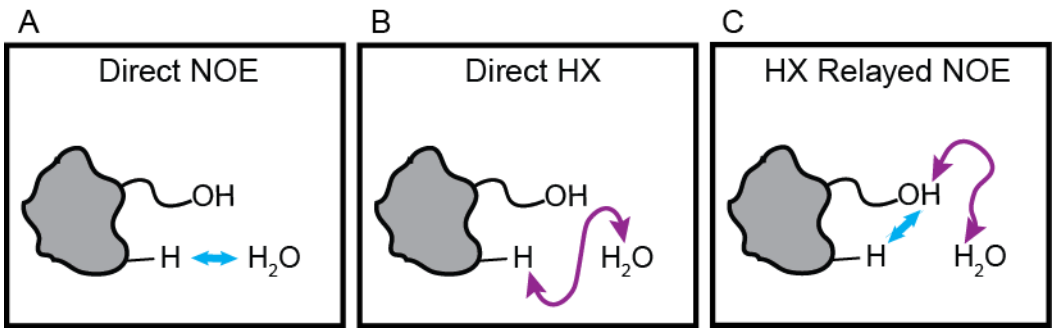

Figure 1-2: Examples of magnetization transfer that can be detected by the NOE experiment. A) Direct NOE between a protein-proton and a water proton as shown by a straight blue arrow. B) Direct hydrogen exchange between a protein-proton and a water proton as a purple curved arrow. C) Exchange relayed process where a protein-proton (e.g. hydroxyl) directly hydrogen exchanges with water (curved purple arrow) followed by direct dipolar exchange (straight blue bar) to a nearby protein-proton (e.g. amide)

While the $\sigma^{NOE}/\sigma^{ROE}$ ratio appears to be an excellent means to understand hydration dynamics near the surface of the protein, there are three issues that arise when attempting to analyze these experiments in aqueous solution. The first is poor dipolar contact between protons on the protein surface and water protons: although hydration layer waters are slowed relative to bulk by up to 2 orders of magnitude (23), they are often still too fast to detect quantifiable intermolecular NOEs (93). The second issue is potential contamination from bulk water on the NOE (102): the overwhelming presence of waters in the bulk solvent has been thought to diminish the distance dependence of the intermolecular NOE from r^{-6} to r^{-1}. The third issue is possible contamination of the protein-water NOE from chemical exchange: magnetization can be transferred from hydrogen-exchanged protons from nearby exchangeable groups (nearby waters, backbone amides, or side chains) leading to potential ambiguities in the assignment of a true

protein-water NOE (75, 93). Fortunately, these issues can (mostly) be alleviated upon encapsulating the protein within a reverse micelle.

Reverse Micelles

Reverse micelles (RM) are spontaneously forming particles composed of a nano-pool of water, an amphiphilic surfactant shell, and bulk organic solvent (Figure 1-3) (109-116). The reverse micelle can encapsulate small molecules or large biological macromolecules, or can be made in the absence of solute ("empty"). The size of non-protein containing reverse micelles can be controlled by the molar ratio of the water-to-surfactant, W_o, added to the sample. Stable reverse micelle samples have been made with W_o ranging from 2-60 consisting of water pools ranging from 1.7-28 nm (68, 114). It has also been shown that proteins maintain their hydrated radii upon encapsulation within a reverse micelle with excess water being sequestered into "empty" reverse micelles (117). Protein encapsulation in reverse micelles was initially intended to overcome the tumbling limit in NMR by replacing bulk aqueous solvent with a low viscosity organic solvent (118-123). The utility of the reverse micelle has led to its use in many biophysical studies including metastable proteins, lipid anchored proteins, membrane proteins, and hydration measurements (119, 124-129).

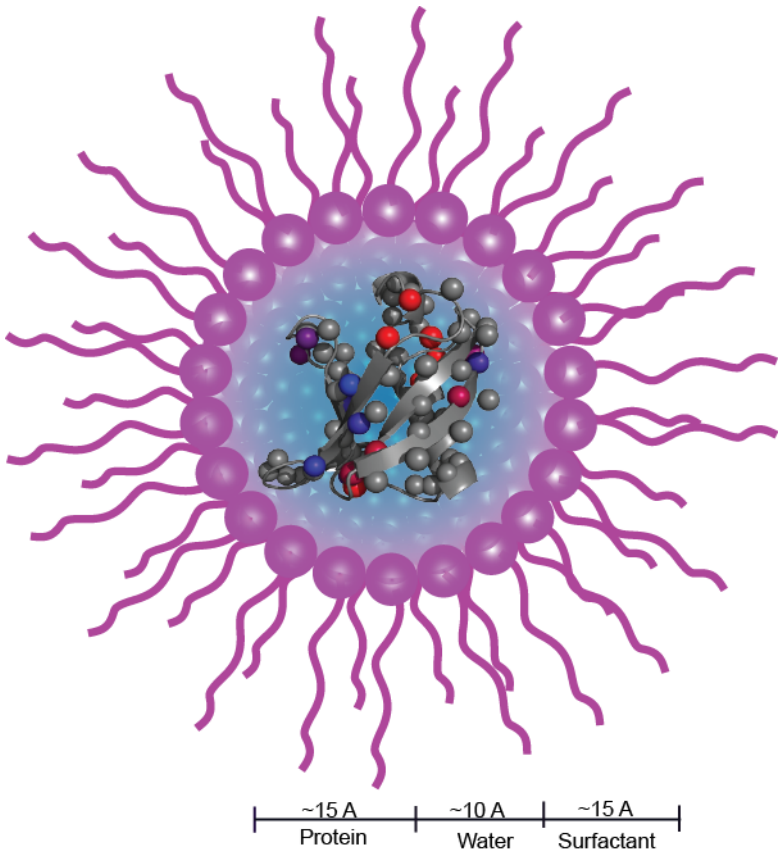

Figure 1-3: Schematic of Ubiquitin encapsulated in a reverse micelle.

There are several benefits of reverse micelle encapsulation for the detection of protein-water NOE's. Nucci *et al.* showed that nearly all artifacts associated with measuring protein-water interactions via the NOE in aqueous solution are removed when employed in the reverse micelle (125). "Empty" RMs have been extensively used to study water pool behavior and hydrogen bond behavior of water networks (27, 40, 42, 66, 68, 111, 130-132). Confinement from the reverse micelle slows the rotational and translational motions of water by up to two orders of magnitude. The water surrounding the surfactant interface is the most motionally restricted suggesting that water is highly influenced by

ions and charged surfaces. The water motions become more bulk like as it extends into the core of the water pool (27, 38, 40, 66, 68, 130). Reverse micelles with higher water loadings have water with more bulk-like behavior. The overall slowing of water in the reverse micelle serves to amplify the intermolecular NOE. Additionally, encapsulation of protein removes bulk water while maintaining the native hydration shell of the protein (117). This maintains the local nature of the NOE as there is no bulk aqueous solvent to contaminate distance dependence of the intermolecular NOE. And finally, the hydrogen exchange rates are slowed approximately two orders of magnitude in the reverse micelle (125, 133). This slowing removes contamination from direct hydrogen exchange of amides and greatly reduces exchange relayed processes occurring from side chains. Thus the reverse micelle is the ideal system to study protein and water interactions via the NOE.

Biophysical studies of proteins in reverse micelles require that the protein maintains its native structure upon encapsulation (134). Retention of structure is easily identified by using NMR spectroscopy. Fidelity of protein structure and dynamics can be inferred through careful analysis of ^{15}N-HSQC spectra. The NMR chemical shifts of protons and amides are exquisitely sensitive to slight differences in local chemical environment. In order to assess foldedness the amide peaks must maintain good spectral dispersion. Generally, comparison of protein chemical shifts in bulk aqueous solution and reverse micelles show RMSD's <0.1 ppm (117, 135). Several structures of proteins encapsulated in the reverse micelle have been determined and are shown to have backbone C_α RMSD's <1 Å relative to in bulk aqueous solution (119, 127, 136). It is also necessary that the

protein remains stable over the course of several weeks during experimental collection. These requirements generally require optimization of encapsulation conditions for each protein studied.

Numerous surfactant mixtures have been developed that encapsulate proteins reproducibly and stably (115, 116). Bis-(2-ethylhexyl)sulfosuccinate (AOT) is an anionic surfactant and is, to date, one of the most studied reverse micelle systems. AOT reverse micelles do not require the addition of any secondary surfactants or co-surfactants and is therefore simple to use. However NMR spectroscopy shows that many proteins in AOT, while dissolved in the aqueous core, are unfolded (137). Ubiquitin is one of the few exceptions to this and generally encapsulates in AOT reverse micelles at high concentrations (~300μM), and remains folded and stable for >6 months. A second surfactant system has also been widely studied. Cetyltrimethylammonium bromide (CTAB) is a cationic surfactant that can either form micelles or reverse micelles depending on the type of co-surfactant used. CTAB requires a cosurfactant that is generally a short chain primary alcohol such as hexanol to form a reverse micelle. The tertiary mixture makes it slightly more difficult to initially optimize but encapsulates a wide range of proteins (113, 114, 122, 138). Recently, a new quaternary surfactant system was introduced consisting of lauryldimethylamine-N-oxide (LDAO) and decylmonoacylglycerol (10MAG) and slight amounts of primary alcohol cosurfactants. The 10MAG/LDAO is a zwitterionic surfactant mixture resulting in a much lower charge density than the other anionic and cationic surfactants (AOT and CTAB respectively). The 10MAG/LDAO mixture is capable of encapsulating the widest range of proteins, but

due is the most difficult to optimize (135). Nearly all proteins can be encapsulated in one of these surfactant mixtures.

Dissertation Objectives

It is clear that the interactions between protein and water are incredibly complex. In order to understand the thermodynamic contributions of water to different aspects of protein function it is necessary to obtain a site and time resolved view of protein hydration in native folded protein. And yet, due to the complex behavior of water, experimental techniques that provide this level of resolution are lacking. The revival of NMR methods to measuring protein-water interactions via the NOE by encapsulating proteins in the interior of reverse micelles has contributed a great step forward in this endeavor. While promising, technological advancements will facilitate the broader application of these methods. The goal of this dissertation is to improve and expand upon on these methods to make it generally applicable to all protein systems. The following chapters are organized in order of increasing complexity in the measurements ranging from binary observations of internal waters to analysis of protein hydration across the chemically heterogeneous protein surface.

Chapter 2 employs NOE hydration measurements to ask a straightforward biophysical question: do water molecules enter the hydrophobic core of proteins to stabilize internal ionizable groups? Although a seemingly simple question, the lack of techniques that provide site resolution have made this a highly debated subject. In fact, many experimental and computational methods including X-ray crystallography, MRD, and MD simulations have been employed to tackle this question. To date, many of the

findings of these experiments contradict each other and therefore no clear consensus has been reached. As only detection of internal waters are required, and no dynamics are necessary to address this question the NOE experiments collected were relatively fast. This allowed for the study of several different mutants in a tractable amount of time.

Chapter 3 addresses the issue of reproducibility and level of quantitation derived from NOE hydration measurements. Data collection times were reduced by implementing non-uniform sampling of three-dimensional experiments or by decreasing the dimensionality of the experiments from three to two dimensions. Minimal signal-to-noise requirements for quantitative reproducibility were determined. Finally, a new data fitting method was implemented that allows for the quantitative hydration dynamics of buried waters, or waters in the absence of artifact from exchangeable side-chains. This method of data fitting does not require assumptions about the relaxation of the protein-water interaction and is therefore more robust than previously established methods. The established method centers on collecting a buildup of experimental mix times and therefore would not be feasible if not for the reduction in data collection times.

Finally, Chapter 4 tackles one of the long-standing limitations of protein-hydration measurements via the NOE: contamination from hydrogen exchange. A new pulse sequence was implemented that decouples side-chain hydroxyls removing exchange relayed contributions. A more rigorous data fitting method is implemented that allows for quantitative hydration dynamics measurements without artifact even for sites in the proximity of exchangeable side chains. The experiments and data analysis are more

intensive than those presented in Chapters 2 and 3, but provide a means to measure protein-water NOE's without contamination through the entire protein.

A distillation of the methods introduced in the subsequent chapters is provided in Appendix A. A general protocol for how to prepare samples and the data collection necessary for these measurements is provided. Additionally, the different data fitting methods described in the following chapters is reiterated with their general use and applicability. It is the hopes of the writer that anyone reading this thesis will be able to implement these experiments in order to address fundamental questions of protein hydration.

Chapter 2: Water Penetration into the hydrophobic core of staphylococcal nuclease stabilizes internal ionizable residues

This work began as a collaboration with Dr. Bertrand Garcia Moreno from Johns Hopkins University.

Abstract

Water-penetration into the core of proteins serves many structural and functional roles. Understanding protein-water interactions has been a long sought after goal but has remained elusive due to the complicated behavior of water. Solution nuclear magnetic resonance (NMR) spectroscopy via the nuclear Overhauser effect (NOE) in combination with reverse micelle encapsulation of proteins has been proposed as a means to characterize these interactions. This method was used to measure hydration dynamics measurements of a hyper stable variant of staphylococcal nuclease SNase Δ+PHS and two mutants SNase Δ+PHS/I92E and SNase Δ+PHS /V66E. These mutants have ionizable groups buried within the hydrophobic core of the SNase β-barrel. These ionizable groups have large dielectric constants relative to what is normally predicted within the protein. Water penetration into the hydrophobic core of the protein, as well as protein relaxation have been proposed as ways of stabilizing these internal ionizable groups. Protein hydration detected via the NOE validates crystallographic waters in all variants of Snase. Additionally, the SNase mutants show detectable hydration throughout the entire hydrophobic cavity. Protein dynamics on both the fast (ps-ns) and slow (μs-ms) timescale are largely unchanged between the SNase Δ+PHS parent protein and mutants. This suggests that water penetration into the core of the protein acts to stabilize the buried ionizable groups.

Introduction

Water penetration into the core of proteins serves many structural and functional roles (53, 91, 93, 139). Internal water molecules generally interact with buried polar groups that do not have a hydrogen-bonding partner (61, 140, 141). They serve to reduce the energetic cost of transferring polar atoms into the hydrophobic interior(61). Most buried ionizable groups are typically in their hydrated state, and just a few water molecules are needed to solvate charges effectively in the proteins low dielectric environment. As many buried polar and ionizable groups are essential for catalysis and energy transduction including H^+ transport and redox reactions water molecules play a central role in these fundamental protein processes (57, 59, 140, 142, 143).

However, despite the fundamental role of internal waters on protein function a site resolved understanding of the number and location of water molecules has proved to be elusive. Water molecules are extremely small and are generally disordered with rapid rotational motion (141). Additionally, water penetration is often accompanied by changes in the conformation and dynamics of the protein. This makes experimental measures of internal hydration difficult to obtain for all but the most rigid waters. Many experimental and computational methods have been employed to study internal waters, but each with its own sets of caveats. X-ray crystallography provides the precise location of rigid water molecules (80), however, positionally disordered waters will not provide sufficient electron density and cannot be detected by crystallography. This is especially true in room temperature crystallography where generally no water molecules can be detected. Cryogenic crystal structures detect more internal waters but whether those are present at room temperature or if they result from cryogenic artifacts is still largely debated (79,

144). Molecular dynamic (MD) simulations have provided the majority of our understanding of internal waters; however, the lack of experimental evidence makes simulation data difficult to interpret (24). Fluorescence (88) and dynamic nuclear polarization measurements (145) offer site resolution and dynamics information about local waters but require mutation of the protein. Neutron and x-ray scattering methods (77), as well as magnetic relaxation dispersion (MRD) (31, 75) methods provide dynamic information but report only on global averaging thereby precluding a site resolved understanding of the water positioning. An experimental method that provides site resolution of native protein at room temperature is necessary in order to understand that number and position of these internal water molecules.

NMR spectroscopy is a useful tool for characterizing interactions between water and protein. Wüthrich and coworkers proposed NMR methods for the study of site-resolved hydration dynamics more than two decades ago (91).This method measures protein-water interactions using through-space intermolecular dipolar magnetization exchange processes between protein and water via the nuclear Overhauser effect in the laboratory (NOE) (94) and rotating (ROE) (96) reference frames. NMR spectroscopy also detects protein dynamics across multiple timescales (146). Unfortunately in bulk aqueous solution NMR spectroscopy of protein-water NOE's is limited by the same difficulties that plague other experimental techniques. Rapid water motions, exchange between the aqueous layer and bulk solution, and rapid hydrogen exchange rates restrict these measurements to only a few completely buried and rigid waters. Recently, Nucci *et al.* showed that encapsulating proteins into the hydrophilic core of a reverse micelle removes

all of the artifacts associated with measuring hydration via the NOE in bulk aqueous solution (125).

Reverse micelles (RMs) are nano-scale complexes that spontaneously form in the presence of appropriate amphipathic surfactant molecules, bulk organic solvent, and minimal aqueous solvent (109). Protein structure and native hydration layer are maintained inside of the protective core of reverse micelles (119). Sequestration of protein in the aqueous core of RMs provides several advantages in the measurement of hydration dynamics. Firstly, confinement from the RM slows both hydration water and hydrogen exchange behavior (68, 133.). The combined slowing of water and hydrogen exchange means that the movements of the hydration layer are within the range of detection by NMR and that artifacts from hydrogen exchange are minimized. Additionally, the removal of bulk water prevents exchange in and out of the hydration layer (102). These benefits allow for detection of protein-water interactions of dynamic waters, as well as the detection of water molecules that are still partially solvent accessible. Furthermore, protein hydration and protein dynamics can be measured in the same sample that allow the interplay between water penetration and dynamic changes to be studied simultaneously.

The present study uses NMR spectroscopy to measure internal hydration and protein dynamics of staphylococcal nuclease (SNase) Δ+PHS and two of its mutants (147). SNase Δ+PHS is a hyper stable pseudo-wild type variant of SNase and differs from wild type by three mutations (P177G, H124L, S128A) and deletion of a loop (residues 44-49) (24). SNase Δ+PHS has a flat stability profile (11.8kcal/mol) between pH 4.5-9. SNase Δ+PHS has a cavity within the hydrophobic core that is large enough to fit ~4 water

molecules but is generally thought to be desolvated. Many mutants have been engineered with internal ionizable groups in the hydrophobic core of the protein to study the dielectric constant of proteins in a controlled manner. Many mutants remain folded with little change to the crystallographic structure. In this present study the NOE is used to detect protein hydration in SNase Δ+PHS, and two mutants SNase Δ+PHS/I92E (148) and SNase Δ+PHS/V66E (54). Additionally, backbone dynamics are measured to asses changes in dynamics associated with each mutant. Ile92 is one of the most buried residues in SNase and its side chain is buried deep within the hydrophobic core of the β-barrel. Similarly the side chain of Val66 is also buried within the β-barrel but the residue resides on the α1 helix immediately adjacent to the β-barrel(149). Several characteristics of these mutations make them ideal for studying the dielectric constant of proteins (150). Firstly, the small cavity within the hydrophobic core in which these side chains reside offers enough room to tolerate amino acid substitutions without disrupting the side chain (151-155). Thus any change in protein structure or dynamics is a result of the presence of internal polar groups. As these mutations are non-native the protein does not have any evolutionary mechanisms in place to stabilize these charges and therefore must adapt to the change in the local environment. Previous studies have shown that the mutant proteins retain their native fold and that the buried Glus have an elevated dielectric constant of ~10 (54, 141, 148, 156-159). Whether the stabilization of the internal ionizable group and high dielectric constant are the result of water penetration or protein relaxation remains highly debated. The data presented here suggest water penetration is a dominant source of the high polarizability of the protein interior and the stabilization of

internal polarized residues with minimal changes to overall backbone dynamics or structure.

Results and Discussion

SNase encapsulation

Wild type SNase Δ+PHS and its mutants Δ+PHS/V66E and Δ+PHS/I92E stably and reproducibly encapsulate at a final concentration of 100 μM in reverse micelles composed of 60 mM, 450 mM hexanol and a W_o of 20. Under these conditions the reverse micelles are mono-dispersed ellipsoids (114). Lower concentrations of cosurfactant increase the resolution between the water and hexanol hydroxyl peak (Figure 2-1). The ^{15}N NOESY-HSQC experiments used for hydration were also analyzed to verify that the protein is not interacting with the surfactant shell. If coalescence of the water and hexanol peaks occurs then there is no way to verify that NOE's are arising from water and not from hexanol. ^{13}C-detected hydration experiments require deuterated surfactants to eliminate spectral artifacts in the methyl region. Therefore, it is important to have at least one protonated site in the surfactant that is spectrally resolved to verify no protein-surfactant interactions. All samples had a separation >100hz between the water and hexanol peaks.

Hydration measurements detected via the NOE require low pH to minimize hydrogen exchange. The NOE can detect magnetization transfer through both through space dipolar interactions as well as hydrogen exchange (92, 95, 105, 160, 161). It was previously shown that the reverse micelle slows hydrogen exchange by 2 orders of magnitude (125, 133). Thus, amide exchange is sufficiently slow in the reverse micelle to not exchange on the timescale detectable by the NOE (161). Unfortunately, titratable side chains have

exchange rates higher than amides. Side chains have exchange rate minima between pH 5-7 (162). In order to limit hydrogen exchange processes all experiments were performed at pH 5.3. The pH was verified by amide chemical shifts and by monitoring the acetate chemical shift as described previously (137).

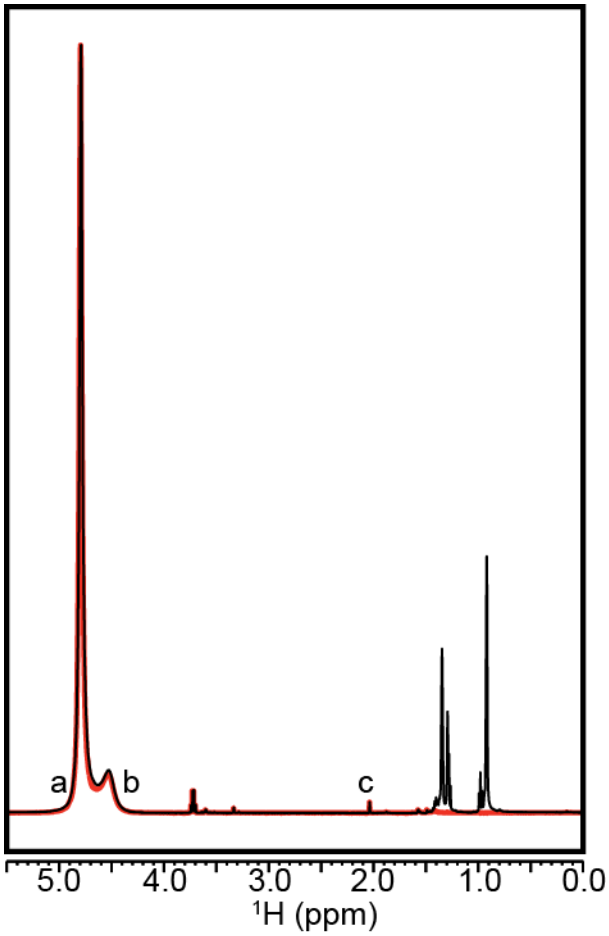

Figure 2-1: Overlay of standard 1D spectrum (black) and 1D spectrum with WET suppression (163)of SNase Δ+PHS encapsulated in CTAB/hexanol reverse micelles. Peaks that were used to assess sample stability are labeled a) water, b) hexanol, and c) acetate. Separation between the water and hexanol peaks is necessary to ensure that the protein is not interacting with the surfactant layer

Upon encapsulation spectra maintain broad dispersion of peaks, and only minimal chemical shift perturbations were observed between aqueous and reverse micelle samples. The ^{15}N-HSQC spectrum of encapsulated SNase Δ+PHS show excellent

agreement with that obtained in free aqueous solution with R^2 for chemical shift correlations of the amide ^{1}H and ^{15}N both exceeding 0.99 and chemical shift RMSDs of 0.04 ppm and 0.17 ppm for proton and nitrogen chemical shifts, respectively. The ^{13}C-HSQC of the reverse micelle is directly superimposable on the aqueous spectrum. This indicates the protein maintains its native structure under the conditions used for encapsulation. Under these conditions the reverse micelle samples remain stable for >6 months. Stability of the reverse micelle mixture was verified by periodically measuring the integral and chemical shift of the water and acetate peaks in 1D proton detected experiments. Stability of the protein was verified by 2D ^{15}N-HSQC's.

Chemical Shift Perturbations of I92E and V66E mutants

The amide cross peaks in ^{15}N-HSQC spectra are highly sensitive to the local chemical environment and therefore report on minor structural perturbations. The majority of amide peaks in both the Δ+PHS/I92E and Δ+PHS/V66E mutants do not display major chemical shift perturbations (CSPs) upon mutation suggesting general retention of the structure (Figure 2-2). Ile92 is one of the most buried residues of SNase and resides in the back of the β-barrel. The mutated Glu side chain is completely buried within the hydrophobic core. The pK_a value of the buried Glu is shifted towards neutral with a value of 8.85 (164). The stability of the I92E mutant is highly pH dependent and has a maximum stability at pH 5. As the pH is increased the Glu becomes deprotonated and the stability decreases. At pH 5.3 the buried Glu is in its protonated uncharged form, and the protein has a stability >5.5kcal/mol. The I92E mutant has a median CSP of 0.04 ppm with a mean of 0.11 ppm. There are several locations where larger CSP's occur. The β-bulge consisting of residues 18-22, and the inner part of the α1 helix consisting of

residues 61-67 show CSPs up to 1ppm. The residues that make up the β-bulge show the largest crystallographic C_α RMSDs in the crystal structures relative to wild type (144). However, these changes are slight with a <0.3Å RMSD. Additionally, these residues form a hydrogen bond network with the 4 internal water molecules that solvate the Glu carboxyl. The hydrogen bonded water network extends out toward bulk solvent. These bridging waters extend between the β-barrel and the α1 helix and are hydrogen bonded to the Ser 59:O. CSPs of the mutation site and the residue immediately preceding it can also be observed.

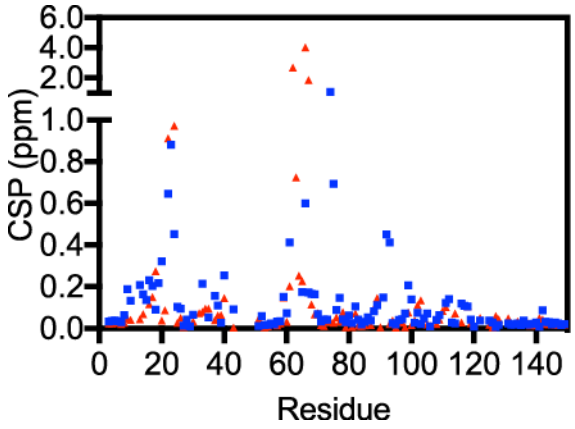

Figure 2-2: Chemical Shift perturbations for SNase Δ+PHS/I92E (blue squares) and SNase Δ+PHS/V66E (red triangles) relative to the pseudo wild-type SNase Δ+PHS parent protein.

The V66E mutation is located on the α1 helix, with its side chain buried in the β-barrel. Similar to the I92E mutant, the V66E mutant Glu has a pK_a value of 8.8 that is highly shifted toward the neutral form. At pH 5.3 the buried Glu is in its protonated uncharged form and the protein has a stability of ~5 kcal/mol. A similar pattern of CSPs can be seen in with the V66E mutant as with the I92E mutant. CSPs are identified in the β-bulge consisting of residues 18-22, and in the α1 consisting of residues 61-67. While fewer water molecules are seen crystallographically, 2 buried waters are hydrogen bonded to

residue 22 and solvate the buried Glu. A similar water network of bridging waters is also seen crystallographically. The CSPs presented here are in agreement with the crystal structures (54, 148) that have been determined previously and suggest that no large changes in the protein structure are present.

Analysis of NOESY and ROESY spectra

Protein-water interactions were measured by observing cross peaks at the water resonance of ^{15}N-resolved NOESY- and ROESY-HSQCs (Figure 2-3A and C) for amides and ^{13}C-resolved NOESY- and ROESY-HSQC's for methyls. (Figure 2-3B and D). Hydration measurements were performed on fully perdeuterated protein that was grown in 99% D_2O to replace non-labile protons with deuterons (165). This removes any intra-molecular cross-peaks from H_α protons that resonate at frequencies overlapped with water. Perdeuteration also drastically decreases the $R_{1\rho}$ relaxation rate due to the lower gyromagnetic ratio of deuterons over protons. Perdeuteration decreased the amide $R_{1\rho}$ relaxation rate to 0.04 s^{-1} from 0.11 s^{-1} in full protonated protein. This allows for the collection of ROESY spectra at longer mix times. All amide detected NOE and ROE experiments were collected with 30 ms mix times. Methyl detected experiments were collected at 40 ms mix times. The intensity of the NOE is dependent on both the distance between interacting spins and the motions of the internuclear vector (93, 94). The NOE is therefore lower in intensity for inter-molecular crosspeaks, such as those between protein and water, than in intramolecular cross peaks. Increasing the mix time allows for increased signal-to-noise and detection of interactions that have faster water motions. All protein-water interactions were assumed to have a distance of <4 Å between the interacting spins.

The cross-relaxation rate of the NOE and ROE cross peaks are dependent on the correlation time of the protein-water interaction. The correlation time is defined as the inverse sum of the molecular tumbling (τ_m) and the interaction of the protein and water bond vector. The NOE has a positive cross relaxation rate at short correlation times and then crosses zero and becomes negative for longer correlation times. This zero crossing point is 356 ps when collected on a 500MHz spectrometer. This results in a negative cross peak relative to diagonal for short interaction times and a positive cross peak relative to diagonal at longer interaction times. All NOESY cross peaks in the ^{15}N and ^{13}C-NOESY-HSQC spectra are positive suggesting long-lived protein-water interactions (Figure 2-3A and B). The rotational translational motion of water is slowed an order of magnitude in the reverse micelle relative to bulk (68). Additionally, it is known that the dynamics of water at the protein interface are slowed 1-2 orders of magnitude. The lack of negative NOESY cross peaks indicate that the dynamics of water on the surface and within the protein are substantially slow relative to bulk.

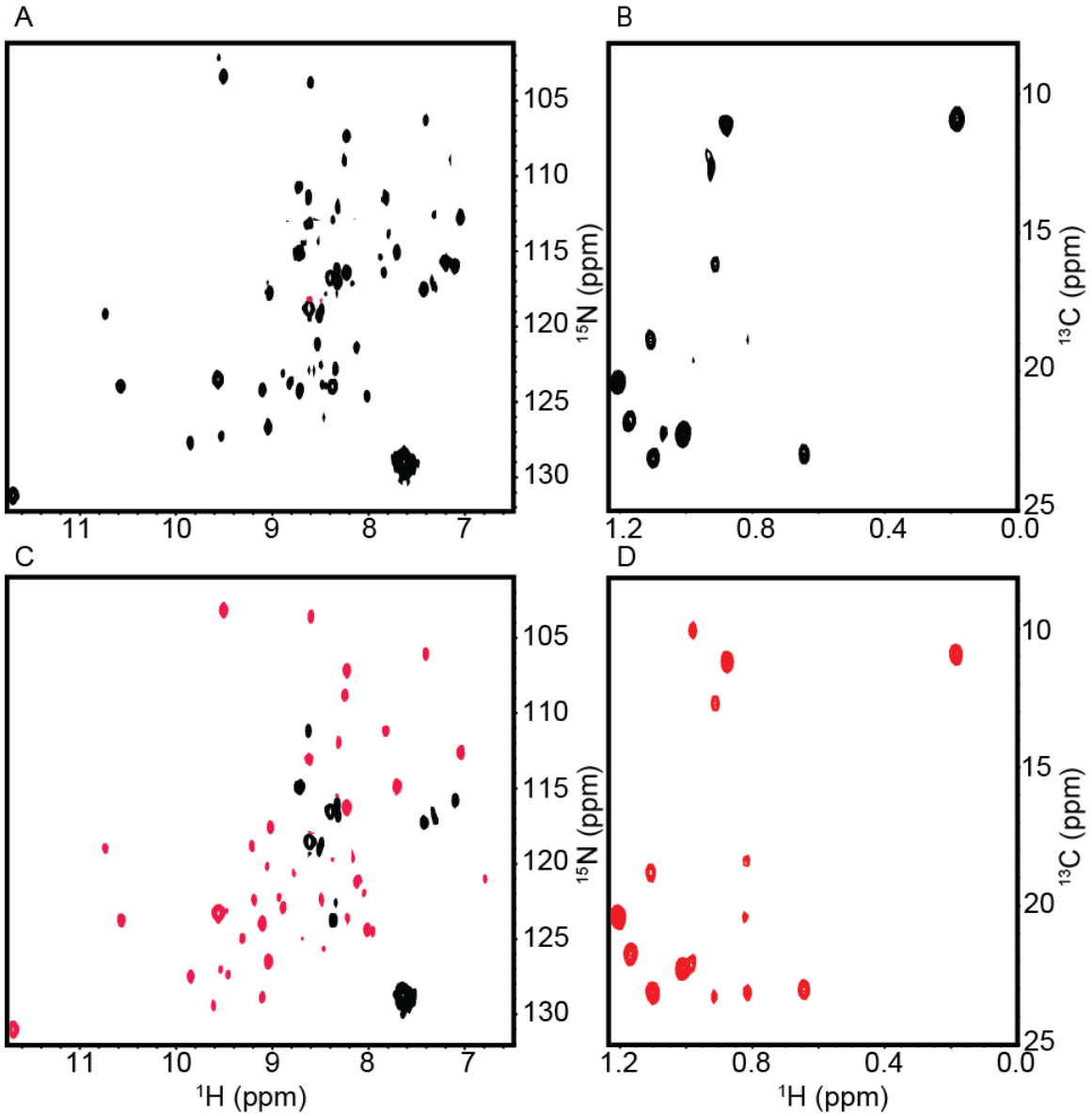

Figure 2-3: A) ^{15}N NOESY-HSQC, B) ^{13}C NOESY-HSQC, C)^{15}N ROESY-HSQC, and D) ^{13}C ROESY-HSQC spectra at the water plane of SNase Δ+PHS encapsulated in CTAB/hexanol reverse micelles. Positive and negative crosspeaks are colored black and red, respectively. No positive crosspeaks are observed in ^{15}N or ^{13}C NOESY-HSQC spectra owing to the slowed waters in the reverse micelle. Positive crosspeaks observed in ^{15}N or ^{13}C ROESY-HSQC spectra are located in disordered termini or side chains suggesting no contamination from hydrogen exchange.

In contrast to the NOE the cross-relaxation rate of the ROE is always positive, resulting in a negative cross peak relative to the diagonal. Hydrogen exchange results in a positive cross peak relative to the diagonal in the ROE spectrum. This is advantageous because it easily allows for the detection of hydrogen exchange. Therefore, only negative cross peaks in the ROESY spectra are considered to be protein-water interactions. Positive cross peaks are indicative of hydrogen exchange and are not included in our analysis. As the cross-relaxation rate of the ROE does not have a zero crossing point it is able to detect faster protein-water interactions (98). Residues that had cross peaks in the ROESY experiments but not the NOESY experiments were considered fast protein water interactions as the NOE approaches the zero-crossing point.

In SNase Δ+PHS and both mutants the majority of positive cross peaks in the ^{15}N-ROESY spectra, which are indicative of hydrogen exchange, are the disordered protein termini. An additional 2 sites, Arg81 and Lys 84, within the protein showed hydrogen exchange peaks. None of these sites are located near mutation sites. No positive cross peaks were observed in ^{13}C-detected ROESY experiments and no other hydrogen exchange peaks were observed in any of the spectra (Figure 2-3 B and D).

Hydration of SNase Δ+PHS and comparison to crystal structures

Water	H-Bond Partners	Detected Amide NOEs	Detected Methyl NOEs
WAT1	Asp77:N, Leu89:O	Lys84, Gly85, Asp89, Gln125, Thr126	Leu7:HD, Leu37:HD, Leu89:HDS
WAT2	Trp140:Nε1, Val104:O, Ala109:O	Gly107, Trp140Hε1	Val104:HG Ile133:HD
WAT3	Gly20:N, Pro42:O, Gly55:O	Phe44, Gly20	
WAT4	Glu73:Oε1, Gly96:N	Glu73, Asp95, Gly96	
WAT5	His8:O, Glu10:Oε2, Phe76:N	His8, Glu10, Phe76	
WAT6	Tyr115:N, Asn118:O, Tyr113:O	Leu38, *Val114, Gly117, Asn119	Leu38:HDS, Leu37:HD, *Val108:HGS
WAT7	Thr22:O, Asp19:O, Ser59:O	Ile18, Gly19, Asp21, Thr22, Lys63	
*Residues >4Å in flexible loop consisting of residues 111-119			

Table 2-1: Location of buried crystallographic waters and nearby protons with detectable hydration via the NOE

Cross peaks that were detected in ^{15}N and ^{13}C NOESY- and ROESY HSQC's were mapped to the cryogenic crystal structure of SNase Δ+PHS (PDB accession 3BDC). Several waters have been identified in the cryogenic crystal structures, although only 2 water molecules have been confirmed using magnetic relaxation dispersion methods (141). A list of crystallographic waters and the sites with NOEs are listed in Table 2-1 (54). One water molecule, WAT1 is hydrogen bonded to the Asp77:N and Leu89:O. Numerous cross peaks including Leu7, Leu37, and Leu89 methyls, and show NOEs to water. WAT2 is hydrogen bonded to the Trp140 indole. NOEs to water were detected on the Val104 and Ile133 methyls, Gly107 amide, and the Trp140 indole. A third buried water, WAT3, is hydrogen bonded to Gly20:N, Pro42:O, and Gly55:O. NOEs were detected to the amides of residues Phe44 and Gly20. Two water molecules WAT4 and WAT 5 are partially solvent exposed and hydrogen bonded to Glu73:Oe1 and Gly96:N, and His8:N, Glu10:Oe2, and Phe76:N respectively. NOEs to water are detected on

amides Glu73, Asp95 and Gly96 for WAT4 and His8, Glu10 and Phe76 for WAT5. Several solvent exposed waters are also identified in the active site. These waters, WAT6, are hydrogen bonded to Y115:N, N118:O, and Y113:O. The amide of Leu38, and methyls of Leu37 and Leu38 are less than <4 Å away from WAT6 and have detectable NOEs to water. Additionally, several other residues including amides Val114, Gly117, and Asn119, and methyls from Val108 also show NOEs to water. The loop making up the active site consisting of residues 111-119 is highly dynamic as assessed by H-N NOE (166) and TROSY-Hahn Echo experiments (167). This flexibility would explain the detection of NOEs to waters that are between 4-6Å away from the crystallographic water. One final cluster, WAT7 of buried waters resides within the β-bulge consisting of residues 18-22. Two water molecules are hydrogen bonded to each other and residues Thr22:O, Asp19:O, and Ser59:O. While the water molecule bound to Ser59 is detected by all crystal structures the water bound to Thr22 and Asp19 is only detected in some crystal structures. Amides immediately surrounding these waters Ile18, Gly19, Asp21and Thr22 all have NOEs to water confirming the presence of this second water molecule.

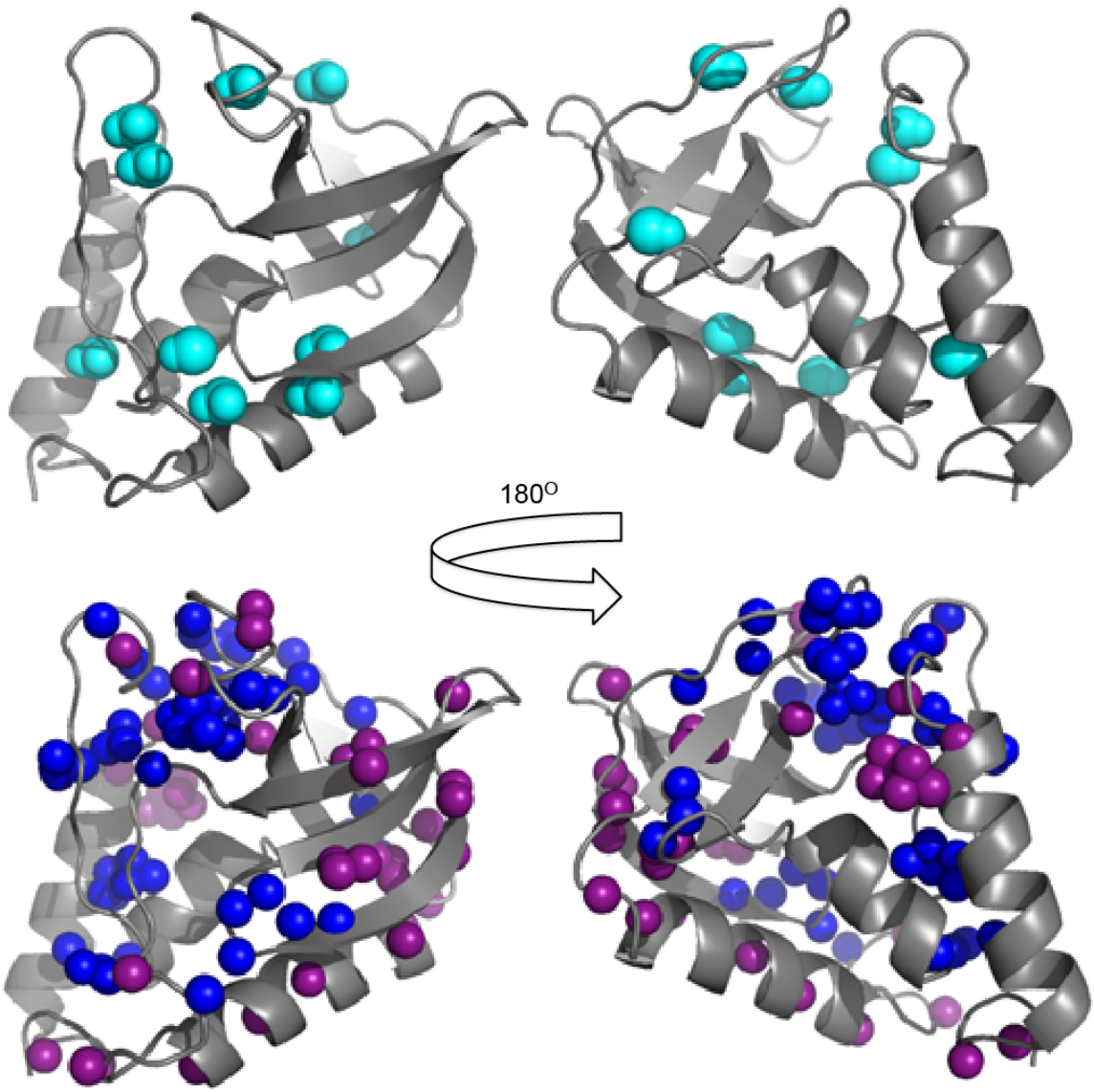

Figure 2-4: Top: Structure of SNase Δ+PHS (PDB accession code 3BDC) with buried crystallographic waters shown as blue spheres. Bottom: Structure of SNase Δ+PHS (PDB accession code 3BDC) with protons with detectable NOEs to waters illustrated as spheres. Sites that are within 4 Å of a crystallographic water are illustrated in blue, with all other sites in purple.

Despite the hydrophobic interior of the β-barrel containing a cavity large enough to hold 4 water molecules, no water NOEs are detected in the hydrophobic core. Additional NOEs to water were located on surface exposed regions of the protein. These include

amides from residues Phe61, Val17, Thr13, Leu14, Met26, Tyr29, and Lys53. While multiple crystallographic waters are present in the SNase Δ+PHS cryogenic crystal structure, only two waters, WAT1 and WAT2 are considered long lived according to MRD experiments and MD simulations (156, 157, 159, 168). No NOEs were detected on buried residues that were not near crystallographic water. All additional NOEs were located on loops and were solvent exposed. In the absence of spin diffusion the NOE has a very short r^{-6} dependence. Since all NOEs, except for those in the dynamic active site loop were under 4 Å in distance from a crystallographic water shows that the local nature of the NOE is maintained.

Hydration of I92E

The I92E mutation is one of the most buried residues in the protein and is located in the back most buried region of the β-barrel. At pH 5.3 the Glu is in its neutral, protonated form. It is part of the hydrophobic core consisting of residues Leu14, Ala17, Val23, Leu36, Val66, Ile72, and Val99. NOEs for the I92E mutant were detected for Leu14, Val23, Leu36, Val66, and Ile72. Both methyl peaks for Val99 were overlapped in the ^{13}C detected experiments and cannot be used in our analysis, and Ala17 was unable to be detected due to the choice of ILV only methyl labeling. All methyls lining the hydrophobic core have NOEs to water suggesting water penetration throughout the cavity (Figure 2-5A). This is in stark contrast to previous experimental and computational data. The I92E mutant has the largest number of waters in the cryogenic crystal structure, but doesn't have any crystallographic waters in room temperature structures (144). A total of 4 cryogenic crystallographic waters are hydrogen bonded to each other and to the Glu92 carboxyls, and Gly20, Asp19, and Thr62 carbonyls. Methyls of Leu14, Val23, Leu36,

and Val66 are within 4 Å of these crystallographic waters. However, the methyls of residue Ile72 are more than 6 Å from the nearest crystallographic water, and more than 4 Å from the Glu carboxyls. This suggests that water penetrates deep into the hydrophobic core but is disordered. These disordered waters cannot make hydrogen bonds with nearby residues that accounts for lack of crystallographically detected waters. Up to 10 putative binding sites were previously detected for SNase mutants by DOWSER (168). However, molecular dynamics simulations suggest that water molecules occupy only 5 of these sites and that on average only two water molecules are present in the cavity at any time. The findings presented here suggest that all 10 of these binding sites may be transiently occupied by water but these waters may not form the necessary hydrogen bonds to be detected by other methods. This is consistent with findings of Nguyen *et. al* (148). The NOE is capable of detecting dynamic and positionally disordered waters as long as they are within 4 Å of the detecting proton.

Hydration of V66E

Similar to the I92E mutant, all internal crystallographic waters that were detected in the SNase Δ+PHS cryogenic structure were also detected in the V66E mutant structure. Residues buried deep in the hydrophobic core have detectable NOEs to water. This includes residues Leu14, Leu36, Ile72, and Ile92. Only two waters were detected in the cryogenic crystal structure and no waters were detected in the room temperature crystal structure. Molecular dynamics simulations confirmed the presence of two water molecules, although one water molecule is more long-lived than the other (156, 168). Magnetic relaxation dispersion showed no difference in internal hydration between the

Δ+PHS and V66E mutant (141). NOEs to water can be detected by all methyls lining the cavity suggesting that water penetrates deep into the cavity (Figure 2-5B).

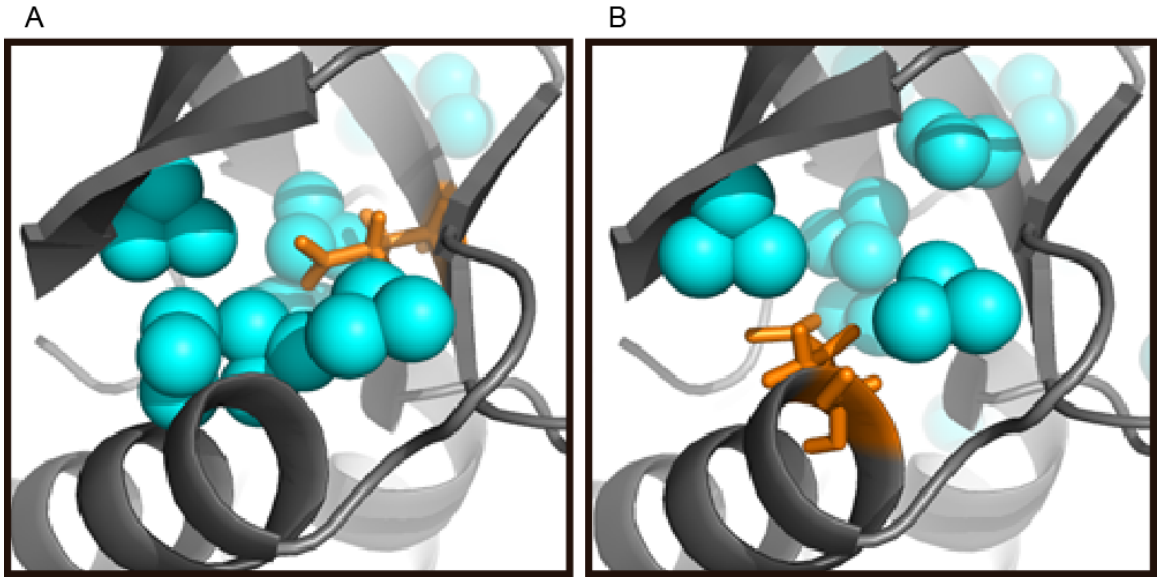

Figure 2-5: Cavity of SNase Δ+PHS/I92E (PDB accession number 5KIX) A) and SNase Δ+PHS/V66E (PDB accession number 5EGT) B). Sites with detectable NOEs to water are shown as teal spheres. The site of mutation is illustrated as orange sticks.

Comparison of protein dynamics

The increased dielectric constant of the buried Glu residues in the I92E and V66E mutants can be due to either water penetration into the core or by local structural rearrangements. The CSP data presented here are in agreement with crystallographic data suggesting that no large changes occur to the protein structure occur upon mutation. Water penetration can be coupled to changes in local unfolding or increased dynamics on the μs-ms timescale. Protein dynamics using the H-N NOE were used as a proxy to detect fast (ps-ns) motions and protein disorder (166). The ratio of the NOE is taken from experiments with and without saturation. The saturated NOE is dependent on the local fluctuations of the H-N bond vector. Ordered regions with fast dynamics have depressed

ratios and are generally less than 0.65, whereas the ratios of disordered regions invert sign. In the SNase Δ+PHS protein negative HN-NOE values were detected in disordered termini. Additionally decreased HN-NOE values were measured at the β-bulge consisting of residues 18-22, the β-turn consisting of residues 28 and 29, the truncated loop consisting of residues 37-54, and the loop consisting of residues 107-119 (Figure 2-6A). This is consistent with previously measured aqueous ^{15}N relaxation data of SNase (169). This further suggests that structure and dynamics are unaffected by reverse micelle encapsulation. Similar patterns of HN-NOE ratios were observed for both of the mutants studied. Comparisons of HN-NOE ratios between the WT and I92E mutant had a slope of 0.95, and R^2 of 0.98, and a standard deviation of 0.05. Similarly, comparisons between WT and the V66E mutant had a slope of 0.99, with an R^2 of 0.98 and a standard deviation of 0.04. Thus, no changes in protein disorder or protein dynamics on the ps-ns timescale were observed.

TROSY Hahn-Echo experiments were used to assess protein dynamics on the us-ms timescale, and are expressed as the rate of chemical exchange (R_{ex}) (167). The fastest dynamics of the WT protein R_{ex} values were greater than 20 s^{-1}. These residues were part of the β-bulge consisting of residues 18-22, the loop consisting of residues 37-54, and the loop consisting of residues 107-119 (Figure 2-6B). Similar patterns of R_{ex} were identified for the I92E mutant. Conversely, R_{ex} values for the V66E mutant are depressed for all but the loop consisting of residues 107-119. Thus, no increases in protein dynamics occur upon mutation. Molecular dynamic simulations have shown that the most common traveled route for water molecules is through passage between Ala17, Ile18, Aps19, and Ser59. Intriguingly, these protein dynamics, along with buried waters hydrogen bonded to

Thr22 and Asp19 and Ser59 are observed in all mutants as well as the wild type. Thus the flexibility of the β-bulge is required for penetration of water into the core of the protein.

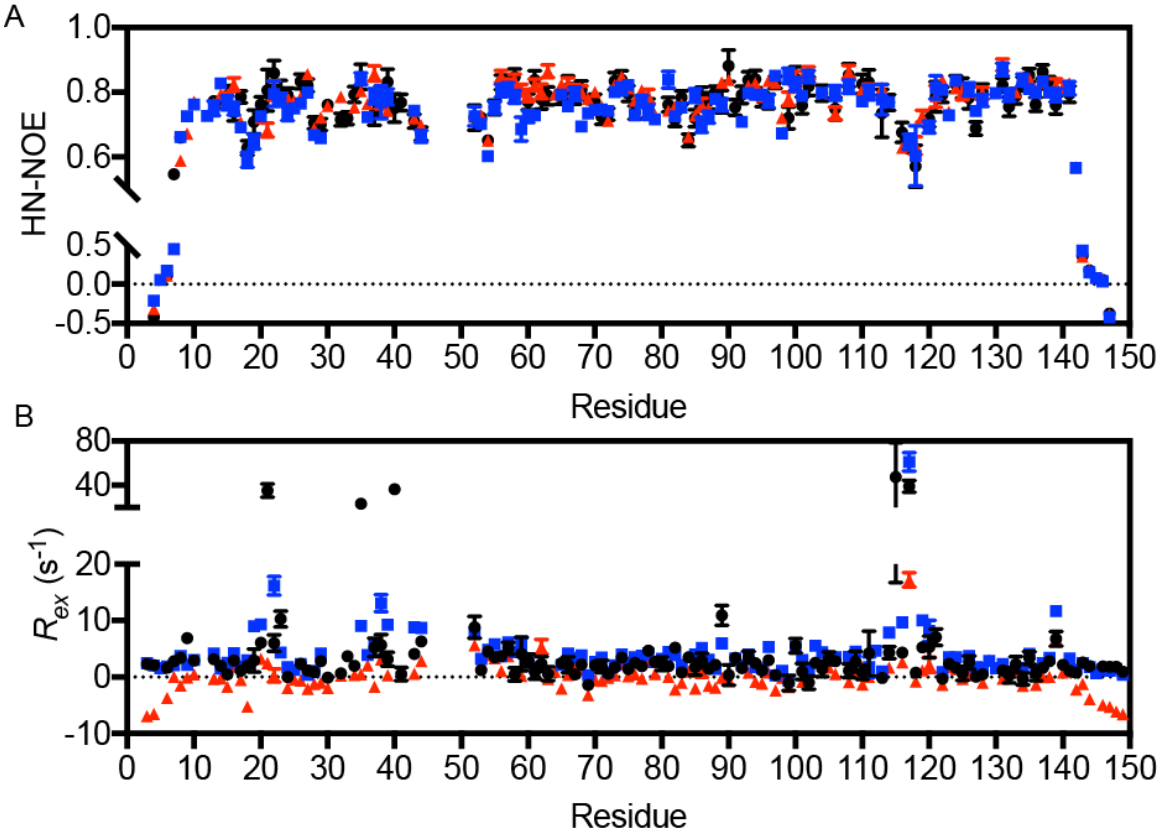

Figure 2-6: A) HN-NOE values and B) TROSY Hahn-Echo R_{ex} values for SNase Δ+PHS (black circles), SNase Δ+PHS/I92E (blue squares), and SNase Δ+PHS/V66E (red triangles).

Conclusions

The dielectric constant for ionizable groups buried in the hydrophobic core of SNase is substantially higher than what would be expected from the protein interior. Two mechanisms have been proposed to describe the increased dielectric accompanying buried ionizable group; water penetration into the hydrophobic core, and structural rearrangement of the protein. However, despite numerous experimental and computational studies there remains a longstanding debate as to whether or not water is capable of entering the hydrophobic core of proteins. This study uses reverse micelles to

investigate protein dynamics and protein-water interactions in SNase and two mutants via NMR spectroscopy.

The structure and dynamics of SNase Δ+PHS encapsulated in CTAB/hexanol reverse micelles is maintained relative to bulk solution as assessed by chemical shift perturbations, and HN-NOE and TROSY Hahn Echo experiments. The reverse micelle serves to slow the rotational and translational motions of water as well as remove exchange in and out of the hydration layer to bulk. However, despite this, the majority of residues that have detectable NOEs to water are within 4 Å of previously detected crystallographic waters or reside in solvent exposed parts of the protein exemplifying the local nature of the NOE. Three water sites have been previously identified as being slow, whereas six different buried water sites were identified by the NOE. Thus, the NOE is capable of detecting protein-water interactions on timescales faster than other methods such as room temperature crystallography and magnetic-relaxation dispersion. Even though the hydrophobic core of the WT protein is large enough to house up to four water molecules, no NOEs were detected to water in the core suggesting that no water penetrates the core in the wild type protein.

In contrast to the wild-type protein, SNase I92E and V66E mutants have detectable NOEs to water throughout the hydrophobic cavity. No major changes in chemical shift or dynamics were observed between the wild type and mutant proteins. These findings are consistent with crystallographic structures and suggest that water penetration is not coupled to any large conformational changes or local unfolding events. The largest changes in chemical shift are observed around the β-bulge consisting of residues 18-22. This region of the protein has fast R_{ex} dynamics on the us-ms timescale in both the WT

and mutant proteins. This suggests that the dynamics along the β-bulge allow for penetration of water molecules into the cavity but the lack of hydrogen binding partners within the hydrophobic core preclude burial of water in the WT protein in its native state. Upon mutation the buried Glu residues in the I92E and V66E mutants are sufficient to stabilize water molecules within the hydrophobic core. These waters are hydrogen bonded to the carboxyl side chains of the Glu residue and form a characteristic ring like structure. However, the depth of detected NOEs suggest that once the water molecule is brought into the core of the protein it is capable of transiently penetrating deep into the hydrophobic core. These transient motions are likely highly disordered and therefore not detectable by crystallography or other methods such as magnetic relaxation dispersion. The data presented here suggest that water penetration is a major factor for the high apparent dielectric constants of buried Glu residues. While slight structural rearrangements of side chains would not be detected by our measurements no large changes in protein structure or dynamics are observed upon water penetration. These findings are consistent with those hypothesized by Nguyen *et al.* who suggest that the hydrophobic core may contain many more water molecules than previously detected, and that they may not be site bound and can penetrate transiently in many locations (148). The NOE method does not require positionally ordered waters and is therefore the only method that can detect these types of dynamic interactions.

Chapter 3: Reduction of experimental time for protein-water hydration measurements using nuclear magnetic resonance spectroscopy

Most of this work was done in collaboration with Dr. Bryan Marques, previous Ph.D. candidate in the laboratory of A. Joshua Wand.

Abstract

The interaction between the surface of proteins and the three to five layers of solvating water (the hydration layer) is inarguably of utmost importance throughout all facets of biology; however, these interactions are notoriously difficult to observe in a site-specific manner without physical alterations to the studied protein. Encapsulating proteins within reverse micelles slows hydration dynamics and hydrogen exchange within the hydration layer enough such that it allows for quantification of site-specific hydration dynamics at protein surfaces via NMR nuclear Overhauser effect (NOE) spectroscopy. Through the advent of non-uniformly sampled (NUS) NMR spectroscopy, it is possible to reliably extract this information in afraction of the time. In this study, we first determine the reproducibility of hydration dynamics measurements as determined from NUS versions of the experiments and also provide criteria for outlier detection. We also extrapolate proper hydration ratios for encapsulated ubiquitin by collecting hydration dynamics experiments at multiple mixing times, a feat not possible without NUS. Finally, we introduce water-selective two-dimensional versions of the hydration experiments that further improve the efficiency with which hydration dynamics can be detected.

Introduction

The ability to measure protein-water interactions is necessary to understand the thermodynamic role solvation water plays on protein function and stability (43, 44, 46).

However, measuring these interactions has proven to be quite difficult for a number of reasons. Solution nuclear magnetic resonance (NMR) has been used to measure the dynamics of protein water interactions via the nuclear Overhauser effect (90, 91, 93). These measurements, when performed in bulk aqueous solution, have numerous artifacts that limit the ability to study protein hydration in a quantitative manner (75, 102).

We have recently shown that encapsulating proteins in the hydrophilic core of a reverse micelle (RM's) retains the native folded protein and its hydration shell while reducing the amount of water (116, 117, 119). These factors contribute to slower water and reduced hydrogen exchange (27, 133). Proteins encapsulated in RM's allow an experimental condition that is optimal for the study of protein hydration. Nucci *et al.* show that the majority of Ubiquitin in AOT reverse micelles had detectable hydration that spanned the entire theoretical limit. He further concluded that the HX rates are indeed slowed by several orders of magnitude (125, 126). The combination of selective perdeuteration and reverse micelle encapsulation removes all artifacts present in aqueous solution measurements without the need for complicated pulse sequences.

Despite this massive improvement in sample preparation one major technical problem still remains. The overall concentration of protein in a reverse micelle sample is often low (~50-300μM)(116). Cross peaks observed in nuclear Overhauser effect spectroscopy can often be quite low in signal-to-noise intensity due to rapid motions or large distances between dipoles. This is especially true in the case of intermolecular interactions (94). Thus, protein hydration experiments are often very time costly due to the need to collect a high number of transients per FID, which is necessary to obtain peaks with adequate

signal-to-noise (S/N) intensity. Thus, the long time requirements restrict data collection to one or two mix periods. This makes fitting of the cross-relaxation rates impossible without assumptions about the relaxation behavior of water. In this present study two different methods are applied to decrease experimental time in NOESY experiments; reducing the number of points when collecting a three-dimensional experiment, or by reducing the dimensionality of the experiment. Decreasing experimental time allows for the collection of multiple mix times thereby providing more robust data fitting.

Traditional NMR experiments sample uniformly across a Cartesian grid in order to satisfy the criteria for the discrete Fourier transform (DFT). NUS takes advantage of the fact that only a small subset of sampled frequencies contain data while the rest contain noise. Therefore, when using NUS only a fraction of time points need to be collected resulting in decreased experimental time per experiment. This time savings can then be applied to collecting experiments with greater signal-to-noise (S/N) or resolution in a tractable amount of time (170-172). However, processing of NUS data with a traditional DFT results in many artifacts. A number of programs have been created to reconstruct NUS data sets that result in accurate S/N and frequency reconstruction with minimal artifacts. In this present study we use sinusoidally weighted Poisson-gap (173) NUS schedule followed by iterative-soft thresholding (IST) reconstruction (174, 175). IST reconstruction belongs to a larger class of compressed sensing algorithms (176). It has previously been shown to have accurate frequency reconstruction and high linear peak-heights relative to a uniformly sampled reference and also benefits from reduced spectral noise (170, 173, 174). We have chosen this method due to its ease of application, broad

use in the NMR community, and minimal computational requirements. However, the procedure in this present paper should be broadly applicable to a number of NUS sampling scheduling and reconstruction methods.

Full three-dimensional experiments are often not needed to measure protein hydration. Generally, only crosspeaks that occur at the water resonance of the three-dimensional experiment are used for analysis. Time savings can also be accomplished by reducing the dimensionality of the experiment from a three-dimensional to a two-dimensional experiment. This is accomplished by selectively exciting the water frequency prior to the NOE mix time. The excited water is then able to undergo dipolar relaxation (NOE) to nearby protein protons, and then read out using a standard HSQC readout.

First, we identify the minimal recommended non-uniform sampling density necessary for quantitative peak height intensity in NOESY-HSQC spectra. Then we then assess the intra-sample and inter-sample reproducibility of hydration $\sigma^{NOE}/\sigma^{ROE}$ ratios as detected with NUS hydration. This allows us to determine a reliable signal-to-noise (S/N) cutoff below which reproducibility is generally poor. We then collect hydration experiments with a series of mixing times in order to improve the way we calculate the $\sigma^{NOE}/\sigma^{ROE}$. And finally, we introduce two dimensional pulse sequences that can also be used for protein hydration dynamics measurements.

Results and discussion

Choice of Sampling Density

For hydration measurements we need quantitatively accurate peak heights in addition to the precision of peak frequencies. We set out to determine the minimal NUS sampling

density necessary for a quantitative NOE. The peak height intensities of the intermolecular NOE between protein and water is low relative to intramolecular cross peaks. In the case of hydration it is often more beneficial to increase the number of transients per FID than increasing the resolution in the indirect dimensions (170) In order to find a minimum recommended sampling density we collected a series of ^{15}N-edited NOESY-HSQC on U- [^{13}C^{15}N]-ubiquitin collected at low spectral resolution with different NUS sampling densities.

We collected five sampling densities: 5, 10, 15, 20, 25% NUS in both indirect dimensions as well as duplicates in the uniformly sample and 25% sampled (highest sampled density) data sets. Over 200 well-resolved cross-peaks ranging from signal-to-noise of 10-200 (~1-20% diagonal peak height) were compared across the varied densities. The R^2 of peak height intensity converges to ~0.99 at a15% NUS density, however the <RMSD> between Cartesian sampling and NUS sampled data continues to decrease as the sampling density is increased. The percent RMSD in peak height between two Cartesian replicates was 2.2%, compared with two 25% NUS replicates with a percent RMSD of 5.79%. The percent RMSD error between Cartesian sampling and 25% NUS data sets was 5.85%. Because the error of the $\sigma^{NOE}/\sigma^{ROE}$ is taken in quadrature it was important to have a final percent error between two replicates be ~5% of the total measurement.

	Slope	**R^2**	**% <RMSD>**
Cartesian vs. Cartesian	1.005	0.999	2.20%
Cartesian vs. 5% NUS	0.839	0.893	26.96%
Cartesian vs. 10% NUS	0.939	0.976	14.65%
Cartesian vs. 15% NUS	0.952	0.989	10.62%
Cartesian vs. 20% NUS	0.966	0.994	9.06%
Cartesian vs. 25% NUS	0.971	0.996	6.14%
NUS 25% vs. NUS 25%	1.01	0.998	5.79%

Table 3-1: Peak height intensity was compared for NOE cross-peaks in a NUS dataset relative to the peak height intensity of a Cartesian sampling data set of the same experiment. A combination or <RMSD> and slope were used do determine the requirement for 25% NUS sampling for hydration dynamics analysis.

Therefore, all experiments for testing the reproducibility of hydration were used at 25% NUS data collection yielding a total ¼ experimental time. These guidelines provided a conservative estimate that was determined to be sufficient for high reproducibility independent of sampling schedule optimization, resolution, and spectral crowding.

The IST method for reconstructing non-uniformly sampled data belongs to a larger family of compressed sensing (CS) techniques. One of the major limitations of CS techniques is the principle of transform sparsity (176). In general, as the sparseness of the measured signal is decreased (i.e. more peaks in an NMR spectrum), the amount of points collected is decreased, or the sampling density is decreased the reliability of the reconstruction decreases. Conventional 3-dimensional spectra (such as the HNCO) which are spectrally sparse are often recorded with sampling densities as low as ~10%. Unfortunately, NOESY spectra have a much larger number of peaks with a high dynamic range of peak heights. This, in combination with the low signal-to-noise of the inter-molecular NOE presents a challenge for reconstruction of NUS data (170, 171, 177).

It has been shown that in traditional NMR experiments optimal S/N is obtained when indirect dimensions are sampled to $1.26*T_2$, whereas optimal resolution is present at $3.14*T_2$ (178). However, it has also been shown that benefits are observed using NUS from increased S/N and resolution well past $1.26*T_2$ (179). Additionally, the precision of the NUS reconstruction is dependent on the overall number of points collected;

experiments with low sampling density but high resolution are comparable to low resolution, highly sampled data. There is no consensus of optimal sampling density and resolution (170, 180).

In the case of protein hydration measurements the rapid nature of water makes crosspeaks intensities generally quite weak relative to the diagonal (94). In order to simulated an absolute worst case scenario (as may be encountered in large spectrally overlapped proteins) using these criteria we show that a sampling density of 25% results in accurate peak height reproducibility and an RMSD less than 5%. This sampling density is similar to the requirements of a standard 2D experiment (171, 180), an intuitive finding since the water-plane of a 3D NOESY-HSQC largely mimics its HSQC (125). This conservative method does not require optimizing sampling schedules, and is tolerant to spectral overlap. Decreases in RMSD would be present for well-resolved or more high-resolution data collection.

Reproducibility of NUS ^{15}N NOESY-HSQC and ^{15}N ROESY-HSQC hydration experiments

Non-uniform sampling was added to standard ^{15}N NOESY-HSQC and ROESY-HSQC pulse sequences. For simplicity of analysis (see below), all experimental parameters including mix times, pulse length and power, inter-scan delays, and increments collected in each dimension must be the same for both the NOE and ROE experiment. The ROE experiment replaces the laboratory frame NOE mixing period with a continuous-wave spinlock bracketed by 90^{o}_{y} pulses (98). A weak CW spinlock pulse with a bandwidth of ~16-20 ppm ensures a wide excitation bandwidth and suppresses contributions from Hartman-Hahn transfers. The 90^{o} hard pulses bracketing the spinlock remove any off-

resonance effects on the edge of the bandwidth. This scheme does not require complicated phase cycling (Figure 3-1).

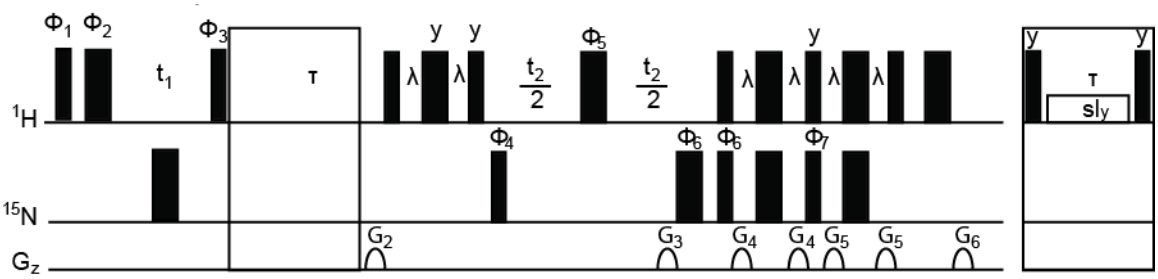

Figure 3-1: ^{15}N NOESY-HSQC and ROESY-HSQC pulse sequences. The boxed region indicates the mix with the ROE counterpart illustrated to the right. Narrow and wide bars indicate 90^{o} and 180^{o} pulses respectively. Phase cycling of scheme: Φ1=4(x), 4(-x), Φ2=4(y), 4(-y), Φ3=16(x),16(-x), Φ4= x,-x, Φ5=2(x), 2(-x), Φ6=2(x), 2(-x), Φ7=2(y), 2(-y), r=x,-x,-x,x,-x,x,x,-x,-x,x,x,-x,x,-x,-x,x,-x,x,x,-x,x,-x,-x,x,x,-x,-x,x,-x,x,x,-x.

In order to study the reproducibility of the hydration dynamics measurements we collected ^{15}N-edited NOESY-HSQC and ROESY-HSQC spectra at a single mix point of three independent samples, each collected in duplicate. Each sample used <90% perdeuterated protein and was prepared in AOT reverse micelles as described previously. The ratio of the height of the NOE and ROE cross peak was then identified for each peak. This allowed us to compare both intra and inter sample reproducibility of hydration dynamics measurements. Both the intra- (Figure 3-2A) and inter-sample (Figure 3-2B) are very reproducible with several obvious outliers.

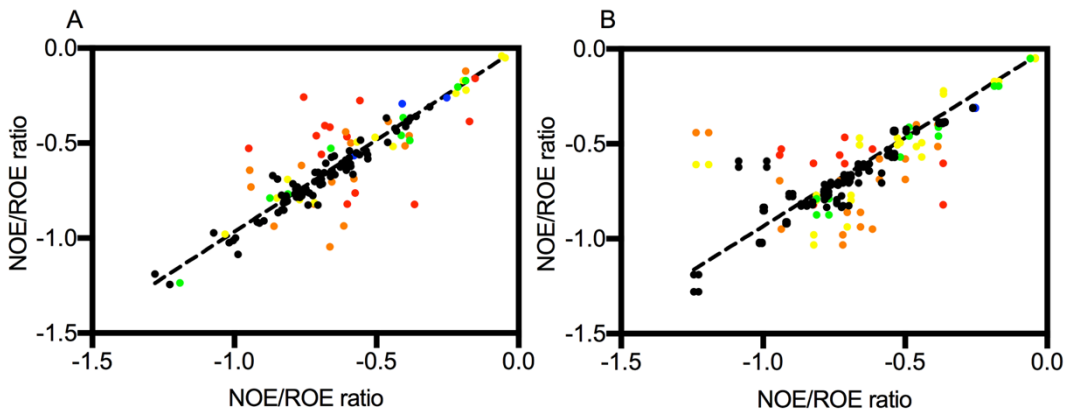

Figure 3-2: The reproducibility of the hydration experiments is dependent on signal-to-noise. Comparison of the uncorrected NOE/ROE ratios within the same sample A) and between different samples B) demonstrate excellent reproducibility with obvious outliers. The black line indicates the line of best fit. Individual sites are colored according to their minimum S/N as follows: Red= S/N<10, Orange= 10<S/N<15, Yellow=15<S/N<20, Green=20<S/N<25, Blue=25<S/N<30.

The comparison of all intra sample points (Figure 3-2) shows a modest R^2 of 0.76 with an <RMSD%> of ~20 percent. By iteratively removing sites with low signal-to-noise the reproducibility of the measurement continues to increase. The signal-to-noise was set to the lowest signal-to-noise between the NOESY and ROESY data sets. Often because of T1ρ relaxation this was the ROESY counterpart. The R^2 and RMSD both begin to plateau when at values of ~0.94, and ~7% of the measurement when only peaks with a minimum S/N greater than 20 is used. As the minimum S/N is increased the reproducibility does not increase dramatically.

	Intra Sample Duplicates			Inter Sample Duplicates		
Minimum S/N	R^2	RMSD	RMSD %	R^2	RMSD	RMSD%
All	0.76	0.117	18.27%	0.23	0.204	37.60%

>10	0.89	0.081	12.33%	0.4	0.181	32.48%
>15	0.95	0.053	8.03%	0.52	0.157	27.42%
>20	0.94	0.052	7.61%	0.65	0.125	19.41%
>25	0.93	0.050	7.16%	0.67	0.112	15.24%
>30	0.93	0.049	6.93%	0.71	0.101	13.08%

Table 3-2: Comparison of inter- and intra- sample reproducibility as a function of signal-to-noise

When comparing inter-sample duplicates similar trends are observed. As peaks with the low S/N are removed from the analysis the R^2 and RMSD improve. However, unlike the case of the intra sample comparisons the overall RMSD continues to decrease as peaks with S/N as high as 30 are discarded. This suggests that slight variations in samples might contribute to slightly decreased reproducibility. However, it should be noted that this is true in the case of low S/N cross peaks, and that peaks with higher S/N remain quantitatively reproducible between samples.

It is interesting to note that even in the IST reconstruction peaks with S/N greater than 8 are reliably constructed in their frequency. However, the absolute peak height is less reliably reproduced with peaks with S/N between 8 and 20. Cross-peaks of low S/N are less reproducible and hence less reliable than those of high S/N. However, these peaks can still be used to detect the present of water in cases where quantitation of the rate is not necessary.

Reverse micelles are spontaneously forming assemblies that adopt their most thermodynamically stable arrangements. Reverse micelle mixtures consist of an ensemble of shapes and sizes. Slight differences in micelle composition on the micro-scale could,

in theory, affect the hydration (114, 116, 137). In general we show that the ratio of the $\sigma^{NOE}/\sigma^{ROE}$, which is the basis of the hydration measurements, is highly reproducible given high signal-to-noise both within a sample and between samples. Additionally, we show that the sites with the highest percent error of the $\sigma_{NOE}/\sigma_{ROE}$ ratio are the sites that have lower signal-to-noise.

Improved data fitting of NOESY and ROESY hydration ratios with a mixing time buildup

To determine the hydration ratios for ubiquitin amides ^{15}N-edited NOESY-HSQC and ROESY-HSQC hydration experiments were collected at four different mixing times (20, 40, 60, and 80 ms). In the linear regime of the NOESY experiment (i.e. no spin diffusion) the signal intensity (I_{NOE}) of the cross peak is proportional to the cross relaxation rates (σ^{NOE}) damped by the auto-relaxation rate (Equation 3-1)(94). The auto-relaxation rate is different in the laboratory and rotating frames, and depends on the relaxation of both the protein and water protons involved in the NOE. In order to fit for the true $\sigma^{NOE}/\sigma^{ROE}$ ratio we collect NOESY-HSQC and ROESY-HSQC spectra at series of mix times. The natural log of the I_{NOE}/I_{ROE} as a function of mix time (τ_{mix}) is fit to a line with the slope equal to the auto-relaxation rates and the intercept equal to the $\sigma^{NOE}/\sigma^{ROE}$ as shown in Equation 3-2.

$$\frac{I_{NOE}(\tau_m)}{I_{ROE}(\tau_m)} = \frac{\sigma_{NOE} e^{-R_1 \tau_m}}{\sigma_{ROE} e^{-R_{1\rho} \tau_m}} \qquad 3\text{-}1$$

$$\ln[-\frac{\sigma_{NOE} e^{-R_1 \tau_m}}{\sigma_{ROE} e^{-R_{1\rho} \tau_m}}] = \ln[-\frac{\sigma_{NOE}}{\sigma_{NOE}}] + (R_{1\rho} - R_1)\tau_m \qquad 3\text{-}2$$

These data were then fit to Equation 3-2 to obtain the effective relaxation rate ($1/T_{1\rho}$-$1/T_1$: slope) and $\sigma^{NOE}/\sigma^{ROE}$ ratios (intercept). All mix times were performed in the linear regime of the NOE to prevent any contamination from spin-diffusion. The T_1 of the NOE is negligible at the mix times used and therefore the overall relaxation rate will be referred to as $T_{1\rho}$, which includes contribution from both protein and water relaxation.

As demonstrated in Figure 3-3A as the mix time of the experiment increases the $\sigma_{NOE}/\sigma_{ROE}$ gets more negative. If only the protein amide proton $T_{1\rho}$ is used to correct for the auto-relaxation, $\sigma^{NOE}/\sigma^{ROE}$ approaches 0 (not shown) resulting in an overcorrection leading to artificially faster hydration measurements. The $T_{1\rho}$ fit from Equation 3-2, which include contributions from amide and water are slower than the amide relaxation alone. There is no correlation between the fit $T_{1\rho}$ of the amide and water peak and the amide $T_{1\rho}$ alone (data not shown). Additionally, the calculated $T_{1\rho}$'s vary substantially suggesting that the water protons interacting with the amides have unique relaxation properties.

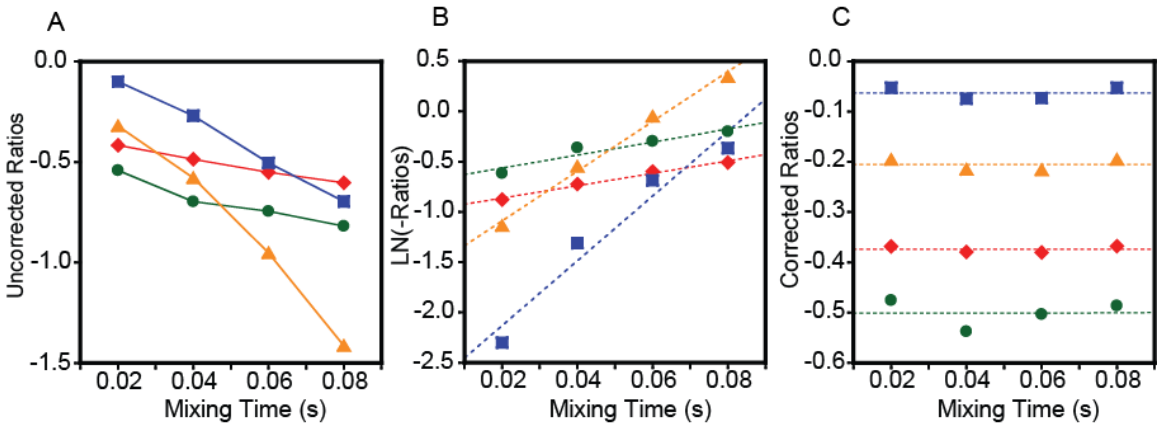

Figure 3-3: The buildup hydration ratios as a function of NOESY and ROESY mixing time (τ_m) demonstrate the necessity of proper $T_{1\rho}$ correction. A) The uncorrected hydration ratios B) fitting of data to Equation 3-2 to for the effective

relaxation time constant ($T1\rho$) and the proper hydration ratio C) Applying the fit $T_{1\rho}$ correction shows nearly constant hydration ratios at all experimental mixing times (20, 40, 60, and 80 ms). The four example residues, T66 (red diamonds), A46 (blue squares), K11 (green circles), and R42 (yellow triangles) were chosen to demonstrate the full dynamic range of the hydration ratio.

Despite the ~10% error possible for each individual time point measurement due to the signal-to-noise fitting using linear regression offers statistics on the precision of the obtained ratios, which would not be possible at a single mix time alone. This, in combination with the longer mix times that can be sampled, can be advantageous in the case of lower signal-to-noise cross peaks. In general, this fitting method appears to be highly robust and is independent of assumptions of uniform water relaxation.

It has previously been assumed that the amide-proton $T_{1\rho}$ is the fastest relaxing term in the hydration measurements and can therefore be used to correct for the auto relaxation in the $\sigma^{NOE}/\sigma^{ROE}$ (125, 126). However, we here we show that the relaxation behavior is a complex mixture of water and protein relaxation in both the laboratory and rotating frames. Performing a full buildup is the only way to obtain the coefficient of the auto-relaxation, as there is no clear correlation between amide proton $T_{1\rho}$ and the $\sigma^{NOE}/\sigma^{ROE}$ relaxation term. Furthermore, linear regression of the buildup further increases the precision of the measurement

Implementation of 2D pulses sequences

Three-dimensional experiments require long data collection times. Two-dimensional projection variants can be used to reduce data collection time and simply involves selective excitation of the water resonance prior to the mixing time(181). While many

water selection schemes have been reported in this study we use the e-PHOGSY water excitation scheme. This selective scheme is robust, easy to implement, and can be used for both aqueous and reverse micelle experiments. The e-PHOGSY scheme is a spin-echo sequence that begins with a 90^{o}-G1-180^{o}_{wat}–G1-90^{o} scheme, which renders the water magnetization longitudinal (182). Example pulse sequences for both two-dimensional and three-dimensional ^{15}N NOESY and ROESY-HSQC's are shown in Figure 3-4.

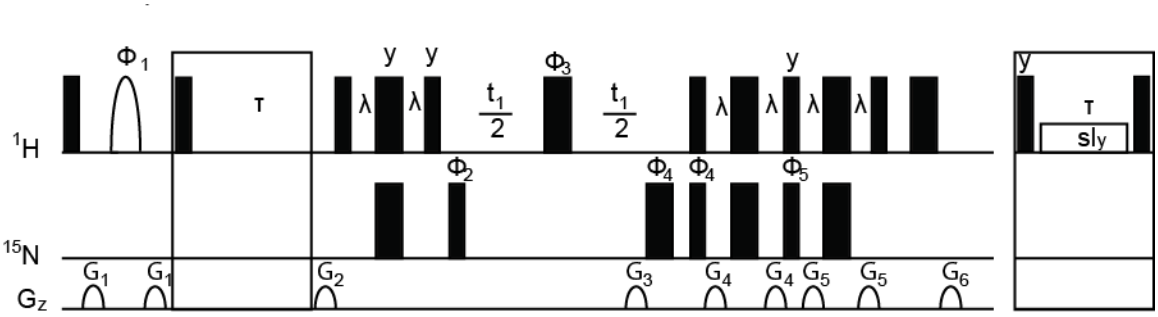

Figure 3-4: Water-selective two-dimensional NOESY-HSQC pulse sequence. The boxed region indicates the mix with the ROE counterpart illustrated to the right. Narrow and wide bars indicate 90^{o} and 180^{o} pulses respectively. Water selective 180^{o} shaped pulse is illustrated as a hollow shape. All phases are x unless otherwise indicated. Phase cycling of scheme Φ1=4(x),4(y),4(-x),4(-y), Φ2= x,-x, Φ3=2(x), 2(-x), Φ4=2(x), 2(-x), Φ5=2(y), 2(-y), r=x,-x,-x,x,x,-x,x,-x,-x,x,-x,x,x,-x.

Comparisons peak height intensities between three dimensional and water-selective two-dimensional ^{15}N NOESY-HSQC and ^{15}N ROESY-HSQC spectra at 60ms mix times are shown in Figure 3-5. Both the 15N NOESY-HSQC (Figure 3-5A) and 15N ROESY-HSQC (Figure 3-5B) correlations have R^2 values >0.98 suggesting that two-dimensional water selective experiments are a good alternative to standard three-dimensional experiments. However, the signal-to-noise of two-dimensional experiments is

substantially lower than in three-dimensional experiments. This is because only the water protons are excited during the experiment. The reverse micelle has very few waters relative to bulk aqueous solution. The reduction in water results in less excited protons. Therefore, the signal-to-noise of the water selective experiments will also depend on the W_o of the sample. The decreased signal-to-noise can be compensated by an increased number of transients collected per FID. In general, the two-dimensional NOESY-HSQC and ROESY-HSQC can offer an approximate two times savings relative to a NUS non-selective three-dimensional experiment.

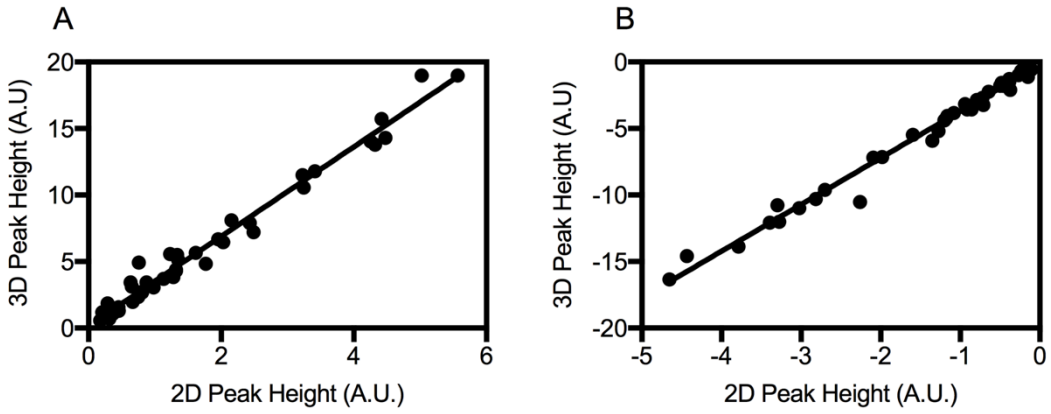

Figure 3-5: Comparison of peak height intensity between non-selective 3 dimensional experiments and 2 dimensional water selective experiments

In the present study we use a 15 ms long 180^o water selective SINC pulse in order to maximize signal-to-noise. In general, the water-selective 180^o pulse should be chosen depending on the bandwidth of excitation needed versus the duration of the pulse length. If fully perdeuterated protein is used, a relatively short (10-15 ms) water selective (e.g. SINC, Gauss) pulse is recommended to prevent relaxation of the water during the spin-echo. The shorter selective pulse will help increase signal-to-noise in the experiment. If

the protein cannot be fully perdeuterated and contributions from H_α are a concern, a longer (G3, reburp) pulse can be used. The intra-protein protons relax due to T_2 relaxation during this time removing contamination from intramolecular H_α peaks. However, some of the water will also relax in this time period resulting in slightly less signal-to-noise. Previous hydration experiments have used isotopic filtering schemes to remove any magnetization that originates from ^{13}C bound protons. While effective at removing intra-molecular NOE's the additional filtering module results in reductions in signal-to-noise and sensitivity. Additionally, these methods require uniform ^{13}C isotopic labeling. The pulse sequence presented here is straightforward to implement and removes the need for complicated pulse sequences while still being able to filter for intra-molecular H_α protons.

Conclusions

Despite the importance of water in biological systems the ability to quantify water interactions has remained technically challenging. In this study we set out to improve the way the protein-water interactions are measured via NMR. It has previously been shown that optimal choices in sample preparation such as for proteins encapsulated in reverse micelles are necessary to remove experimental artifacts (125, 126). Here, we extend those methods to improve data collection and analysis in order to obtain reproducible and quantitative $\sigma^{NOE}/\sigma^{ROE}$ rates.

We implement sinusoidally weighted Poisson-Gap NUS (173) data collection, and IST reconstruction to 3D ^{15}N-edited NOESY and ROESY spectra (175). In the case of hydration it is highly recommended to use the NUS to increase the number of transients

per FID instead to increase precision of the measurement (170). The implementation of NUS also allowed us to comprehensively test the reproducibility within and between samples.

We highly recommend that a duplicate of one mix point be collected for each protein measured as a reference to determine the minimal S/N necessary for reproducibility. The conventional measure of S/N ratio in NMR spectroscopy is the peak height divided by the RMS noise of a peak less spectral region. While this assumption holds true for fully sampled data, NUS noise is non-Gaussian and non-uniformly distributed. Several metrics for measuring S/N in NUS sampled data have been discussed (171, 172), and are beyond the scope of the paper. Here, we use standard calculation of RMS noise to define our S/N cutoff. This is used as a metric to determine the S/N cutoff for reproducibility of the $\sigma_{NOE}/\sigma_{ROE}$ in our hands. This should allow for a broadly applicable metric for S/N despite variations in pulse sequence, NUS sampling schedules, reconstruction methods, and S/N calculation.

Previous studies have measured the NOE/ROE at a fixed mixed point (53, 89-92, 125, 126, 183-186). The time savings from the decreased experimental time allowed us to collect 4 sets of NOESY-HSQC and ROESY-HSQC experiments with varied mix times. This allowed us to perform a full buildup series and fit for the desired $\sigma^{NOE}/\sigma^{ROE}$ and relaxation rates. Performing mix time buildups does not require assumptions or *apriori* knowledge of the relaxation behavior of the amide-proton and water-proton vector. This allows for a more robust and accurate way of fitting for the $\sigma^{NOE}/\sigma^{ROE}$.

In general, the methods presented here offer an experimentally tractable way of measuring protein hydration in a quantitative fashion via the NOE. The implementation of non-uniform sampling to three dimensional NOESY-HSQC and ROESY-HSQC spectra, or two-dimensional water-selective experiments is sufficient to reduce experimental time and allow for increased signal-to-noise and greatly improved data fitting methods. Collection of one duplicate spectrum at a single mix point is needed to determine the S/N cutoff required for robust reproducibility. This makes the method broadly applicable so other implementations of NUS sampling and reconstruction may be used.

Chapter 4: Decoupling of hydrogen exchange relay artifacts for detection of protein-water NOEs on the protein surface

Abstract

The ability to measure protein hydration dynamics with site resolution has been a missing link in the biophysical puzzle. Many techniques have been proposed to measure protein hydration; however, many of them either require mutation, or lack dynamic or site resolution. Those that do not have these limitations are riddled with artifact due to the ubiquitous and dynamic nature of bulk water. It has been shown that protein hydration dynamics can be measured using NMR spectroscopy by encapsulating proteins in reverse micelles. The combination of confinement from the micelle and the removal of bulk water are necessary for measuring surface hydration dynamics from the NOE. The NOE is able to detect magnetization through both physical hydrogen exchange as well as the dipolar interaction between two nearby spins. The reverse micelle slows hydrogen exchange by approximately two orders of magnitude. This is sufficiently slow to remove any contamination from direct hydrogen exchange of backbone amides, but is insufficient to entirely remove hydrogen exchange relay artifacts from side chains. The overall slowing of hydrogen exchange provides a unique environment such that the exchange is slow enough to be in the slow-exchange regime of NMR and therefore spectrally resolved from water. In this present study we take advantage of the unique chemical shifts of hydroxyls to decouple any NOE contribution during the mix period. This serves to remove hydrogen exchange relay artifacts and facilitates direct detection of protein water interactions via the NOE. We apply this method to Ubiquitin in AOT reverse micelles and show that all values are within the theoretical limit of the measurement.

Additionally, we show that the majority of slowed waters reside near previously identified crystallographic waters. The method introduced here provides a robust and artifact free way of measuring protein hydration via the NOE.

Introduction

Water is necessary for protein function (8) and is involved in aspects of protein folding (44), stability (187), catalysis (58) dynamics (73), and protein interactions. It is known that water dynamics are heterogeneously slowed at the protein interface (63). In order to understand the thermodynamic contribution of water on protein function it is necessary to measure the dynamics of the hydration layer with site resolution (6, 7). However, a site resolved view of protein hydration dynamics is very difficult to obtain experimentally. Solution nuclear magnetic resonance spectroscopy (NMR) has been used to measure protein water interactions via the nuclear Overhauser effect (NOE) for several decades (31, 89, 90, 93).

The nuclear Overhauser effect (NOE) detects through-space dipolar magnetization transfer (94). The NOE reports on both inter- and intra-molecular interactions but has extremely sensitive r^{-6} distance dependence. Only the first hydration layer surrounding the protein is close enough to the protein to be detected via the NOE. The short-range nature of the NOE makes it ideal to allow for site specificity of protein-water interactions. The magnitude of the NOE cross relaxation rate (σ^{NOE}) increases with the effective correlation time of the protein-water interaction. The NOE can be observed from magnetization transfer in both the laboratory (NOE) and rotating (ROE) reference frames. Otting *et al.* showed that the effective water correlation times could be

extrapolated from the ratio of these rates ($\sigma^{NOE/}$ σ^{ROE}), thereby giving dynamic information (90, 93).

In theory this methodology should provide site resolved hydration dynamics across the surface of the protein. Unfortunately, several aspects of bulk water result in artifacts when this method is applied to the surface of the protein thereby limiting its use to only buried structural waters (75, 102). The artifacts are generally caused by the high concentrations of water relative to protein, as well as the very fast timescales of water reorientation and hydrogen exchange rates. Nucci *et al.* showed that encapsulating proteins in the interior of a reverse micelle remove contamination from artifacts thereby facilitating the detection of hydration water dynamics (125, 126).

Reverse micelles are spontaneously forming particles composed of a nano-pool of water, an amphiphilic surfactant shell, and bulk organic solvent (137). The nano-pool of the reverse micelle is sufficient to solubilize a protein in its folded conformation. Encapsulation removes bulk water while maintaining the native hydration shell of the protein. This removes any signal from bulk water and removes any contamination from exchange between the hydration layer and bulk that maintains the local nature of the NOE. Additionally, confinement from the reverse micelle slows the rotational and translation motions of water as well as the hydrogen exchange rates (27, 66, 68, 125). Therefore the slowed waters amplify the effect of the NOE and the slowed hydrogen exchange removes contamination from exchange and exchange-relayed processes that can also be detected by the NOE.

In the reverse micelle the hydrogen exchange rates of amides are sufficiently slow to eliminate any contamination from direct hydrogen exchange. Unfortunately, the hydrogen exchange rates of side chains are substantially faster than amides. The pH minimum of hydrogen exchange is also shifted for side chains and is often between 5 and 7 (162). Hydrogen exchange from side chains can contribute to hydrogen-exchange relay artifacts in NOESY and ROESY experiments. These artifacts, unlike direct hydrogen exchange, are spectrally indistinguishable from a direct NOE.

This present studied measures hydrogen exchange rates of a small molecule, glucose, in different reverse micelle mixtures as a function of pH and buffer concentration. This allows for a better understanding of hydrogen exchange chemistry within the reverse micelle. The results from glucose suggest that hydrogen exchange is indeed quenched but likely still remains fast enough for hydroxyl containing side chains. Therefore we implement NMR experiments that decouple hydrogen exchange during the NOE to identify sites that have detectable hydrogen exchange relay artifacts. A novel data fitting is outlined and the surface hydration dynamics of ubiquitin in AOT reverse micelles is described.

Results and discussion

Measurement of glucose hydrogen exchange in the reverse micelle

In addition to dipolar interactions the NOE can potentially contain contributions from direct hydrogen exchange and exchange-relayed hydrogen exchange. Nucci *et al.* showed that reverse micelle slows hydrogen exchange chemistry by over 2 orders of magnitude (125). Hydrogen exchange can either be acid or base catalyzed (H^+, OH^-), water

catalyzed, or buffer catalyzed. The removal of bulk water in the reverse micelle limits the H+ and OH^- catalysis. Unfortunately, every micelle has both water and buffer that can still contribute to the overall hydrogen exchange chemistry. Both the sample buffer, as well as the surfactant can act as weak acids/bases for catalysis if the pK_a is generally low. The exchange chemistry of amides at pH 5 in RMs is sufficiently slow to not be detected by the NOE (161). Amino acid side chains have intrinsically higher exchange rates and can still be detected by the NOE (162). The hydrogen exchange rates of glucose were measured in the reverse micelle in order to quantitatively understand the exchange chemistry in the reverse micelle using EXchange SpectroscopY (EXSY) (105, 160). A small molecule is ideal for measuring hydrogen exchange rates due to its increased sensitivity and spectral simplicity. Glucose is a water-soluble small molecule that has a pK_a of ~12. The amino acid side chains with the highest exchange rates at pH 5 are Tyrosine, Serine, and Threonine, which have pK_a's of 10.5, 13, and 13, respectively (Table 4-1) (162). Therefore, glucose was an ideal choice to understand the exchange chemistry in the reverse micelle.

	pK_a
Glucose	12
Tyrosine	10.5
Serine	13
Threonine	13
Lysine	10.5
Arginine	12.5

Table 4-1: pKa values of glucose and exchangeable side chain protons.

The exchange behavior varies with the surfactant mixture used (Figure 4-1). The head group in AOT has a titratable head group. It has been shown that the sample pH is dominated by the pH of the AOT that is used. The HX rates of glucose in AOT are pH

dependent. AOT has a low pK_a of ~5 and acts as a catalyst below pH 5. The acid catalyzed hydrogen exchange limb of the AOT HX has a standard slope 1 per pH unit. Intriguingly the base form of the sulfate group does not appear to catalyze HX. CTAB/hexanol surfactant mixtures are unable to act as catalysts. Hexanol is the only titratable part of the surfactant and its pK_a is too high (~20) to contribute to HX at standard experimental pH. Therefore, the HX rates of glucose in the reverse micelle do not change with pH of the surfactant. In addition to surfactant effects the buffer used can also catalyze exchange. The concentration dependence of HX for acetate is present but is generally low. The concentration dependence of buffer of phosphate is substantially higher and in fact cannot be measured at a concentration above 20mM $NaPO_4$. Therefore phosphate buffer should be avoided for hydration studies. These findings suggest that care must be taken in the choice of surfactant mixture, pH, and buffer conditions when encapsulating proteins in reverse micelles. Present studies use AOT reverse micelles at pH 5 and use 10mM NaAcetate buffer to reduce hydrogen exchange contributions.

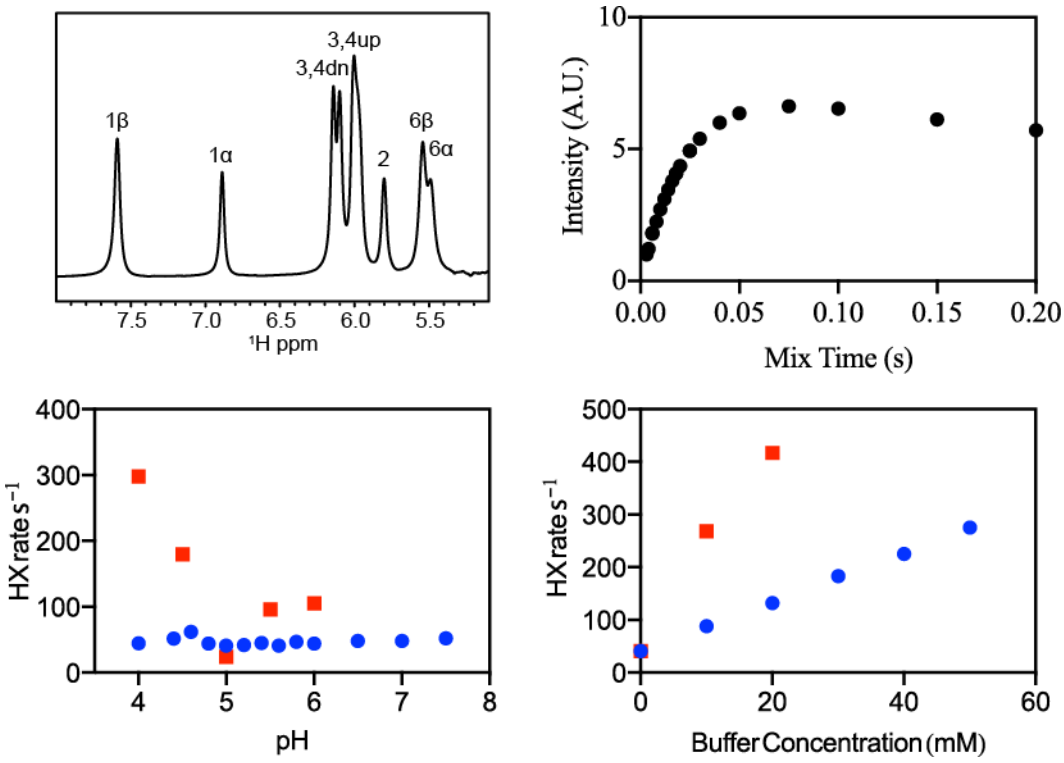

Figure 4-1: Hydrogen exchange rates of glucose in the reverse micelle. A) 1D ^{1}H spectrum of glucose in CTAB/hexanol reverse micelles showing that the exchange rates are slowed and in the slow-exchange regime via NMR. B) Example EXSY curve and fitting of a glucose peak in CTAB/hexanol RM at pH 5. C) The different behavior of HX as a function of pH between AOT (red square) and CTAB/hexanol (blue circle) reverse micelles. D) The effect of buffer on glucose HX in CTAB/hexanol reverse micelles using Sodium acetate (blue circles) and sodium phosphate (red squares) as buffer.

In the absence of buffer the glucose exchange rates are ~50 s^{-1} in the reverse micelle which is in stark comparison to rates of ~2000 s^{-1} when measured in bulk aqueous solution. These HX rates will vary depending on the surfactant, pH, and buffer. Additionally, Levinger *et al.* showed that the HX rates vary depending on the *W*o used (133). This is due to an increased water catalyzed rate due to the increased dynamics of water in the RM at higher water loading. The pK_a values of T/Y/S hydroxyls are

approximately one pK unit lower than glucose. Therefore, the side chain HX rates of T/S/Y residues in a protein are sufficiently fast to be on the same timescale as the NOE and ROE cross relaxation rates (~1-10^{-s}). The exchange rates in the slow exchange NMR timescale and hydroxyl residues have unique peaks in ^{1}H spectra.

Implementation of broadband decoupling of exchange relay

The overall slowing of HX in the revere micelle is approximately 2 orders of magnitude. The HX rates for serine and threonine hydroxyls have pH minimums at around 6.5. The HX rate of serine and threonine in bulk aqueous solution at pH 5 is 1000 s^{-1}. Therefore, in the reverse micelle, the HX rate is still approximately 10 s^{-1}. If a labile hydrogen that is within NOE-distance of the NOE detection spin (e.g. amide hydrogen) exchanges sufficiently rapidly with water then an NOE cross peak between the water resonance and the amide hydrogen will be created even though water may not actually be close the amide hydrogen. This exchange relay process is otherwise indistinguishable from an authentic intermolecular NOE. The residual HX is sufficiently fast for serine and threonine hydroxyls to cause exchange relay artifacts in the NOE experiments. However, the HX rates are sufficiently slow on the NMR timescale to have distinct chemical shifts relative to water. Melacini *et al.* showed that if hydroxyls are sufficiently slow to have unique chemical shifts they can be decoupled during an NOE experiment thereby removing exchange relay contamination (184, 185). Decoupling was added to the mix period of standard two-dimensional water selective experiments (Figure 4-2: A) Pulse sequence used to decouple relaying hydroxyls from the NOE spectrum. Black rectangle pulses are 90^{o} hard pulses, open shaped pulse is a water-selective 180^{o} shaped pulse, and

closed pulses are 180° broadband selective pulses centered on the hydroxyl peaks. The selective decoupling pulse is looped n times for the duration of the mix. B) A diagram of how the decoupling experiment works to remove exchange relay. A protein hydroxyl is able to hydrogen exchange directly with water, and subsequently NOE to a nearby protein amide. The hydroxyl proton is continuously flipped using a broadband decoupled pulse so it is no longer able to effectively NOE.

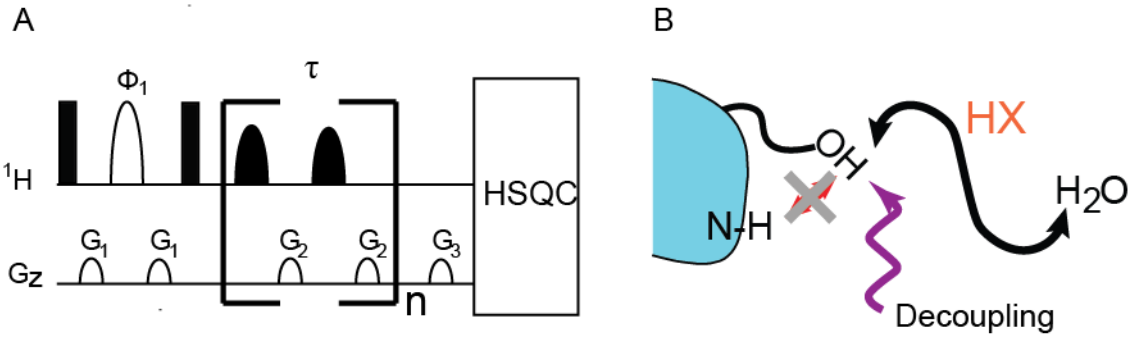

Figure 4-2: A) Pulse sequence used to decouple relaying hydroxyls from the NOE spectrum. Black rectangle pulses are 90° hard pulses, open shaped pulse is a water-selective 180° shaped pulse, and closed pulses are 180° broadband selective pulses centered on the hydroxyl peaks. The selective decoupling pulse is looped n times for the duration of the mix. B) A diagram of how the decoupling experiment works to remove exchange relay. A protein hydroxyl is able to hydrogen exchange directly with water, and subsequently NOE to a nearby protein amide. The hydroxyl proton is continuously flipped using a broadband decoupled pulse so it is no longer able to effectively NOE.

This decoupling scheme was applied to 90%-^{2}H,^{15}N-Ubiquitin in AOT reverse micelles (Figure 4-3). Hydroxyls of Ubiquitin had been previously assigned owing to the slowed HX in the reverse micelle. The water peak of ubiquitin in AOT reverse micelles resonates at 4.5 ppm. Hydroxyls resonate at 4.7-6.15 ppm. G3 pulses are selective “top hat” pulses that have uniform excitation across the bandwidth and no net perturbations occur outside

the bandwidth of excitation (188). Unfortunately, though net magnetization is unaffected the nuclei immediately outside of the excitation bandwith experience perturbations during the pulse.(184). Resonances near the decoupling pulse undergo T_2 relaxation during the decoupling pulse. The stronger the decouple pulse (i.e. wider bandwidth excitation) the more off-resonance frequencies are affected. The hydroxyls resonate at frequencies near water and therefore decoupling pulses result in slight relaxation of the water. Therefore, two individual decoupling pulses were applied to reduce the relaxation of the water. Two 10 ms G3 180^{o} inversion pulses with a 0.6 ppm bandwidth centered at 5.4 and 6.1 ppm were used in ^{15}N detected water selective NOESY-HSQCs. The hydroxyls from residues Thr55 and Ser57 could not be decoupled due to their proximity to water and therefore sites within 4 Å of these residues were not analyzed.

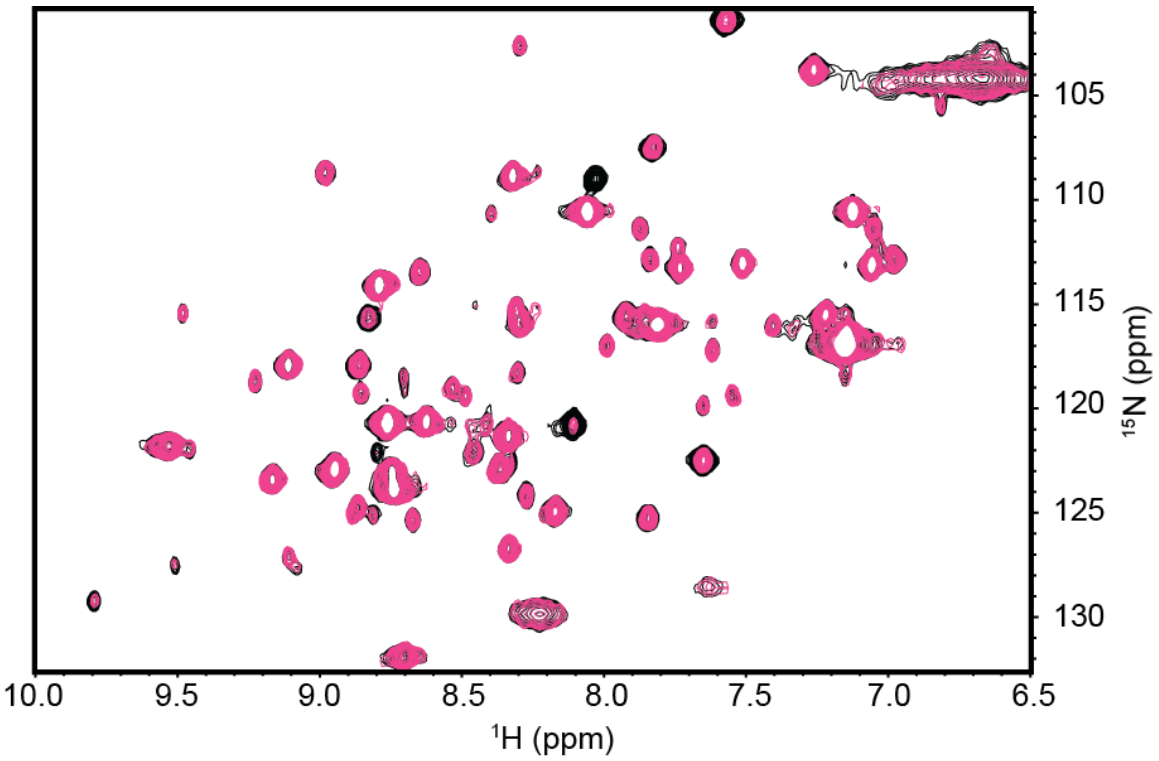

Figure 4-3: Overlay of two-dimensional water selective NOE (black) and NOE with decoupling (pink) with 100ms mix time of Ubiquitin in AOT reverse micelles. The decoupling experiment was collected with a 10ms G3 inversion pulse centered at 5.4ppm with a bandwidth of 0.6 ppm.

When the decoupling is applied to the NOE experiment then exchange relay is removed from the overall rate. The resultant spectrum has the pure NOE rates to water without any contamination from hydrogen exchange. The G3 pulse centered at 5.4 ppm decouples residues Thr7, Thr9, and Ser20. A decreased NOE from the decoupled experiments relative to the standard NOE experiments were observed at residues Thr9, Gly10, Lys11, Thr12, Thr14, Ser20, Thr22, Asn25, Gln62, Ser65, and Thr66. The G3 pulse centered at 6.1 ppm decouples residues Ser65 and Thr66. The residues affected were Thr12, Thr14, Ser20, Thr22, Asn25, Gln62, Ser65, and Thr66. The hydroxyls from residues Thr14 and Thr22 were not assigned but are affected by both G3 pulses suggesting that they are

likely between the two-excitation bandwidths. Similarly, the hydroxyl from Tyr59 was not assigned, but only one amide, Glu51, was within NOE distance of this hydroxyl.

Calibration of pulse location and lengths and correcting for kappa

The decoupling pulses during the mix results in slight relaxation of water during the pulse. A correction for this artifact was measured by using a two-dimensional water selective NOE experiment with a 360^{o} decoupling gauss pulse in the middle of the mix period. In order to determine the correction factor, the peak height intensity of each peak in the decoupled NOE correction experiment was compared to the peak height intensity of the standard two-dimensional NOE experiment. The ratio of the unaffected peaks yields the correction factor for one single 360^{o} pulse. The correction factor is determined from the slope of intensities not affected by the decoupling pulse. The correction depends on the pulse length and center of excitation and thus needs to be determined for each decoupling pulse profile and parameter sets. In principle, once the correction factor is determined, the NOE peak intensities for all mixing times can be corrected by using κ^{n} where κ is the correction factor for each 360^{o} cycle and n is the number of cycles used (189). In order to identify κ two-dimensional water selective NOE and decoupled NOE experiment were collected with a mix time of 140 ms mix time for both decoupling pulses. The decoupling pulse length was set to 10ms for a 180^{o} inversion, resulting in a 20 ms 360^{o} pulse during the mix. A histogram of the ratios with high signal-to-noise in each measurement was used to identify the top 10% of ratios. The slope of the NOE versus the decoupled NOE of the top 10% provides κ (Figure 4-4). The decoupling pulse centered at 5.4ppm was determined to be 0.946 with 95% confidence intervals between

0.94 and 0.95. The decoupling pulse centered at 6.1 ppm was determined to be 0.96 with 95% confidence intervals between 0.946 and 0.97. A κ value of 0.95 and 0.97 were selected for pulses centered at 5.4 ppm and 6.1 ppm, respectively.

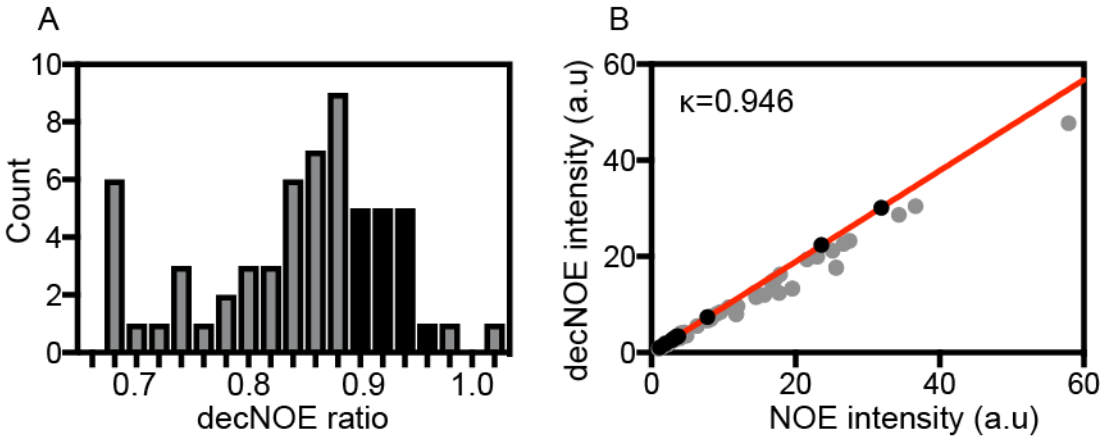

Figure 4-4: Using a 2D experiment to determine κ for a decoupling pulse centered at 5.4 ppm A) Histogram of the ratio of peak height intensity of the NOESY-HSQC with decouple pulse versus the NOE without the decouple pulse. The ratio cannot be above 1 since the decouple experiment can never have more signal than the NOE experiment. Both experiments used a 140ms mix time with a 20ms 360° decouple pulse in the middle of the mix. The highest ratio of decoupled/non-decoupled are those that are not decoupled during the experiment. The top 10% of peaks are used to determine κ B) A plot of the peak height intensity of the NOE versus the decoupled experiment for all peaks (grey circles), and the highest ratio (black circles) between NOE decoupled vs. NOE. The slope of the red line gives κ=0.946.

The magnitude of the correction factor needs to be small and pulse profiles that result in κ values less than 0.95 should be avoided. It is therefore often necessary to employ weaker, more selective decoupling pulses at the expense of having to repeat the experiments to cover the entire region of interest. Nevertheless, even for very high κ values it is generally not feasible to correct the entire NOE evolution curve satisfactorily.

In order to sample the full curve of the NOE on a deuterated protein the mix time must sample extremely high values (1 sec). Using a 10ms decoupling pulse requires a κ^{50} correction factor and is therefore unreliable at long mix times. Additionally, very slight variations (0.005) of the determined κ value can result in under or overcorrection of the overall intensity. Fortunately, the NOE cross-relaxation rate relies on the slope of the initial curves and this is not a concern and the correction factor at long mix times will largely affect the T_1 relaxation term.

Fitting NOE/ROE ratios without hydrogen exchange relay contributions

Full buildup curves for the NOE, ROE, and decoupled-NOE at 5.4 ppm and 6.1 ppm were collected for ubiquitin in AOT reverse micelles. All experiments used a two-dimensional water selective experiment and all experimental parameters including inter-scan delay, number of scans, and digital resolution were matched. The ROE experiments used mix times of 10, 15, 20, 25, 30, 35, 40, 45, 50, 60, 70, 80, 90, 110, 130, 150, 250 ms. All NOE and decoupled NOE experiments used mix times of 20, 40, 60, 80, 100, 140, 180, 240, 300, 400, 550, 750, 1000 ms. The best fit curves were fit to extract the cross-relaxation rate of each set of experiments as described below (Figure 4-5).

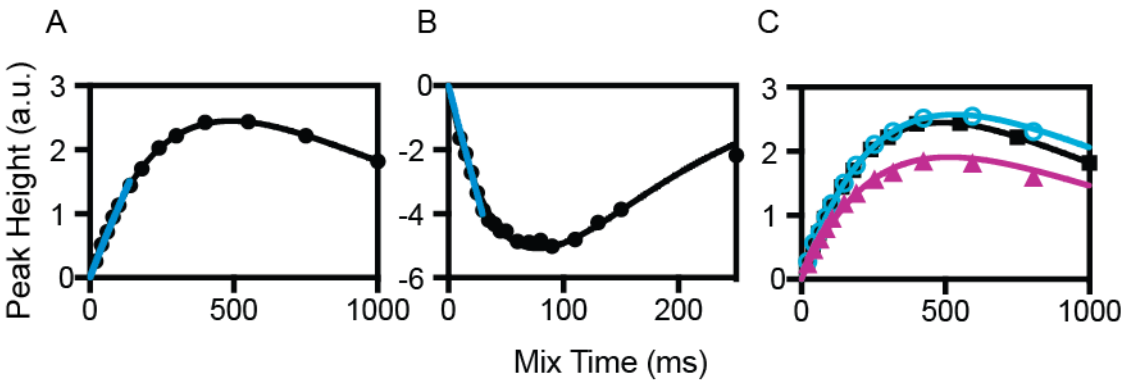

Figure 4-5: Example buildup curves for residue Leu8 of ubiquitin in AOT reverse micelles. A) NOE buildup curve and B) ROE buildup curve. The peak height intensities are shown as black circles with the a full curve fit shown in black, and a fit using the first several points in the linear regime in blue. C) The effect of decoupling on peak height intensity. NOE buildup curve is shown as black squares, the buildup with the decoupling centered at 6.1 ppm (teal circles), and the buildup with the decoupling at 5.4 ppm (magenta triangles). Decoupling at 6.1 ppm does not affect the NOE, whereas the rate is decreased by ~50% when the decoupling at 5.4 ppm, suggesting that there is an exchange relay contribution from a hydroxyl resonating at 5.4 ppm.

The curves for the NOE, ROE, and decoupled-NOE experiment need to be individually fit to Equations 4-1 and 4-2

$$I_{NOE} = A_o[e^{-R_1\tau_m}(1-e^{-\sigma_{NOE}\tau_m})] \quad 4\text{-}1$$

$$I_{ROE} = A_o[e^{-R_{1\rho}\tau_m}(1-e^{-\sigma_{ROE}\tau_m})] \quad 4\text{-}2$$

Unfortunately due to the similar timescales of σ^{NOE} and R_1 (σ^{ROE} / $R_{1\rho}$) these equations are difficult to fit for directly. Fortunately, the A_o term is constant for all experiments assuming identical acquisition parameters and good sample stability. Global fit parameters were used on to determine the A_o term in the NOE experiment. A global fit of the A_o term was accomplished by fitting crosspeaks with mixing times in the linear regime of the NOE buildup by using Equation 4-3:

$$I_{NOE} = A_o(1 - e^{-\sigma_{NOE}\tau_m}) \quad 4\text{-}3$$

The determined A_o term was held constant and each set of experiments was fitted to Equations 4-1 and 4-2 using the full buildup and Equation 4-3 using the first few points. The first few points were collected so that they are in the linear regime of the NOE buildup curves. The rates fit using these two methods should be the same, although the rates might differ slightly (Figure 4-6). Fitting to Equation 4-3 requires less parameters and is an easy fit. However, because it is constrained to peaks in the linear range the signal-to-noise is generally low. In cases where the linear regime is too noisy the full buildup allows sampling at longer mix times and therefore greater signal-to-noise. However, the relaxation term R_1 of the full Equation fitting may be skewed due to the overcorrection due to κ at long mix times.

The σ^{NOE}, σ^{ROE}, and σ^{NOE}_{dec} rates are needed to determine the $\sigma^{NOE}/\sigma^{ROE}$. For sites that are not contaminated by exchange relay the ratio of the fitted rates is sufficient. For sites that contain exchange relay one must fit the σ^{NOE} and σ^{ROE} to Equations 1-10 and 1-11. The difference of the cross relaxation rates between the NOE experiment and the decoupled-NOE experiment give the contribution from HX relay:

$$(\Sigma k_{ex} \bullet \sigma_{NOE}^{intra}) = \sigma_{NOE}^{dec} - \sigma_{NOE} \quad 4\text{-}4$$

The intramolecular ROE is 2x the NOE, therefore the HX contribution is 2x greater for the ROE than the NOE. The ROE can be calculated using:

$$\sigma_{ROE} = \sigma_{ROE}^{obs} - 2(\Sigma k_{ex} \bullet \sigma_{NOE}^{intra}) \quad 4\text{-}5$$

All ratios should fall within -0.5-0 (Figure 4-6). As a general rule this data fitting method must include at least 5-10 different mix times per experiment type. The choices in mix time does not need to be matched for the different experiments as each curve will be fit independently. It is highly recommended that the linear regime be highly sampled.

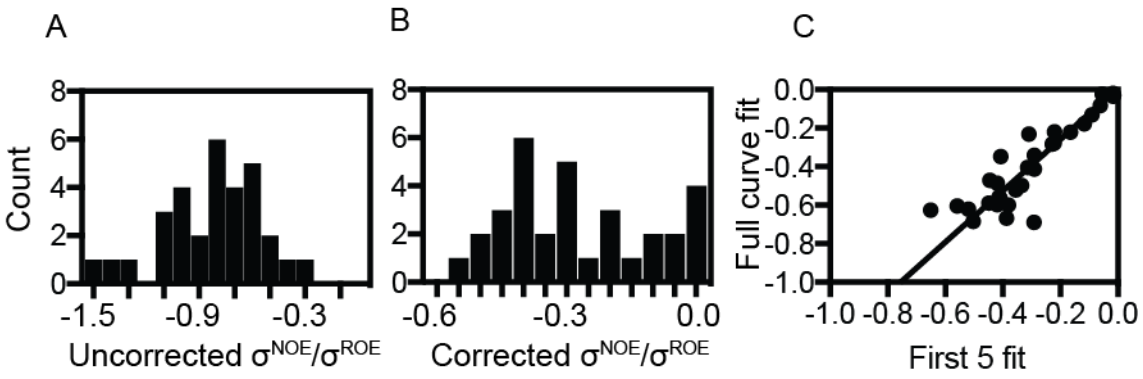

Figure 4-6: Fitting the NOE/ROE ratios. A) Distribution of the $\sigma^{NOE}/\sigma^{ROE}$ ratios without correcting for exchange-relayed contributions. Most of the ratios are >-0.5 and are outside of the theoretical limit. B) Distribution of the $\sigma^{NOE}/\sigma^{ROE}$ after fitting for contributions from hydrogen exchange relay. Most sites are within the theoretical limit of -0.5-0. C) The correlation of the $\sigma^{NOE}/\sigma^{ROE}$ when the first 5 points of the buildup is fit to Equation 4-3 versus when fit to the full curve (Equation 4-1).

The raw $\sigma^{NOE}/\sigma^{ROE}$ ratios without decoupling of hydroxyls range from -0.3 to -1.5 (Figure 4-6 A). This is substantially higher than the theoretical limit of 0 to -0.5. The $\sigma^{NOE}/\sigma^{ROE}$ ratios after decoupling the hydroxyls range from 0 to -0.55 with one additional outlier at -0.65 (Figure 4-6 B). The additional NOE from the relayed hydroxyl will artificially decrease the $\sigma^{NOE}/\sigma^{ROE}$ ratio. This is due to the intra-molecular NOE being half the magnitude of the internal ROE. Upon decoupling, almost all sites are within the theoretical range. The $\sigma^{NOE}/\sigma^{ROE}$ were fit using both Equation 4-1 and Equation 4-3 (Figure 4-6 C). The two fitting methods are in good agreement with a slope of 1.3 and an R^2 of 0.9.

Surface mapping of ubiquitin hydration

The final $\sigma^{NOE}/\sigma^{ROE}$ ratios were plotted on the protein structure to identify which regions of the protein had the slowest hydration dynamics. There are a total of 73 amides in ubiquitin (76 resides with 3 prolines). A total of 6 amides had positive crosspeaks in the ROE spectrum, which are indicative of hydrogen exchange. These residues include Thr12, Lys33, Asp39, Ala46, Lys63, and Gly75. An additional 6 amides could not be analyzed due to their proximity to a hydroxyl that was not decoupled in either of the two pulses. These include residues E51 which is the only amide within 4 Å of Tyr59, and residues Thr55, Leu56, Ser57, Asp58, and Tyr59 with are within 4 Å Thr55 and Ser57 hydroxyls. Sites with signal-to-noise ratios less than 20 in any of the experiments were excluded due to lack of reliability of the buildup curves. An additional 9 sites could not be analyzed due to their proximity to an H_α proton that was overlapped with water due to the residual 10% protonation left in the protein sample. A total of 18 sites were deemed quantitative and could be mapped to the protein structure (Figure 4-7).

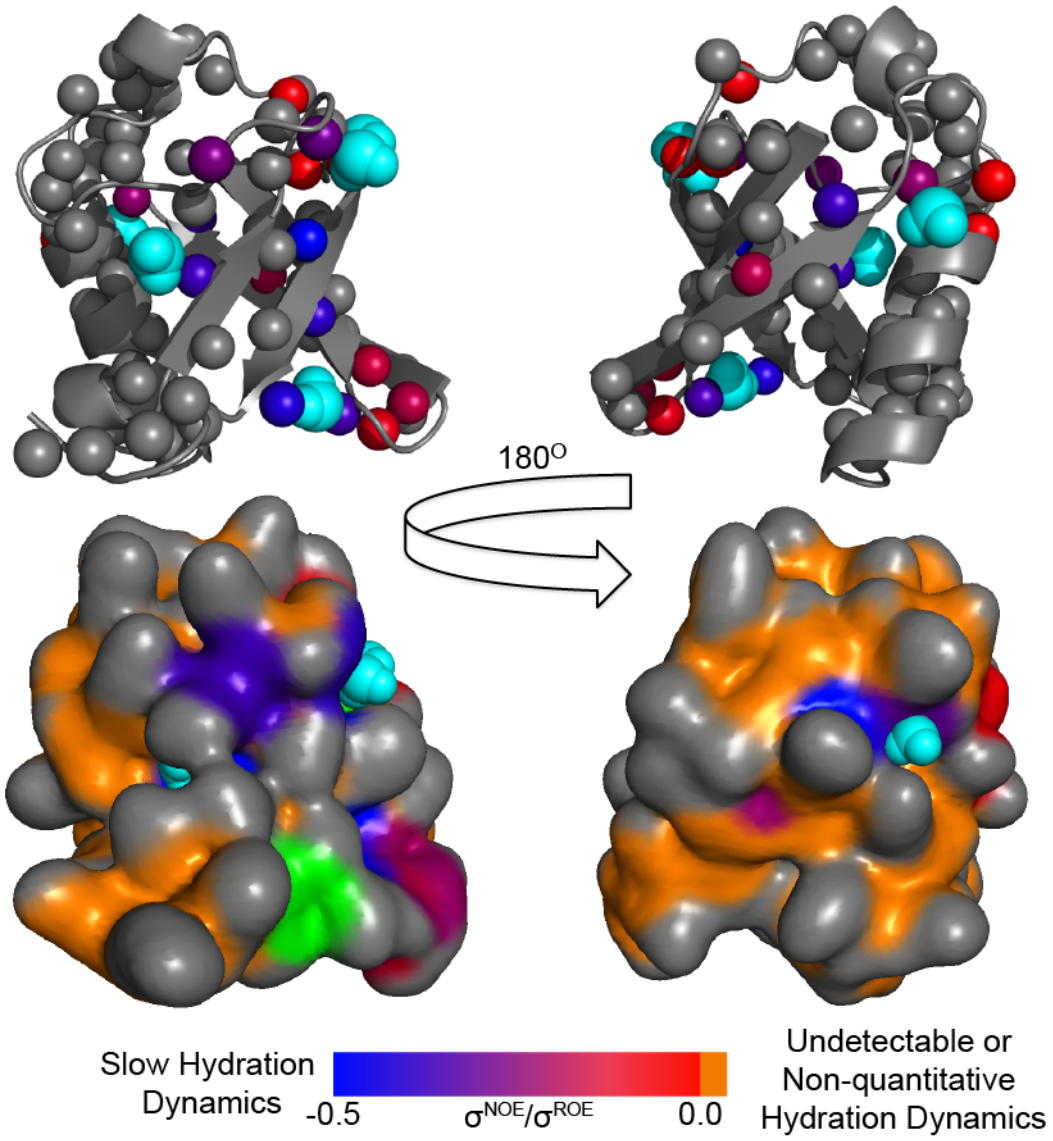

Figure 4-7: The calculated $\sigma^{NOE}/\sigma^{ROE}$ ratios were mapped to the protein surface of Ubiquitin in AOT reverse micelles (PDB accession 1G6J/Conformer25). The top shows the cartoon illustration with all amides shown as spheres. Spheres are colored red to blue for fast to slow hydration dynamics detected via the NOE. Crystallographic waters are shown in cyan spheres. The bottom shows the surface representation using the same color scheme as above. The regions in green have detectable hydration dynamics via the NOE, but are outside of the theoretical limit of -0.5. Orange regions are sites that have amides within 4Å of the surface but don't have a quantitative $\sigma^{NOE}/\sigma^{ROE}$ ratio.

Several different regions of slow waters are identified. Ubiquitin has two partially buried water molecules detected crystallographically. The first water molecule, WAT1, is hydrogen bonded between Leu43 amide and the Lys27 side chain. The Leu43 amide has a detectable $\sigma^{NOE}/\sigma^{ROE}$ ratio at the bound limit. Unfortunately, the amide of Leu50 is overlapped with Phe45 and an $\sigma^{NOE}/\sigma^{ROE}$ ratio was unable to be analyzed with this current data set. Similarly, the amide of Glu51 has a slow $\sigma^{NOE}/\sigma^{ROE}$ ratio but was not considered in our analysis because it is within 4Å of the non-decoupled Tyr59 residue. Denisov *et al.* previously identified this water residue as being the only slow water molecule in Ubiquitin in magnetic relaxation dispersion experiments (MRD) (190, 191). This water residue was shown to be slowed in several MD simulations (28, 63). The experimental MRD results provide dynamic information, but do not provide spatial resolution. Here, the presence of this long-lived water is confirmed and slow hydration dynamics are detected via the $\sigma^{NOE}/\sigma^{ROE}$ ratio. An additional partially buried water molecule WAT2 is visible in the crystal structure and is hydrogen bonded to amides of Leu8 and Leu 71. Several sites surrounding this water molecule have slow detectable $\sigma^{NOE}/\sigma^{ROE}$ ratios including Leu8, Leu71, and Leu69. Several other clusters of slow waters are identified using the $\sigma^{NOE}/\sigma^{ROE}$ ratios. Nearly all of these sites reside in highly curved pockets in on the surface structure. Depth of burial was not correlated with the overall slowing of protein hydration. Surface curvature and local topology has been hypothesized as a driving force for the slowing of waters at the protein surface (30, 34, 133, 192, 193). The data presented here are in agreement with this hypothesis. However, these findings could be confounded with the choice of detection probe for the NOE since amides are generally

involved in secondary structure hydrogen bonds and are not surface exposed. As the depth of burial of detected NOEs are within 1-3.5 Å this doesn't seem likely. Additionally, all amides in Ubiquitin are less than 5 Å from the protein surface. More protein systems are necessary to understand the role of surface curvature on protein hydration.

Conclusions

The lack of methods for measuring surface hydration dynamics of proteins in a site and time resolved manner has left a great hole in the biophysical puzzle. In this present study we improve upon NMR methods for the detection of protein hydration via the NOE. Hydrogen exchange relay artifacts from side chain hydroxyls have remained a major artifact in NOE detected hydration experiments. The unique environment of the reverse micelle slows these exchange rates such that they are on the slow chemical shift NMR timescales. We have shown that these hydroxyls can be selectively decoupled during the NOE mix time. The contribution from hydrogen exchange cannot be decoupled during the ROE experiments. Therefore, we introduce a new data fitting method that allows for calculation of $\sigma^{NOE}/\sigma^{ROE}$ ratios without contribution from exchange relay. This method was applied to Ubiquitin in AOT reverse micelles.

The data presented here are in agreement with many previous experimental and computational studies of Ubiquitin hydration. Additionally, many other sites were detected that have slow hydration relative to previously studies. In addition to partially buried waters the NOE detects regions of surface hydration that are slow. The slowed waters of Ubiquitin tend to cluster around the surface of the protein. Slowed waters reside

in concave regions of the protein. This is in good agreement with other experimental and computational studies of surface hydration. The experiments outlined here provide the only method of measuring protein hydration with site and time resolution without mutating the protein. Artifact free measurement using the NOE requires reverse micelle encapsulation.

Chapter 5: Conclusions and Future Directions

The goal of this thesis was to apply and improve upon methods that use NMR spectroscopy and reverse micelle encapsulation of proteins to study protein hydration dynamics. NMR provides the only experimental technique that provides both site resolution and dynamic information on native proteins. The methods presented show that protein-water interactions detected via the NOE can be applied to a wide range of biophysical questions that necessitate different levels of quantitation. Several different ways of collecting and analyzing NOE data are introduced. The final method introduced provides the only means of site resolved hydration dynamics measurement of native protein in the absence of artifact.

Chapter 2 measured protein-water interactions of SNase Δ+PHS and several of its mutants in CTAB/hexanol reverse micelle. Water penetration into the hydrophobic core of SNase mutants with internal ionizable groups has been highly debated. NOE hydration measurements were applied to identify whether water is able to penetrate into the hydrophobic core of SNase. Unlike other methods, the NOE is able to detect nearby positionally disordered waters. Protein-water NOE's were detected throughout the entire hydrophobic core, including to sites that are >4 Å from nearby crystallographic waters. Additionally we were able to show that no major changes to protein structure or dynamics occurred. These measurements were used only to identify the presence of internal waters and did not require high levels of quantitation. Therefore, only a single mix period was used. This allowed for relatively fast data collection and the ability to study multiple mutants in a tractable amount of time.

Chapter 3 aims to develop faster methods for the detection of protein-water NOEs. Hydration dynamics experiments are generally low in signal-to-noise and require long data collection times. NUS sampling was implemented to traditional three-dimensional NOESY-HSQC experiments. Two-dimensional water selective experiments were also implemented. Both of these methods allowed for an over 4-fold time savings. We benchmarked the reliability of NOE crosspeaks under these conditions and the reproducibility of hydration dynamics $\sigma^{NOE}/\sigma^{ROE}$ ratios both within and between samples. Finally, a new method for data fitting that allows for the detection of $\sigma^{NOE}/\sigma^{ROE}$ ratios without assumptions about the relaxation behavior of the water and protein was introduced. The methods presented in Chapter 3 are sufficient for quantitative hydration dynamics of buried waters or surface hydration of sites >4 Å from a Ser/Thr/Tyr hydroxyl.

In Chapter 4 tackles one of the longstanding artifacts affecting protein hydration measurements via the NOE. Hydrogen exchange and hydrogen exchange relay, though slowed relative to bulk, are still present in the reverse micelle. Hydrogen exchange relay artifacts can be removed from NOE spectra by selective decoupling of hydroxyl peaks during the mix time. A new data fitting method to calculate $\sigma^{NOE}/\sigma^{ROE}$ ratios of sites near hydroxyls without contamination from hydrogen exchange is presented. Partially buried waters are reliably detected. Additionally, we show that slowed surface waters tend to reside in concave regions of the protein. The data analysis and time requirements of the experiments are relatively slow and complex. However, these methods provide the only

means of measuring surface hydration dynamics with site resolution and time resolution that are devoid of artifact.

The work in this thesis has focused on methods development for the data collection and analysis of protein hydration detected via the NOE. These advancements focused on decreasing the amount of experimental time needed to collect these experiments, as well as improving the data collection and fitting to provide artifact free measurements. The techniques presented here offer the only site and time resolved measurements of protein-water interactions of native state protein. Despite this, one can envisage much additional technical advancement that might increase the utility of these measurements. To date, most proteins can be reliably encapsulated in at least one of the well-used surfactant mixtures. The identification of novel surfactant mixtures as well as biophysical characterization of existing mixtures will help ensure that all proteins can be encapsulated in an ideal surfactant mixture under ideal conditions such as pH and W_o. The NMR experiments used have fairly low signal-to-noise ratios which increase experimental time. Optimization of pulse sequences to increase signal-to-noise will be advantageous for broad application of these techniques. Additionally, the experiments presented here rely on shaped pulses, which have imperfect excitation. The "top hat" pulses presented in Chapter 4 provide the most uniform excitation over a given bandwidth, and only marginally affect off-bandwidth frequencies. Development of new pulses that do not affect off-bandwidth frequencies would remove the need to correct for κ during the decoupling experiments and further increase the precision of the measurements. Finally, the experiments presented here rely on amide or methyl detection. While these protons

are distributed across the entire protein they generally tend to reside on the protein interior. Novel isotopic labeling schemes and NMR detection schemes will facilitate a much larger range of detectable surface probes specifically on the surface of the protein. The work presented here outlines several different strategies for applying the NOE to measure protein-hydration. An outline of how to collect these experiments, as well as the different considerations for each type of application are described in Appendix A. Each of these strategies was applied to a model protein system and general trends were observed. However, water plays roles in many aspect of protein function. In order to truly understand the thermodynamic role that water plays in protein function it will be necessary to measure hydration dynamics on many proteins, in order to address different aspects of protein-water interactions. The data presented here are in good agreement with many other biophysical and computational methods but are able to provide more information. By adding NMR detection of protein-water interactions to the biophysicist's toolbox in combination with other well-established methods, we hope that the role of water on protein function will be elucidated in a quantitatively rigorous and comprehensive way.

Appendix A: General method for measuring protein hydration

General protocol for measuring hydration in a small protein

Hydration dynamics experiments can be performed on any protein that is stable in the reverse micelle. Here, we illustrate the general procedure that was used for measuring surface hydration dynamics of Ubiquitin in AOT reverse micelles. Ubiquitin is an 8.3 kDa protein that encapsulates stably for up to several years (119). The procedure described below, including data fitting can be applied to any small protein that can be 100% perdeuterated. If larger proteins are studied then TROSY detection schemes and changes in NOE and ROE mix times should be changed accordingly. Similarly, if the protein cannot be fully perdeuterated changes some potential changes will be identified.

1) Determine optimal encapsulation conditions using ^{15}N protein. Please see Fuglestad *et al.* for a comprehensive description of how to screen and benchmark encapsulation conditions (115).
2) Assign protein in the reverse micelle using $^{13}C^{15}N$ protein using standard triple resonance experiments (e.g. HNCA, HNCOCA, HNCO, HNCACO, HNCACB, CBCACONH) (194)
3) Express protein of interest in 99%-D_2O M9 with $^{15}NH^4Cl$ as the sole nitrogen source and purify (165). Once purified dialyze extensively against water and lyophilize.
4) Dissolve protein in 6.75 uL (W_o=10, 75mM surfactant, 500uL sample) buffer containing 10mM NaAcetate, 10mM NaCl, pH 5 (137, 195).

5) Prepare reverse micelle sample for hydration dynamics using 100% deuterated alkane as the bulk solvent
6) Collect 3D ^{15}N-NOESY-HSQC to assign T/S/Y hydroxyl protons and determine decoupling bandwidth needed for all hydroxyls (~4.7-6.2ppm)
7) Setup G3 (188) decoupling pulses using STDISP. A 10 ms decouple pulse will cover a bandwidth of 0.6ppm. Use two decouple pulses centered at 5.4 and 6.1ppm to cover the bandwidth of 5.1-5.7ppm and 5.8-6.4ppm, respectively
8) Measure 2D NOESY-HSQC's with and without one 360^{o} rotation during the mix using the calibrated G3 pulses. The mix time should be relatively long (e.g. 100ms) to increase signal-to-noise. For fully perdeuterated protein a short water-selective inversion pulse should be used. For protein that is not fully perdeuterated the water-selective inversion pulse should be relatively long (>50ms) to allow for protein H_{α}'s to relax. This removes contamination from overlapped intra-protein NOE's
9) Determine the κ correction factors for each of the selective pulses (189). Plot a histogram of the ratio of decoupled vs. not decoupled peak height intensity. Identify the top 10% of peaks and plot the decoupled versus not decoupled peak height intensities. The slope of the linear regression line is the κ correction factor. This slope should be >0.95
10) Collect 2D water-selective (182) ^{15}N-NOESY-HSQC, ^{15}NROESY-HSQC, and ^{15}N-NOESY-HSQC with G3 decoupling. Mix times for the NOE and decoupled-NOE experiment are 20, 40, 60, 80, 100, 140, 180, 240, 300, 500ms. Example

mix times for the ROE would be 10, 15, 20, 25, 30, 35, 40, 50, 75, 150ms. For fully perdeuterated protein a short water-selective inversion pulse should be used. For protein that is not fully perdeuterated the water-selective inversion pulse should be relatively long (>50ms) to allow for protein H_α's to relax. This removes contamination from overlapped intra-protein NOE's. A weak CW spinlock with a bandwidth of 8.3-10kHz should be used for the ROESY-HSQC experiment.

11) Correct the NOE-decoupled peak height intensities with the determined κ value.
12) Fit the data as described below and calculate NOE/ROE rates.

Data fitting

Buried internal waters without quantitative dynamics

Structural or buried waters can easily be detected by the NOE. If no dynamics information is needed the σ^{NOE} and σ^{ROE} can each be collected using a single mix time. If perdeuterated protein is used the experiment can be collected in either two or three-dimensional experiments. If protonated protein is used the two-dimensional water selective experiments with a long water selective pulse is recommended to remove contamination from H_α. If short mix times are used (~20ms) a rough approximation of how long lived the waters are can be obtained by taking the ratio of the peak height intensities (I_{NOE}/I_{ROE}).

Dynamics of buried waters or surface waters >5Å from hydroxyls.

If full buildups for the NOE, ROE, and G3 experiments cannot be performed, or of the hydroxyls cannot be assigned the NOE/ROE method can still be used on buried waters or

sites that are >5A from the nearest hydroxyls. Matched mix time NOESY-HSQC and ROESY-HSQC experiments should be collected (94, 96). The data fitting relies on linear regression and therefore 4 mix time points are recommended. The mixing time is not restricted to the linear regime. The ROE experiments will have contributions from auto-relaxation, even at short mix times. To calculate out the $\sigma_{NOE}/\sigma_{ROE}$ ratio in the absence of relaxation multiple mix times are needed. The natural log of the I_{NOE}/I_{ROE} as a function of mix time (τ_{mix}) is fit to a line with the slope equal to the auto-relaxation rates and the intercept equal to the $\sigma_{NOE}/\sigma_{ROE}$ as shown in Equation 5-2

$$\frac{I_{NOE}(\tau_m)}{I_{ROE}(\tau_m)} = \frac{\sigma_{NOE} e^{-R_1 \tau_m}}{\sigma_{ROE} e^{-R_{1\rho} \tau_m}} \quad 5\text{-}1$$

$$\ln[-\frac{\sigma_{NOE} e^{-R_1 \tau_m}}{\sigma_{ROE} e^{-R_{1\rho} \tau_m}}] = \ln[-\frac{\sigma_{NOE}}{\sigma_{NOE}}] + (R_{1\rho} - R_1)\tau_m \quad 5\text{-}2$$

The linear regression fitting is generally simple and robust.

Surface waters

Full buildup curves for the NOE, ROE, and decoupled-NOE must be collected (97, 105, 107, 160). The curves for the NOE, ROE, and decoupled-NOE experiment need to be individually fit to Equations 1-6 and 1-7. Unfortunately due to the similar timescales of σ^{NOE} and R_1 (σ^{ROE} / $R_{1\rho}$) these equations are difficult to fit for directly. Fortunately, the A_o term is constant for all experiments assuming identical acquisition parameters and good sample stability. In order to simplify the data fitting the *Ao* term can

be determined using a global fit of the NOE data and held constant for the remaining curves. A global fit of the A_o term is accomplished by fitting crosspeaks with mixing times in the linear regime of the NOE buildup by using a simplified version of Equation 5-3:

$$I_{NOE} = A_o(1 - e^{-\sigma_{NOE}\tau_m}) \qquad 5\text{-}3$$

Once the A_o term is determined it can then be held constant and each experiment is then fitted to the full NOE buildup and Equation 5-3 using the first few points. Fitting to Equation 5-3 requires less parameters and is an easy fit. However, because it is constrained to peaks in the linear range the signal-to-noise may be low. In cases where the linear regime is too noisy the full buildup allows sampling at longer mix times and therefore greater signal-to-noise. However, the relaxation term R_1 of the full equation fitting may be skewed due to the overcorrection due to κ at long mix times.

Once the observed σ^{NOE}, σ^{ROE}, and σ^{NOE}_{dec} rates are calculated the NOE/ROE ratio can be determined. For sites that are not contaminated by exchange relay the ratio of the fitted rates is sufficient. For sites that contain exchange relay one must fit the σ^{NOE} and σ^{ROE} to Equations 5-4 and 5-5. The difference of the cross relaxation rates between the NOE experiment and the decoupled-NOE experiment give the contribution from HX relay:

$$(\Sigma k_{ex} \bullet \sigma^{intra}_{NOE}) = \sigma^{dec}_{NOE} - \sigma_{NOE} \qquad 5\text{-}4$$

The intramolecular ROE is 2x the NOE, therefore the HX contribution is 2x greater for the ROE than the NOE. The ROE can be calculated using:

$$\sigma_{ROE} = \sigma_{ROE}^{obs} - 2(\Sigma k_{ex} \bullet \sigma_{NOE}^{intra}) \quad 5\text{-}5$$

The NOE/ROE ratios can then be calculated. All ratios should fall within -0.5-0. As a general rule this data fitting method must includes at least 5-10 different mix times per experiment type. The choices in mix time does not need to be matched for the different experiments as each curve will be fit independently. It is recommended that atleast half of the data points collected are within the linear regime of the NOE and ROE buildups.

General sample considerations

Protein growth and purification

The choice of protein labeling schemes will depend on the regions of protein that are of interest (step 3 of general protocol). One of the biggest considerations when preparing protein for hydration studies is the need for high perdeuteration levels (165). The reasons for this are multifold. Perdeuteration suppresses spin diffusion and reduces longitudinal relaxation thereby providing purer cross relaxation and access to longer NOE/ROE mixing times. The latter is helpful for obtaining higher signal-to-noise (S/N) cross peaks and sampling broader sampling of the time dependence. The ROE experiments require transverse magnetization and is therefore sensitive to $R_{1\rho}$ relaxation. Perdeuteration drastically reduces this relaxation rate. Extensive perdeuteration also largely eliminates spin-diffusion, which maintains the local nature of the NOE even at longer experimental mix times. Additionally, H_α protons may resonate at frequencies similar to or overlapped with water. Therefore an intra-molecular cross peak from a H_α that is overlapped with water may be mistaken for an inter-molecular protein-water NOE.

The intra-molecular NOE is much stronger than an inter-molecular NOE and therefore high (~99%) deuteration levels are recommended. If such high perdeuteration levels cannot be obtained a high-resolution structure in combination with H_α assignments can be used to remove any potential contaminant peaks from the analysis. If a high-resolution structure is not available more complicated pulse schemes may also be used to remove signals from H_α's, and will be discussed below.

The simplest isotopic labeling scheme uses uniform ^{15}N-labelling in an otherwise 99%-^{2}H background using $^{15}NH_4Cl$ as the sole nitrogen source during growth (196, 197). ^{15}N-labelling is relatively inexpensive and provides a probe on every residue within a protein. This facilitates good detection coverage of protein-water NOE's across the entire protein. However, since most amides are involved in secondary structure hydrogen bonds, many may be too far from the protein surface or internal cavities to provide enough information. Selective methyl labeling can provide additional coverage both on the surface of the protein and especially in the hydrophobic core of the protein. $^{13}CH_3$-ILV,^{12}C,^{2}H,^{15}N labeling can be easily obtained by adding α-ketobutyrate and α-isoketovalerate precursors 1-hour before induction. While not as commonly used selective methyl labeling of alanine, threonine, and methionine residues, as well as selective ^{13}C,^{1}H labeling of aromatic residues in a deuterated background can be used (197-200).

Once the isotopically labeled protein is purified it needs to be prepared for reverse micelle encapsulation. This requires removal of excess salt and buffers prior to concentration. Depending on the isoelectric point of the protein and the pH used during

purification the protein can still contain a high concentration of counter ions. High salt concentrations can interfere with reverse micelle encapsulation (201). Additionally, many buffer molecules can catalyze hydrogen exchange thereby increasing the hydrogen exchange contaminants in the reverse micelle (162). If possible, it is best to dialyze dilute protein extensively against water and then lyophilize prior to the preparation of reverse micelles.

Once dry the protein can be resuspended in small amounts of the buffer that will be used in the reverse micelle. The final pH of the reverse micelle sample (buffer and surfactant) should be kept relatively low in order to reduce hydrogen exchange. In general a pH of ~5 is optimal for low hydrogen exchange rates of amides and side chains (161). It is important to stay away from phosphate buffers because even modest concentrations can increase hydrogen exchange rates dramatically. Other buffers such as acetate, a commonly used buffer at pH 5, only mildly increase hydrogen exchange rates and are safe to use at low concentrations. Verify and monitor pH once the sample is made (137).

Reverse micelle encapsulation and considerations

Proteins must be stably encapsulated in reverse micelles for hydration measurements using the NOE. For an in-depth description of benchmarking protein encapsulation refer to Fuglestad *et al.* A 3D ^{15}N-NOESY-HSQC should be collected on an encapsulated protein to verify that the protein is not interacting with the surfactant shell. A well solubilized protein in its native hydration shell will not have any detectable NOE's between the protein and the surfactant. If protein-surfactant NOE's are detected the

surfactant mixture or encapsulation conditions should be changed. If the protein cannot encapsulate in other mixtures only buried or structural waters should be studied. If CTAB/hexanol is used care should be taken to resolve the water and hexanol hydroxyl peaks in the 1D ^{1}H-spectrum. The ^{15}N-NOESY-HSQC should be used to verify that no crosspeaks exist between the protein and hexanol hydroxyl. This can be accomplished by decreasing the hexanol concentration, increasing the temperature, or reducing the concentration of surfactant. Protonated surfactants can be used for ^{15}N-detected experiments. For ^{13}C detected experiments deuterated surfactants should be used to avoid streaking and spectral artifacts.

The NOE/ROE hydration experiments are relatively insensitive and so the reverse micelle sample must be stable for several weeks in order to collect data of sufficient quality. If a protein itself is stable in a reverse micelle then the greatest source of RM sample instability comes from evaporation of either the pentane or buffer. This can be mitigated by using moderate experimental temperature (e.g. 20^{o}C) and plugging the sample with a vortex plug. Record 1-dimensional ^{1}H spectra periodically through the course of the experiments to make sure no changes occur in the peak height or frequency of the water peak or buffer peaks.

Appendix B: Materials and Methods

Chapter 2

Protein Purification

SNase Δ+PHS and mutants was expressed as previously(202) described in M9 minimal media with $^{15}NH_4Cl$ as the sole nitrogen source. Reverse micelle encapsulation condition screening was performed using ^{1}H,^{15}N-protein as described by Fuglestad *et al.* (115). Chemical shift assignments were collected using ^{1}H, ^{13}C, ^{15}N protein by using $^{13}C_6$-labeled glucose as the sole carbon source. Protein hydration and dynamics measurements were performed on ^{2}H, $^{13}CH_3$-ILV, ^{12}C, ^{15}N-SNase grown in 99%-D_2O and adding α-ketobutyrate and α-ketovalerate precursors 1 hour before induction (200). Cells were grown at 37^{o}C until OD_{600} reached 0.8, and induced with 1 mM IPTG for 4 hours. Induced cells were harvested and sonicated in buffer containing 6M Urea, 25mM Tris, 2.5mM EDTA, pH8.0. The sonicate was spun down and the supernatant was run over an SP sepharose fast flow column and eluted with a NaCl salt gradient (0-400 mM) and collected. Fractions containing pure protein were collected and dialyzed against 4L of 1M KCl overnight to refold. Refolded protein was subjected to four rounds of dialysis against 4L of water. Small quantities of 0.1mM HCl were used to change the pH of the protein and final dialysis solution to pH 5.3. Protein was divided into 1mg aliquots, flash frozen in a dry ice/ethanol mixture, and lyophilized until dry. Protein purity was confirmed by SDS-PAGE and mass spectrometry. All unlabeled chemicals were purchased from Sigma-Aldrich (St. Louis, MO) and all isotopically labeled chemicals were purchased

from Cambridge Isotope Laboratories (Andover, MA). Site directed mutagenesis for V66E and I92E mutants were engineered from SNase Δ+PHS using Agilent quick-change kits (Santa Clara, CA) and sequenced.

Protein Encapsulation

Lyophilized SNase was resuspended in 13μL of 50mM NaAcetate, 50mM NaCl, 20uM DSS, 0.05% NaAzide, pH 5.3. Reverse micelles were prepared by injecting 13.0 μL (target Wo=20) of concentrated SNase, into a mixture of 60 mM cetyltrimethylammonium bromide (CTAB)/450mM hexanol and 550 μL of 99% (*d-12)* deuterated pentane, and vortexed until clear. Reverse micelles for encapsulation tests and assignment experiments used uniformly ^{1}H surfactants. Hydration and dynamics experiments used d_{13}-N-hexanol and d_{42}-cetyltrimethylammonium bromide to remove proton surfactant signals in the methyl region. The reverse micelle solution was transferred to a Wilmad screw cap tube and a vortex plug was placed on the sample-air interface during NMR data acquisition. SNase reverse micelle samples remain stable for >6 months under those conditions. Deuterated surfactants were purchased from Cambridge Isotope Laboratories (Andover, MA)

NMR spectroscopy

All NMR experiments were performed on either 500 or 600 MHz Bruker Avance III spectrometers equipped with TXI cryoprobes. All spectra were recorded at 293 K and referenced to dimethyl-silapentanesulfonate (DSS, Sigma). Backbone assignment data were collected at 600 MHz using gradient-selected sensitivity-enhanced ^{15}N-HSQC,

HNCA, HNCOCA HNCACB, CBCACONH, HNCO and HNCACO experiments with proton carrier on water (194). Backbone assignments were collected in both aqueous solution and in the reverse micelle samples. Chemical shift perturbations of mutants were calculated by using Equation 5-1

$$CSP = \sqrt{(H_{ppm}^{WT} - H_{ppm}^{mut})^2 + 0.1(N_{ppm}^{WT} - N_{ppm}^{mut})^2} \quad 5\text{-}1$$

ILV-Methyls were assigned in aqueous solution and mapped to the reverse micelle. Methyl assignments were performed using a ^{13}C-HSQC and MQ-(H)CCH-TOCSY with a 13.2ms FLOPSY spinlock using a 7.5kHz ^{13}C spinlock field strength (203). All assignment data were collected using 10%-non-uniform sampling in the indirect dimensions. Sampling schedules were created using Poisson-Gap sampling. Backbone assignments were collected in an aqueous reference sample as well as the reverse micelles. All hydration and dynamics experiments were collected at 500 MHz. Both ^{15}N and ^{13}C sensitivity enhanced NOESY- and ROESY-HSQC's were collected. WET suppression was used on ^{13}C-detected experiments to eliminate spectral artifacts arising from residual pentane protonation (163). ROESY-HSQC's used an 8.3kHz bandwidth continuous wave spinlock with a 90_y-Sly-90_y motif during the mix to eliminate frequency offset artifacts (98). Proton carrier was set to 5.5 ppm and 2.8 ppm for ^{15}N- and ^{13}C-detected experiments, respectively. No water suppression was used. A 30 ms and 40 ms mixing time was used for ^{15}N and ^{13}C-detected experiments, respectively. All experimental parameters including pulse durations and scans were matched for NOESY-HSQC and ROESY-HSQC pairs. Hydration experiments were collected using 25% non-uniform sampling in both indirect dimensions. Sampling schedules were created using

Poisson-Gap sampling (173, 204). Protein dynamics on the μs-ms time scale were measured using the TROSY Hahn Echo method as introduced by Palmer (167). The 2/J value was set to 10.8ms. Intensities were measured with 2-D experiments collected in triplicate (I_α, I_β, I_zS_z). ^{15}N R_1 measurements were performed as a series of 2D experiments with 9 delay times ranging from 28-750ms with 3 duplicates. Rates were fitted to a single exponential decay. The value <κ> was obtained from the trimmed mean of amides not exhibiting chemical exchange. R_{ex} was calculated using the Equation 5-2 as described by Palmer:

$$R_{ex} = R_2^{\alpha} - R_1^{2HzNz}/2 - \eta_{xy}(\kappa - 1) + R_1^N/2 \qquad 5\text{-}2$$

Errors in R_{ex} were calculated by error propagation using RMS noise of the spectra. Dynamics on the ps-ns timescale were measured using the heteronuclear NOE. H-N NOE values were taken as ratios of intensities with and without saturation. A relaxation delay of 5 s was used to ensure full relaxation of water (166). Errors were calculated by error propagation using the RMS noise of the spectra. All spectra were processed using NMRPipe and analyzed in Sparky (205).

Data Processing and molecular visualization

All calculations were performed using in house scripts written in Python with standard packages including numpy, matplotlib, and scipy, or in GraphPad Prism. All visualization was performed in PyMol (Delano Scientific) (206) using PDB accession numbers 3BDC, 5KIX, and 5EGT for SNase Δ+PHS, SNase Δ+PHS/I92E, and SNase Δ+PHS/V66E respectively. Amide hydrogens were added to the structures using VMD.

Chapter 3

Protein Purification and Reverse Micelle Encapsulation

The gene for wild-type human ubiquitin was cloned into the pET11a expression vector (Genscript) and expressed in BL21(DE3) E. coli cells in M9 minimal media. Ubiquitin used for sampling density measurements were grown in 100% H_2O and ^{13}C d-glucose and $^{15}NH_4Cl$ as the sole carbon and nitrogen sources for uniformly labeled U- [$^{13}C^{15}N$]-ubiquitin. Ubiquitin used to determine NUS hydration reproducibility were grown in 95% D_2O and $^{15}NH_4Cl$ as the only nitrogen source to yield ~90% ^{2}H, U- [^{15}N] ubiquitin. The protein was then extracted from inclusion bodies, purified, and refolded as previously described(121). After purification, the protein was extensively dialyzed against pH 5.0 adjusted water and lyophilized in 1 mg aliquots. Aqueous samples were made with U-[$^{13}C^{15}N$]-ubiquitin resuspended in buffer (50 mM sodium acetate pH 5.0 with 50 mM NaCl) to a final concentration of 1 mM. To create stable reverse micelle samples *(119)*,each aliquot of 90% ^{2}H, U-[^{15}N] ubiquitin was dissolved in the proper amount of buffer (50 mM sodium acetate pH 5.0 with 50 mM NaCl) in order to create a reverse micelle using the direct injection method*(116)* with a molar water to surfactant ratio (water loading or W_0) of 10 using 75 mM bis(2-ethylhexyl)sulfosuccinate (AOT) as the surfactant and 99% deuterated pentane (d-12) as the solvent. The pH of the AOT was pre-adjusted to 5.0 *(137)* in order to ensure the aqueous nanopools were at an average pH of 5. All isotopically labeled materials were obtained from Cambridge Isotopes (Andover, MA) and all unlabeled chemicals were purchased from Sigma-Aldrich (St. Louis, MO). Three separate reverse micelle samples were made.

NMR Spectroscopy and Experimental Setup

All aqueous samples were collected at 25°C on a 500 MHz (^{1}H) Bruker AVANCE III spectrometer equipped with a TXI cryoprobe. ^{15}N-resolved, sensitivity-enhanced NOESY-HSQC (207) was collected on U-[^{13}C^{15}N]-ubiquitin with an NOE mix period of 100ms. Each experiment was collected with 32 scans per free induction decay with 24 and 64 complex points in nitrogen and indirect protein, respectively. Spectral widths were 10504.20 Hz (F3, ^{1}H), 1414.696 Hz (F2, ^{15}N) and 5982.8 Hz (F1, ^{1}H-indirect), corresponding to sweep widths of 21, 28, and 12, respectively. All data was collected with a 97.5 ms acquisition time and an interscan recycle delay of 1 sec. Non-uniformly sampled data was collected with both indirect dimensions collected non-uniformly. Sampling schedules were generated using the PoissonGap2program (175) and were not tested or optimized before use. A total of 8 experiments were collected, 2 uniformly Cartesian sampled (US), and 6 non-uniformly sampled (NUS) data sets at 5, 10, 15, 20, 25, 25% sampling density in the indirect dimensions, respectively.

All reverse micelle data were collected at 20°C on a 500 MHz (^{1}H) Bruker AVANCE III spectrometer equipped with a TXI cryoprobe. ^{15}N-resolved, sensitivity-enhanced NOESY-HSQC (89, 94, 196, 207) and ROESY-HSQC (96, 97, 108) were collected on uniformly ^{15}N-labeled, ~90% perdeuterated ubiquitin encapsulated in AOT reverse micelles as described above. All three-dimensional (3D) NOESY-HSQC and ROESY-HSQC spectra were collected at 25% Poisson-gap sampling with non-uniformly sampled (NUS) versions of the pulse sequences (173, 175) with 32 scans per free induction decay with 50 and 64 complex points in the nitrogen and indirect proton dimensions,

respectively. Spectral widths were 10504.20 Hz (F3, ^{1}H), 1666.921 Hz (F2, ^{15}N) and 5482.9 Hz (F1, ^{1}H-indirect), corresponding to sweep widths of 21, 33, and 11, respectively. The ROESY experiments used a 8.33 kHz continuous wave spin-lock field as previously described (125, 126). Three reverse micelle samples were used and each sample was collected at a single N(R)OE mix time in duplicate. Additionally, one sample was collected at multiple mix points (20, 40, 60, 80 ms) in order to perform a full NOE buildup curve. Two dimensional experiments were collected with spectral widths of 10504.20 Hz (F2, ^{1}H) and 1666.921 Hz (F1, ^{15}N) corresponding to sweep widths of 21 and 33 ppm for proton and nitrogen, respectively. Experiments were collected with 512 scans per free induction decay and a 48 complex points in nitrogen. The water selective pulse was a 15ms Sinc pulse center around water. The inter-scan delay was set to 1 second.

All spectra were processed in NMRPipe (208) using the istHMS reconstruction algorithm for non-uniformly sampled data (175) with a threshold of 98% and 400 iterations. All water (4.5 ppm) cross-peak intensities were determined using Sparky (205). S/N ratios were determined as the max peak intensity divided by the RMS_{NOISE} across the entire spectrum. All further analysis was completed using standard data fitting software or in house Python Scripts.

Chapter 4

Reverse Micelle Encapsulation

Glucose was encapsulated in AOT and CTAB/hexanol reverse micelles. The pH of 2M glucose in the absence of buffer was adjusted using small quantities of 0.01M HCl and

0.01M NaOH. The pH of AOT reverse micelles was pre-adjusted as described previously. Glucose reverse micelles containing sodium acetate and sodium phosphate were collected at pH 5. All reverse micelle samples were made with 75mM surfactant with a W_o of 20. A total of 15 μL of stock glucose solution was added for a final glucose concentration of 50mM in the reverse micelles. AOT reverse micelles were prepared as described in Chapter 3 except that only 10mM NaAcetate buffer was used to reduce overall hydrogen exchange rates.

NMR Spectroscopy and Experimental Setup

All experiments were collected at 20^{o}C on a 500 MHz (^{1}H) Bruker AVANCE III spectrometer equipped with a TXI cryoprobe. Hydrogen exchange rates of glucose in reverse micelles was collected using standard EXSY experiments. One-dimensional water selective NOE experiments using the e-PHOGSY scheme with gradient pulses was used. The Bruker pulse pack "SELNOGP" was converted into a pseudo two-dimensional experiments. Proton spectral widths were 10000 Hz corresponding to a 20 ppm sweepwidth and 128 transients per FID were collected and the inter scan delay was set to 2 seconds. The water selective pulse consisted of a 15ms SINC pulse. A total of 20 delays were used consisting of 3, 4, 6, 8, 10, 12, 14, 16, 18, 10, 12, 14, 16, 18, 20, 25, 30, 40, 50, 75, 100, 150, 200, 500, 800 with 3 duplicates. ^{15}N NOESY-HSQCs, ROESY-HSQCs, and NOESY-HSQCs with decoupling were collected as a series of pseudo three-dimensional water selective experiments. Each experiment was collected with 96 transients per fid and 48 complex points in nitrogen with spectral widths of 10000 Hz and 1620 Hz corresponding to 20 ppm and 32 ppm for proton and nitrogen, respectively.

Selective water excitation was achieved using a 15ms SINC pulse. Decoupling of hydroxyls was accomplished using a 10ms G3 inversion pulse. Each G3 inversion loop consisted of one 360^{o} rotation and was 20 ms long. Each G3 pulse has a bandwidth of ~0.6 ppm, and decoupling experiments were centered at 5.7 and 6.1 ppm. NOE and decoupled NOE experiments were collected with mix times of 20, 40, 60, 80, 100, 140, 180, 240, 300, 400, 550, 750, 1000. ROE experiments were collected with mix times of 10, 15, 20, 25, 30, 35, 40, 45, 50, 60, 70, 80, 90, 110, 130, 150, 250 ms. Experiments for determining the κ correction factor were set at 80 and 140 ms mix times with a 20ms 360^{o} pulse in the middle of the mix period.

Data fitting

All spectra were processed in NMRPipe (208). Glucose peak height intensities were determined by using the NMRDraw module of NMRPipe. Protein crosspeak intensities were determined using Sparky (205). In house python scripts were used to fit glucose hydrogen exchange rates according to Equation 5-3:

$$A_o(1-e^{-k_{ex}\tau})e^{-R_1\tau} \qquad 5\text{-}3$$

All data fitting for Ubiquitin was performed using GraphPad Prism.

Structural Surface Analysis

The trigen and trisrf algorithms (209) were implemented on the structure of ubiquitin encapsulated in AOT reverse micelles (PDB entry 1G6J, conformer 25) in order to create a Van der Waals surface (VDWS) in Cartesian points. This surface was used to map the amide hydration dynamics across the surface of ubiquitin: if a point on the rendered

surface was within 4 Å of one or more amide probes, it would adopt the average $\sigma_{NOE}/\sigma_{ROE}$ ratio and would be colored accordingly (see main text for color scale). If a surface point was not within 4 Å of an amide residue, it is colored gray. All molecular images were created using PyMol (Delano Scientific).

Appendix C: Data Tables

Chapter 2

Table C- 1: List of Chemical Shift Perturbations of SNase Δ+PHS/I92E and SNase Δ+PHS/V66E in CTAB/hexanol reverse micelles relative to the SNase Δ+PHS WT protein

Assignment		I92E	V66E
ALA	1		
THR	2		
SER	3	0.033	0.024
THR	4	0.036	0.024
LYS	5	0.038	
LYS	6	0.034	0.025
LEU	7	0.030	0.020
HIS	8	0.063	0.027
LYS	9	0.188	0.047
GLU	10	0.133	0.041
ALA	12		
THR	13	0.208	0.044
LEU	14	0.164	0.068
ILE	15	0.137	0.141
LYS	16	0.232	0.116
ALA	17	0.204	0.150
ILE	18	0.089	0.274
ASP	19	0.217	
GLY	20	0.322	0.038
ASP	21		0.087
THR	22	0.645	0.912
VAL	23	0.881	
LYS	24	0.452	0.972
LEU	25	0.103	0.027
MET	26	0.094	0.050
TYR	27	0.013	0.008
LYS	28	0.042	0.014
GLY	29	0.010	0.010
GLN	30	0.066	0.033
MET	32		0.073
THR	33	0.215	0.080
PHE	34		0.095
ARG	35	0.053	0.095
LEU	36		
LEU	37	0.156	0.039
LEU	38	0.110	0.063
VAL	39	0.027	0.064
ASP	40	0.254	0.145
THR	41		
GLU	43	0.091	0.004
PHE	51	0.012	0.043
ASN	52	0.059	0.022
GLU	53	0.016	0.006
LYS	54	0.018	0.011
TYR	55	0.024	0.022
GLY	56	0.019	0.023
GLU	57	0.034	0.015
ALA	58	0.034	0.023
SER	59	0.151	0.148
ALA	60	0.073	0.032
PHE	61	0.413	0.202
THR	62		2.692
LYS	63		0.725
LYS	64		0.253
MET	65	0.174	0.227
VAL	66	0.599	4.027
GLU	67	0.173	1.857
ASN	68	0.165	0.115
ALA	69	0.164	0.066
LYS	70	0.069	0.072
LYS	71	0.033	0.016
ILE	72	0.043	0.012
GLU	73	0.042	0.031

VAL	74	1.072	0.035
GLU	75	0.694	0.027
PHE	76	0.089	0.053
ASP	77	0.146	0.033
LYS	78	0.043	0.077
GLY	79	0.030	0.005
GLN	80	0.062	
ARG	81	0.026	0.008
THR	82	0.105	0.072
ASP	83	0.043	0.012
LYS	84	0.019	0.011
TYR	85	0.032	0.015
GLY	86	0.054	0.052
ARG	87	0.038	0.016
GLY	88	0.083	0.094
LEU	89	0.111	0.145
ALA	90		0.005
TYR	91	0.148	
GLU	92	0.452	
TYR	93	0.413	0.020
ALA	94	0.026	0.037
ASP	95	0.018	0.003
GLY	96	0.040	0.028
LYS	97	0.044	0.027
MET	98	0.072	0.005
VAL	99	0.206	0.075
ASN	100	0.140	0.016
GLU	101	0.027	0.038
ALA	102	0.075	0.112
LEU	103	0.021	0.134
VAL	104	0.049	0.046
ARG	105	0.072	0.019
GLN	106	0.010	0.011
GLY	107		
LEU	108	0.040	0.020
ALA	109	0.063	0.043
LYS	110		0.084
VAL	111	0.122	0.102
ALA	112	0.141	
TYR	113	0.029	0.032
VAL	114	0.024	0.071
TYR	115		
LYS	116	0.120	0.029
GLY	117	0.108	0.113
ASN	118	0.104	0.107
ASN	119	0.043	0.026
THR	120	0.009	0.018
HIS	121		
GLU	122	0.037	0.050
GLN	123	0.020	0.025
LEU	124	0.039	0.000
LEU	125	0.038	0.018
ARG	126	0.029	0.005
LYS	127	0.007	0.059
ALA	128	0.018	0.044
GLU	129		
ALA	130		
GLN	131	0.024	0.048
ALA	132	0.017	
LYS	133	0.018	0.023
LYS	134	0.024	0.033
GLU	135	0.016	0.017
LYS	136	0.038	0.026
LEU	137	0.019	0.030
ASN	138	0.020	0.015
ILE	139	0.022	0.024
TRP	140	0.028	0.014
SER	141	0.009	0.050
GLU	142	0.086	0.041
ASP	143	0.031	0.020
ASN	144	0.031	0.020
ALA	145	0.019	
ASP	146	0.029	0.018
SER	147	0.025	0.018
GLY	148	0.016	0.017
GLN	149	0.020	0.019

Table C- 2: ^{15}N-Detected NOE and ROE values to water for SNase Δ+PHS

Assignment	NOE S/N	ROE S/N	NOE/ROE
Ser3HN	1102	917	1.20
Thr4HN	715	530	1.35
Lys5HN	290	162	1.79
Lys6HN	78	16	4.76
Leu7HN	13	-23	-0.58
His8HN	89	-65	-1.36
Glu10HN	224	-268	-0.84
Thr13HN	23	-39	-0.60
Leu14HN		-29	
Ala17HN	8	-25	-0.33
Ile18HN	8	-17	-0.48
Asp19HN	10	-11	-0.94
Gly20HN	37	-54	-0.69
Asp21HN	33	-23	-1.42
Thr22HN	63	-75	-0.85
Met26HN		-7	
Lys28HN		-17	
Thr33HN	80	-120	-0.67
Leu38HN	25	-26	-0.95
Glu43HN		-15	
Phe44HN		-15	
Lys53HN		-11	
Glu57HN		-9	
Phe61HN		-7	
Val66HN	9		
Ala69HN		-17	
Lys70HN		-11	
Ile72HN		-32	
Glu73HN	17	-34	-0.49
Phe76HN	70	-100	-0.71
Lys78HN	33	-24	-1.39
Gly79HN	20	-20	-1.02
Arg81HN	36	7	4.92
Thr82HN	32	-47	-0.69
Asp83HN	10	-14	-0.71
Lys84HN	124	52	2.37
Tyr85HN		-9	
Leu89HN	11	-13	-0.91
Tyr91HN		-18	
Asp95HN	51	-58	-0.88
Gly96HN	94	-120	-0.79
Gly107HN	52	-63	-0.83
Leu108HN	13		
Val111HN		-9	
Val114HN	43	-56	-0.78
Gly117HN	28	-9	-3.05
Asn119HN	29	-6	-4.53
Thr120HN	63	-51	-1.23
His121HN	61	-59	-1.03
Leu124HN		-14	
Asn138HN	7	-32	-0.23
Ser139HN	117	-139	-0.84
Glu142HN	32	-28	-1.12
Asp143HN	82		
Asn144HN	129	60	2.14
Asp146HN	87	51	1.70
Ser147HN	296	176	1.68
Gly148HN	198	129	1.54
Gln149HN		-34	

Table C- 3: ^{13}C-Detected NOE and ROE values to water for SNase Δ+PHS

Assignment	NOE S/N	ROE S/N	NOE/ROE
Leu7HDR	40	-41	-0.97
Leu7HDS	18	-19	-0.96
Ile18HD1	24	-38	-0.63
Leu37HDR	21	-22	-0.94
Leu37HDS	23	-29	-0.81
Leu38HDS	21	-32	-0.66
Ile72HD1		-15	
Val74HGS		-8	
Leu89HDS		-11	
Val104HGR	36	-38	-0.93
Val104HGS	6	-7	-0.88
Val114HGS	12	-10	-1.19
Leu124HDS	8	-17	-0.48
Ile139H	36	-26	-1.34

Table C- 4: ^{15}N-Detected NOE and ROE values to water for SNase Δ+PHS/I92E

Assignment	NOE S/N	ROE S/N	NOE/ROE
Ser3HN	850	795	1.07
Thr4HN	640	536	1.19
Lys5HN	319	213	1.50
Lys6HN	77	30	2.60
Leu7HN	19	-15	-1.25
His8HN	106	-74	-1.43
Lys9HN	50		
Glu10HN	12	-12	-0.96
Ala12HN		-22	
Thr13HN		-13	
Leu14HN		-45	
Ala17HN	13	-39	-0.33
Ile18HN	55	-67	-0.82
Asp19HN	65	-64	-1.01
Gly20HN	51	-74	-0.69
Thr22HN	112	-128	-0.87
Val23HN	29	-31	-0.94
Met26HN	11	-11	-1.00
Lys28HN		-19	
Thr33HN	89	-132	-0.67
Arg35HN	7	-11	-0.66
Leu36HN	36	-25	-1.43
Leu38HN	29	-48	-0.60
Glu43HN		-22	
Phe44HN		-17	
Asn51HN	12		
Lys53HN		-11	
Tyr54HN		-19	

Ser59HN	15	-19	-0.79
Ala60HN		-10	
Val66HN	20	-56	-0.36
Ala69HN		-18	
Lys71HN		-7	
Ile72HN		-44	
Glu73HN	37	-47	-0.78
Phe76HN	89	-145	-0.62
Asp77HN	294	-369	-0.80
Lys78HN	35	-37	-0.93
Gly79HN	25	-22	-1.13
Arg81HN	33	11	2.99
Thr82HN	31	-47	-0.67
Asp83HN	20	-11	-1.75
Lys84HN	100	54	1.87
Leu89HN	20	-24	-0.84
Ala94HN		-10	
Asp95HN	60	-82	-0.73
Gly96HN	106	-142	-0.74
Met98HN	18		
Arg105HN		-9	
Gly107HN	90	-92	-0.98

Lys110HN		-10	
Val111HN		-24	
Val114HN	69	-69	-1.01
Lys116HN	41		
Asn118HN	22		
Asn119HN	32	-21	-1.54
Thr120HN	79	-64	-1.24
Glu122HN	29	-50	-0.58
Gln123HN	24		
Ala128HN		-13	
Asn138HN	17	-43	-0.39
Ile139HN	18		
Ser141HN	154	-193	-0.80
Glu142HN	43	-26	-1.68
Asp143HN	133	23	5.79
Asn144HN	206	122	1.69
Ala145HN	273	200	1.36
Asp146HN	152	115	1.33
Ser147HN	407	304	1.34
Gly148HN	298	239	1.25
Gln143HN		-52	

Table C- 5: ^{13}C-Detected NOE and ROE values to water for SNase Δ+PHS/I92E

Assignment	NOE S/N	ROE S/N	NOE/ROE
Leu7HDR	34	-37	-0.92
Leu7HDS	27	-27	-1.00
Ile18HDR	31	-45	-0.69
Val23HGS	19	-31	-0.59
Leu36HDR	37	-33	-1.12
Leu36HDS	41	-38	-1.07
Leu37HDR	33	-29	-1.15
Leu37HDS	32	-37	-0.89

Leu38HDR		-7	
Leu38HDS	38	-39	-0.98
Val66HGR	38	-29	-1.31
Val66HGS	24	-22	-1.09
Ile72HDR	15	-24	-0.61
Val74HGS	8		
Val104HGR	60	-52	-1.15
Val104HGS	16		
Val111HGS	14		
Ile139HDR	55	-42	-1.30

Table C- 6: ^{15}N-Detected NOE and ROE values to water for SNase Δ+PHS/V66E

Assignment	NOE S/N	ROE S/N	NOE/ROE
Ser3HN	1356	1002	1.35
Thr4HN	761	475	1.60
Leu7HN	7	-39	-0.18
His8HN	140	-164	-0.85
Lys9HN	47	-33	-1.41
Thr13HN	68	-96	-0.71
Leu14HN	18	-81	-0.22
Ala17HN	24	-67	-0.37
Ile18HN	294	-332	-0.89
Gly20HN	95	-106	-0.90
Asp21HN	118	-57	-2.06
Thr22HN	232	-251	-0.92
Leu25HN	8	-12	-0.74
Lys28HN		-40	
Gly29HN		-9	
Met32HN	9	-25	-0.35
Leu38HN	85	-120	-0.71
Val39HN	16	-13	-1.30
Glu43HN		-29	
Phe44HN		-26	
Lys53HN		-16	
Ser59HN	40	-66	-0.62
Lys63HN	21	-38	-0.55
Lys64HN		-8	
Ala69HN	11	-27	-0.40
Lys70HN		-12	
Ile72HN	14	-71	-0.19
Glu73HN	54	-68	-0.79
Phe76HN	154	-199	-0.78
Asp77HN	489	-548	-0.89
Lys78HN	69	-57	-1.20
Gly79HN	30	-28	-1.08
Thr82HN	77	-107	-0.72
Asp83HN	34	-18	-1.92
Tyr85HN	225	-222	-1.02
Leu89HN	39	-52	-0.76
Ala90HN	8	-15	-0.53
Asp95HN	99	-118	-0.83
Gly96HN	184	-222	-0.83
Lys97HN	12	-15	-0.77
Met98HN	14	-27	-0.52
Gly107HN	142	-157	-0.91
Ala109HN	127	-135	-0.94
Lys110HN	15	-32	-0.47
Ala112HN	9	-13	-0.66
Val114HN	101	-112	-0.90
Lys116HN	66	-10	-6.52
Gly117HN	63	-35	-1.79
Asn118HN	33	-32	-1.02
Asn119HN	69	-32	-2.14
Thr120HN	175	-134	-1.31
Glu122HN	8	-11	-0.73
Lys133HN	97	-131	-0.74
Lys134HN		-8	
Asn138HN	25	-61	-0.41
Ser141HN	274	-315	-0.87
Glu142HN	47	-49	-0.96
Asp143HN	119	-30	-3.98
Asn144HN	146	29	5.02
Asp146HN	85	20	4.34
Ser147HN	321	111	2.89
Gly148HN	182	89	2.04
Gln149HN	-8	-76	0.10

Table C- 7: ^{13}C-Detected NOE and ROE values to water for SNase Δ+PHS/V66E

Assignment	NOE S/N	ROE S/N	NOE/ROE
Leu7HDR	51	-58	-0.88
Leu7HDS	24	-29	-0.85
Leu14HDR	22	-18	-1.22
I18HD1	51	-74	-0.69
Leu36HDR	11	-22	-0.48
Leu36HDS	23	-21	-1.11
Leu37HDR	26	-30	-0.88
Leu37HDS	31	-35	-0.90
Leu38HDR	10	-10	-0.97
Leu38HDS	38	-49	-0.76
Ile72HD1	15	-28	-0.54
Leu89HDS	9	-15	-0.58
Ile92HD1	-1	-13	0.09
Val104HDR	56	-52	-1.08
Val104HGS	5	-11	-0.42
Val114HGS	10	-11	-0.87
Leu124HDR	2	-33	-0.06
Leu124HDS	9	-21	-0.41
Ile139HD1	42	-43	-0.99

Table C- 8: List of H-N NOE values for SNase Δ+PHS and mutants SNase Δ+PHS/I92E and SNase Δ+PHS/V66E

Assignment		WT			I92E			V66E		
ALA	1									
THR	2									
SER	3	-1.03	±	0.01	-0.87	±	0.02	-1.01	±	0.01
THR	4	-0.42	±	0.01	-0.21	±	0.01	-0.32	±	0.01
LYS	5				0.05	±	0.01			
LYS	6	0.12	±	0.01	0.17	±	0.01	0.11	±	0.01
LEU	7	0.55	±	0.01	0.45	±	0.01	0.45	±	0.01
HIS	8	0.66	±	0.01	0.66	±	0.01	0.59	±	0.01
LYS	9				0.73	±	0.02	0.67	±	0.01
GLU	10				0.76	±	0.02	0.77	±	0.01
ALA	12				0.73	±	0.01			

THR	13	0.77	±	0.02	0.75	±	0.02	0.76	±	0.01
LEU	14	0.77	±	0.02	0.83	±	0.01	0.79	±	0.01
ILE	15	0.79	±	0.03	0.77	±	0.02	0.78	±	0.02
LYS	16	0.74	±	0.03	0.75	±	0.02	0.82	±	0.02
ALA	17	0.79	±	0.02	0.69	±	0.02	0.71	±	0.01
ILE	18	0.63	±	0.02	0.59	±	0.02	0.59	±	0.02
ASP	19	0.71	±	0.04	0.65	±	0.02			
GLY	20	0.76	±	0.02	0.73	±	0.02	0.72	±	0.02
ASP	21	0.81	±	0.06				0.68	±	0.02
THR	22	0.86	±	0.04	0.8	±	0.04	0.81	±	0.03
VAL	23	0.8	±	0.04	0.78	±	0.02			
LYS	24	0.79	±	0.02	0.73	±	0.02	0.78	±	0.02
LEU	25				0.75	±	0.01	0.77	±	0.01
MET	26	0.83	±	0.02	0.77	±	0.02	0.79	±	0.01
TYR	27	0.82	±	0.02	0.8	±	0.01	0.86	±	0.01
LYS	28	0.71	±	0.02	0.67	±	0.01	0.69	±	0.01
GLY	29	0.7	±	0.02	0.66	±	0.02	0.72	±	0.01
GLN	30	0.76	±	0.02				0.76	±	0.01
MET	32	0.72	±	0.02				0.79	±	0.01
THR	33	0.72	±	0.02						
PHE	34	0.79	±	0.02				0.75	±	0.01
ARG	35	0.85	±	0.04	0.84	±	0.02	0.8	±	0.01
LEU	36				0.72	±	0.02	0.76	±	0.01
LEU	37	0.73	±	0.04	0.79	±	0.02	0.86	±	0.02
LEU	38	0.77	±	0.05	0.77	±	0.05	0.77	±	0.02
VAL	39	0.83	±	0.04	0.79	±	0.02	0.74	±	0.01
ASP	40	0.75	±	0.04						
THR	41	0.77	±	0.03						
GLU	43	0.71	±	0.02	0.74	±	0.02	0.72	±	0.01
PHE	51	0.67	±	0.02	0.66	±	0.02	0.7	±	0.01
ASN	52	0.72	±	0.04	0.73	±	0.03	0.72	±	0.02
GLU	53	0.72	±	0.02	0.7	±	0.01	0.73	±	0.01
LYS	54	0.65	±	0.02	0.6	±	0.01	0.65	±	0.01
TYR	55	0.75	±	0.02	0.75	±	0.02	0.75	±	0.02
GLY	56	0.83	±	0.02	0.81	±	0.02	0.85	±	0.02
GLU	57	0.82	±	0.02	0.81	±	0.02	0.82	±	0.02
ALA	58	0.85	±	0.03	0.79	±	0.02	0.84	±	0.02
SER	59				0.69	±	0.04	0.81	±	0.02
ALA	60	0.77	±	0.03	0.72	±	0.02	0.79	±	0.02

PHE	61	0.84	±	0.03	0.73	±	0.02	0.82	±	0.02
THR	62	0.78	±	0.03				0.8	±	0.02
LYS	63	0.79	±	0.03				0.87	±	0.02
LYS	64							0.79	±	0.02
MET	65	0.78	±	0.02	0.79	±	0.02	0.82	±	0.02
VAL	66	0.81	±	0.04	0.76	±	0.01	0.83	±	0.02
GLU	67	0.79	±	0.03	0.8	±	0.02	0.8	±	0.02
ASN	68	0.81	±	0.03	0.69	±	0.02	0.8	±	0.02
ALA	69	0.78	±	0.02	0.74	±	0.01	0.78	±	0.01
LYS	70	0.77	±	0.02	0.74	±	0.02	0.8	±	0.02
LYS	71	0.72	±	0.02	0.75	±	0.02	0.76	±	0.02
ILE	72	0.73	±	0.02	0.74	±	0.01	0.71	±	0.01
GLU	73	0.83	±	0.03	0.8	±	0.02	0.82	±	0.01
VAL	74	0.84	±	0.03	0.81	±	0.02	0.85	±	0.02
GLU	75	0.8	±	0.02	0.82	±	0.02	0.81	±	0.02
PHE	76	0.74	±	0.02	0.73	±	0.01	0.77	±	0.01
ASP	77				0.77	±	0.02	0.81	±	0.02
LYS	78	0.75	±	0.03	0.74	±	0.02	0.79	±	0.02
GLY	79				0.72	±	0.01	0.73	±	0.01
GLN	80	0.1	±	0.03	0.18	±	0.02			
ARG	81	0.76	±	0.02	0.84	±	0.03	0.74	±	0.01
THR	82	0.71	±	0.02	0.73	±	0.02	0.76	±	0.02
ASP	83	0.78	±	0.02	0.75	±	0.01	0.76	±	0.01
LYS	84	0.65	±	0.02				0.66	±	0.01
TYR	85	0.72	±	0.03	0.79	±	0.02	0.73	±	0.01
GLY	86	0.79	±	0.03	0.7	±	0.02	0.76	±	0.02
ARG	87	0.77	±	0.03	0.72	±	0.02	0.75	±	0.02
GLY	88	0.8	±	0.02	0.78	±	0.01	0.78	±	0.01
LEU	89	0.77	±	0.03	0.76	±	0.02	0.83	±	0.01
ALA	90	0.88	±	0.05				0.84	±	0.02
TYR	91	0.75	±	0.02						
GLU	92	0.79	±	0.03	0.71	±	0.01			
TYR	93	0.84	±	0.03	0.8	±	0.02	0.82	±	0.02
ALA	94	0.84	±	0.03	0.79	±	0.02	0.83	±	0.02
ASP	95	0.78	±	0.02	0.79	±	0.02	0.79	±	0.02
GLY	96	0.77	±	0.02	0.77	±	0.02	0.83	±	0.02
LYS	97	0.83	±	0.02	0.85	±	0.01	0.83	±	0.01
MET	98				0.67	±	0.01	0.72	±	0.01
VAL	99	0.72	±	0.03	0.85	±	0.02	0.78	±	0.02

ASN	100	0.84	±	0.04	0.82	±	0.02	0.84	±	0.02
GLU	101	0.76	±	0.03	0.79	±	0.02	0.84	±	0.02
ALA	102	0.82	±	0.03	0.85	±	0.02	0.86	±	0.02
LEU	103									
VAL	104	0.8	±	0.02	0.8	±	0.02			
ARG	105									
GLN	106	0.75	±	0.03	0.8	±	0.02	0.73	±	0.02
GLY	107									
LEU	108	0.85	±	0.04	0.82	±	0.02	0.86	±	0.02
ALA	109	0.83	±	0.03	0.77	±	0.02	0.81	±	0.02
LYS	110									
VAL	111	0.83	±	0.04	0.8	±	0.02	0.8	±	0.02
ALA	112	0.78	±	0.04	0.86	±	0.03	0.85	±	0.03
TYR	113	0.73	±	0.07	0.78	±	0.05	0.81	±	0.01
VAL	114	0.77	±	0.02	0.77	±	0.02			
TYR	115									
LYS	116	0.68	±	0.03	-0.65	±	0	0.63	±	0.02
GLY	117	0.62	±	0.01	0.65	±	0.02	0.64	±	0.01
ASN	118	0.57	±	0.07	0.6	±	0.09	0.63	±	0.03
ASN	119							0.73	±	0.02
THR	120	0.72	±	0.02	0.69	±	0.02	0.69	±	0.02
HIS	121	0.79	±	0.05	0.82	±	0.04	0.79	±	0.03
GLU	122	0.79	±	0.02	0.81	±	0.01	0.84	±	0.02
GLN	123				0.73	±	0.02	0.74	±	0.02
LEU	124	0.83	±	0.03	0.84	±	0.01	0.81	±	0.02
LEU	125	0.81	±	0.03				0.8	±	0.02
ARG	126	0.78	±	0.03	0.81	±	0.02	0.81	±	0.02
LYS	127	0.69	±	0.02	0.74	±	0.02			
ALA	128	0.8	±	0.02	0.77	±	0.02	0.8	±	0.02
GLU	129				0.28	±	0.09	0.81	±	0.02
ALA	130				0.8	±	0.02			
GLN	131	0.82	±	0.02	0.87	±	0.02	0.88	±	0.02
ALA	132	0.76	±	0.03	0.79	±	0.02			
LYS	133	0.79	±	0.02				0.8	±	0.01
LYS	134	0.83	±	0.02	0.84	±	0.02	0.84	±	0.02
GLU	135	0.85	±	0.02	0.81	±	0.02	0.84	±	0.02
LYS	136	0.76	±	0.02	0.8	±	0.01	0.81	±	0.02
LEU	137	0.86	±	0.02	0.83	±	0.02	0.83	±	0.02
ASN	138	0.83	±	0.02	0.8	±	0.01	0.8	±	0.01

ILE	139	0.76	±	0.03	0.79	±	0.02	0.82	±	0.02
TRP	140							0.81	±	0.02
SER	141	0.79	±	0.03	0.81	±	0.02	0.83	±	0.02
GLU	142				0.57	±	0.01	0.57	±	0.01
ASP	143	0.36	±	0.01	0.43	±	0.01	0.35	±	0.01
ASN	144	0.18	±	0.01	0.15	±	0.01	0.18	±	0.01
ALA	145				0.08	±	0			
ASP	146	0.06	±	0.01	0.04	±	0	0.06	±	0
SER	147	-0.38	±	0.01	-0.42	±	0	-0.39	±	0
GLY	148	-0.62	±	0.01	-0.71	±	0.01	-0.68	±	0
GLN	149	-0.69	±	0.01	-0.65	±	0	-0.71	±	0

Table C- 9: List of TROSY Hahn-Echo (R_{ex}) values for SNase Δ+PHS and mutants SNase Δ+PHS/I92E and SNase Δ+PHS/V66E

Assignment		WT	I92E	V66E
SER	3	2.26 ± 0.38	2.45 ± 0.39	-6.91 ± 0.19
THR	4	2.12 ± 0.29	2.04 ± 0.25	-6.50 ± 0.19
LYS	5		1.60 ± 0.21	
LYS	6	1.64 ± 0.31	1.90 ± 0.30	-3.70 ± 0.19
LEU	7	2.83 ± 0.31	2.09 ± 0.25	0.03 ± 0.24
HIS	8	3.40 ± 0.42	3.75 ± 0.25	-1.53 ± 0.31
LYS	9	6.87 ± 0.46	2.18 ± 0.34	-0.12 ± 0.30
GLU	10	2.92 ± 0.68	3.06 ± 0.36	0.46 ± 0.56
THR	13	3.16 ± 0.62	4.15 ± 0.69	-0.37 ± 0.52
LEU	14	1.98 ± 0.41	1.50 ± 0.25	-0.23 ± 0.32
ILE	15	0.48 ± 0.98	2.50 ± 0.58	-1.77 ± 0.81
LYS	16	2.93 ± 0.94	4.20 ± 0.57	1.82 ± 0.78
ALA	17	1.11 ± 0.46	1.86 ± 0.35	-0.50 ± 0.35
ILE	18	2.02 ± 0.88	2.96 ± 0.61	-5.26 ± 0.63
ASP	19	2.91 ± 2.05	9.01 ± 0.65	
GLY	20	6.11 ± 0.81	9.34 ± 0.38	3.19 ± 0.63
ASP	21	35.35 ± 5.95		2.47 ± 0.95
THR	22	6.05 ± 1.47	16.18 ± 1.65	0.30 ± 1.18
VAL	23	10.31 ± 1.42	4.33 ± 0.42	
LYS	24	0.02 ± 0.67	1.78 ± 0.57	-1.98 ± 0.51
LEU	25		1.29 ± 0.37	-0.47 ± 0.60
MET	26	2.35 ± 0.74	2.27 ± 0.39	-0.62 ± 0.56
TYR	27	1.17 ± 0.82	0.43 ± 0.34	-2.10 ± 0.65
LYS	28	0.88 ± 0.53	1.09 ± 0.29	-1.23 ± 0.37
GLY	29	2.81 ± 0.60	4.13 ± 0.35	-1.06 ± 0.48
GLN	30	-0.12 ± 0.68		-1.95 ± 0.49
MET	32	0.68 ± 0.79		0.27 ± 0.59
THR	33	3.68 ± 0.56		
PHE	34	2.01 ± 0.98		0.34 ± 0.57
ARG	35	23.54 ± 2.22	9.06 ± 0.53	0.46 ± 0.61
LEU	36		3.94 ± 0.42	2.07 ± 0.53
Assignment		WT	I92E	V66E
LEU	37	5.26 ± 1.62	5.59 ± 0.74	-1.72 ± 0.92

LEU	38	5.68 ± 1.90	13.09 ± 1.51	3.12 ± 0.59
VAL	39	3.14 ± 1.25	9.32 ± 0.71	0.33 ± 0.50
ASP	40	36.38 ± 3.76		
THR	41	0.55 ± 1.15		
GLU	43	4.09 ± 0.85	8.81 ± 0.43	0.59 ± 0.42
PHE	51	6.30 ± 0.69	8.72 ± 0.41	2.79 ± 0.50
ASN	52	8.85 ± 1.97	7.91 ± 0.92	5.59 ± 0.83
GLU	53	1.21 ± 0.69	3.22 ± 0.33	2.38 ± 0.62
LYS	54	4.48 ± 0.51	4.86 ± 0.27	3.87 ± 0.41
TYR	55	3.51 ± 0.66	5.87 ± 0.45	3.34 ± 0.57
GLY	56	3.68 ± 0.76	3.67 ± 0.42	1.05 ± 0.74
GLU	57	5.06 ± 1.05	6.15 ± 0.55	3.70 ± 0.98
ALA	58	0.50 ± 1.20	4.38 ± 0.57	4.36 ± 1.04
SER	59	4.10 ± 2.95	5.55 ± 1.34	0.17 ± 0.85
ALA	60	2.93 ± 1.17	2.63 ± 0.59	3.32 ± 0.99
PHE	61	0.94 ± 1.26	1.73 ± 0.51	1.96 ± 0.98
THR	62	2.34 ± 1.28		5.37 1.30
LYS	63	0.61 ± 1.22		-0.34 0.84
LYS	64			0.97 0.78
MET	65	2.45 ± 0.90	2.18 ± 0.45	-2.02 ± 0.79
VAL	66	2.16 ± 1.43	4.14 ± 0.32	0.39 ± 0.83
GLU	67	0.46 ± 1.00	3.41 ± 0.46	2.46 ± 0.84
ASN	68	2.24 ± 0.96	3.87 ± 0.51	1.22 ± 0.90
ALA	69	-1.37 ± 0.63	0.37 ± 0.32	-3.21 ± 0.58
LYS	70	2.04 ± 0.99	2.67 ± 0.42	-0.56 ± 0.71
LYS	71	1.86 ± 1.10	3.45 ± 0.47	-0.70 ± 0.78
ILE	72	0.60 ± 0.45	0.85 ± 0.25	-0.14 ± 0.34
GLU	73	1.69 ± 0.99	2.13 ± 0.40	0.31 ± 0.65
VAL	74	3.43 ± 0.90	4.05 ± 0.44	2.26 ± 0.60
GLU	75	1.43 ± 1.00	2.49 ± 0.41	0.15 ± 0.61
PHE	76	2.53 ± 0.63	3.53 ± 0.33	0.48 ± 0.43
ASP	77	1.92 ± 0.69	3.78 ± 0.52	-0.26 ± 0.55
LYS	78	4.67 ± 0.87	4.22 ± 0.43	2.61 ± 0.66
GLY	79	2.71 ± 0.67	2.66 ± 0.34	0.51 ± 0.50
GLN	80	2.33 ± 1.21	3.23 ± 0.70	
Assignment		WT	I92E	V66E
ARG	81	1.93 ± 0.65	4.46 ± 0.50	-0.02 ± 0.45
THR	82	5.18 ± 0.78	3.85 ± 0.41	-2.23 ± 0.55
ASP	83	0.85 ± 0.76	2.19 ± 0.34	-1.02 ± 0.54

LYS	84	3.51 ± 0.71		0.96 ± 0.46
TYR	85	1.76 ± 1.41	4.02 ± 0.57	-2.01 ± 0.45
GLY	86	2.90 ± 1.33	5.16 ± 0.59	1.04 ± 1.11
ARG	87	1.49 ± 0.99	3.13 ± 0.41	-1.55 ± 0.71
GLY	88	2.20 ± 0.80	1.45 ± 0.30	-1.94 ± 0.59
LEU	89	10.90 ± 1.76	5.95 ± 0.54	-0.17 ± 0.58
ALA	90	0.36 ± 1.82		-0.44 ± 0.62
TYR	91	3.39 ± 0.63	3.30 ± 0.43	
GLU	92	1.61 ± 1.01	2.11 ± 0.43	
TYR	93	3.53 ± 1.05	4.01 ± 0.44	0.75 ± 0.71
ALA	94	2.48 ± 0.94	1.78 ± 0.36	-0.86 ± 0.62
ASP	95	1.18 ± 0.73	1.53 ± 0.31	-1.13 ± 0.57
GLY	96	2.97 ± 0.80	5.32 ± 0.37	0.79 ± 0.64
LYS	97	0.34 ± 0.72	0.29 ± 0.34	-2.39 ± 0.61
MET	98		1.09 ± 0.23	-0.14 ± 0.30
VAL	99	-1.05 ± 1.37	-0.63 ± 0.60	-1.78 ± 0.81
ASN	100	5.56 ± 1.31	5.30 ± 0.62	5.05 ± 0.88
GLU	101	1.00 ± 1.39	3.06 ± 0.72	-0.88 ± 0.92
ALA	102	-0.97 ± 1.21	1.33 ± 0.56	0.21 ± 0.79
LEU	103	2.54 ± 1.03	5.57 ± 0.58	
VAL	104	1.46 ± 1.42	4.38 ± 0.66	1.98 ± 0.89
ARG	105	3.34 ± 1.13	3.45 ± 0.58	1.66 ± 0.81
GLN	106	2.84 ± 1.04	3.51 ± 0.45	0.51 ± 0.72
GLY				
LEU	108	1.12 ± 1.24	3.59 ± 0.52	-0.92 ± 0.89
ALA	109	2.77 ± 1.84	4.50 ± 0.76	1.42 ± 1.08
LYS	110	0.84 ± 1.25		-1.33 ± 0.85
VAL	111	4.21 ± 3.94	1.79 ± 1.81	0.01 ± 0.50
ALA	112		4.69 ± 0.45	
TYR	113	-0.19 ± 0.64	1.03 ± 0.46	
VAL	114	4.34 ± 1.03	7.88 ± 0.60	1.65 ± 0.56
TYR	115	47.62 ± 30.85		
LYS	116	4.31 ± 0.37	9.71 ± 0.60	2.58 ± 0.35
Assignment		WT	I92E	V66E
GLY	117	39.30 ± 5.57	61.06 ± 8.52	17.21 ± 1.30
ASN	118	0.79 ± 0.56		-0.79 ± 0.72
ASN	119	5.25 ± 0.96	10.04 ± 0.54	1.18 ± 0.70
THR	120	5.31 ± 1.92	8.19 ± 1.88	2.15 ± 1.37
HIS	121	7.04 ± 1.46		

GLU	122	-0.31 ± 0.68	0.86 ± 0.26	-1.41 ± 0.51
GLN	123	2.33 ± 0.57	3.50 ± 0.42	1.73 ± 0.50
LEU	124	1.62 ± 0.84	3.53 ± 0.37	1.39 ± 0.61
LEU	125	0.66 ± 1.25		-0.33 ± 1.00
ARG	126	2.59 ± 1.17	3.77 ± 0.56	0.29 ± 0.76
LYS	127	0.08 ± 0.82	1.76 ± 0.45	
ALA	128	0.47 ± 0.91	1.65 ± 0.48	-1.06 ± 0.76
GLU	129		2.84 ± 0.42	2.98 ± 0.74
ALA	130		1.57 ± 0.46	
GLN	131	1.21 ± 0.93	2.29 ± 0.45	-0.28 ± 0.82
ALA	132	0.29 ± 1.35	0.90 ± 0.49	
LYS	133	2.28 ± 1.36		1.10 ± 0.65
LYS	134	-0.37 ± 1.06	1.61 ± 0.51	-1.55 ± 0.95
GLU	135	3.39 ± 1.09	4.08 ± 0.51	2.83 ± 0.95
LYS	136	0.60 ± 1.21	1.22 ± 0.36	-1.40 ± 0.88
LEU	137	1.63 ± 0.93	2.46 ± 0.40	-0.04 ± 0.72
ASN	138	2.84 ± 0.50	3.37 ± 0.30	0.00 ± 0.42
ILE	139	6.78 ± 1.31	11.71 ± 0.57	6.82 ± 0.94
TRP	140	2.16 ± 1.03		0.77 ± 0.86
SER	141	1.14 ± 0.97	3.27 ± 0.62	0.99 ± 0.62
GLU	142	0.79 ± 0.56	1.28 ± 0.28	-2.20 ± 0.46
ASP	143	2.59 ± 0.32	2.45 ± 0.14	-1.21 ± 0.23
ASN	144	1.94 ± 0.31	1.79 ± 0.18	-3.92 ± 0.24
ALA	145		0.71 ± 0.13	
ASP	146	1.91 ± 0.19	1.32 ± 0.11	-4.97 ± 0.14
SER	147	1.83 ± 0.19	1.13 ± 0.10	-5.32 ± 0.14
GLY	148	1.85 ± 0.18	1.43 ± 0.10	-6.10 ± 0.11
GLN	149	0.95 ± 0.15	0.44 ± 0.10	-6.59 ± 0.12

Chapter 3

Table C- 10: Ln transform fits of Ubiquitin in AOT reverse micelles using either a 4 point (20, 40, 60, 80) buildup series or a 3 point (40, 60, 80) buildup series

		4 Mix Times				3 Mix Times			
Assignment		intercept	slope	NOE/ ROE	R^2	intercept	slope	NOE/ ROE	R^2
Gln	2	-1.43	13.26	0.24	0.96	-1.86	16.4	0.16	1
Ile	3	-0.29	4.58	0.75	0.17	0.27	-7.61	1.3	0.83
Phe	4	-0.56	10.6	0.57	0.56	-0.7	9.27	0.5	0.29
Lys	6	-0.19	3.9	0.83	0.4	-0.11	0.92	0.89	0.02
Thr	7	-0.6	7.12	0.55	0.95	-0.84	8.93	0.43	0.99
Leu	8	-0.69	9.93	0.5	0.96	-1.02	12.35	0.36	1
Thr	9	-0.47	6.52	0.63	0.96	-0.67	7.84	0.51	0.98
Gly	10	-0.75	19.02	0.47	0.98	-1.28	21.83	0.28	0.99
Lys	11	-0.65	6.22	0.52	0.93	-0.86	7.85	0.42	0.96
Thr	12	-0.6	4.68	0.55	0.68	-0.9	8.44	0.41	0.97
Thr	14	-0.79	4.58	0.46	0.81	-0.74	1.9	0.48	0.97
Leu	15	-1.57	16.73	0.21	0.66	-1.37	6.71	0.25	0.19
Val	17	-0.65	4.87	0.52	0.94	-0.76	5.13	0.47	0.87
Glu	18	-1.65	11.59	0.19	0.99	-1.85	11.13	0.16	0.97
Ser	20	-0.8	8.75	0.45	0.9	-0.78	5.25	0.46	0.95
Asp	21	-1.44	25.75	0.24	0.96	-2.28	31.92	0.1	1
Thr	22	-0.82	6.66	0.44	0.96	-1.04	8.37	0.35	1
Ile	23	1.19	-37.23	3.28	0.42	-0.81	14.27	0.44	0.32
Asn	25	-0.54	5.57	0.58	0.9	-0.77	7.79	0.46	1
Val	26	-2.6	15.97	0.07	0.88	-3.13	20.04	0.04	0.86
Glu	34	-1.65	21.2	0.19	0.9	-1.65	13.25	0.19	0.9
Gln	40	-0.45	4.23	0.64	0.07	0.1	-7.59	1.1	0.15
Gln	41	-0.82	8.09	0.44	0.27	-1.02	8.91	0.36	0.15
Arg	42	-0.52	4.55	0.59	0.07	-0.93	10.56	0.39	0.15
Leu	43	-0.66	6.31	0.51	0.89	-0.93	8.88	0.4	0.98
Ala	46	-1.9	22.39	0.15	0.99	-2.5	25.23	0.08	1
Lys	48	0.06	-4.95	1.06	0.16	0.77	-16.43	2.15	0.75
Leu	50	-0.73	6.7	0.48	0.88	-0.86	6.56	0.42	0.73
Glu	51	-0.48	5.84	0.62	0.9	-0.72	8.14	0.49	0.99
Asp	52	-2.3	16.16	0.1	0.91	-2.95	22.34	0.05	1
Ser	57	-0.47	6.01	0.62	0.89	-0.47	3.75	0.62	0.82
Asp	58	-0.47	4.58	0.62	0.91	-0.47	2.83	0.63	0.96

Ile	61	-0.61	1.74	0.54	0.02	-0.97	7.88	0.38	0.17
Gln	62	-1.6	14.77	0.2	0.96	-2.1	18.51	0.12	1
Lys	63	-1.79	1.23	0.17	0.02	-1.34	-7.57	0.26	0.56
Glu	64	-0.96	18.87	0.38	0.36	-0.74	7.67	0.48	0.04
Ser	65	-0.92	10.28	0.4	0.86	-1.36	14.54	0.26	0.94
Thr	66	-0.93	5.57	0.39	0.99	-1.01	4.88	0.36	0.99
Leu	67	-0.66	10.43	0.51	1	-0.85	10.04	0.43	1
His	68	-0.67	9.42	0.51	1	-0.86	9.46	0.42	1
Leu	69	-0.75	10.11	0.47	0.99	-0.98	10.5	0.38	0.99
Val	70	-0.16	6.41	0.86	0.94	-0.29	6.53	0.75	0.87
Leu	71	-0.9	7.84	0.41	0.69	-1.4	14.21	0.25	1
Arg	72	-0.42	0.61	0.65	0	0.29	-12.92	1.33	0.29
Leu	73	-1.15	15.61	0.32	0.98	-1.6	18.11	0.2	1
Arg	74	-1.5	18.87	0.22	0.93	-2.08	22.57	0.13	0.92
Gly	75	-1.94	12.2	0.14	0.9	-2.41	16.37	0.09	0.95

Chapter 4

Table C- 11: Glucose HX rates as a function of pH

pH	CTAB	CTAB w/ 50mM Acetate	AOT
3		326	
4	44.8	325	298
4.5	62		179.9
5	41	275	24
5.5	41	281	96
6	44	285	105
7.5	52	417	

Table C- 12 Glucose HX rates as a function of buffer concentration in CTAB/hexanol reverse micelles

Buffer Concentration (mM)	Sodium Acetate (pH 5)	Sodium Phosphate (pH 5)
0	41	41
10	88	268
20	132	417
30	183	
4	225	
50	275	

Table C- 13: List of Hydroxyls and their assigned resonances

Hydroxyl	Resonance (ppm)
Thr7	5.7
Thr9	5.211
Thr12	5.429
Thr14	n/a
Thr22	n/a
Thr55	4.75
Thr66	6.135
Ser20	5.2
Ser57	4.7
Ser65	6.13
Tyr59	n/a

Table C- 14: List of residues within 4 Å of an Hα

GLN	2
SER	20
ASP	21
ILE	23
GLU	24
ILE	36
ASP	39
GLN	40
GLN	41
ASP	52
GLY	53
ARG	54
ASN	60
ILE	61
LYS	63
GLU	64
ARG	72
ARG	74
GLY	75
GLY	75
GLY	76

Table C- 15: List of amides near hydroxyls

Affected Amide	Nearby OH	Distance
PHE4	SER65	5.55
PHE4	THR66	5.43
VAL5	THR14	5.20
THR7	THR7	2.51
THR7	THR12	5.20
LEU8	THR7	3.76
LEU8	THR9	4.88
THR9	THR7	2.41
THR9	THR9	3.07
GLY10	THR7	2.89
GLY10	THR9	4.66
LYS11	THR7	2.19
LYS11	THR9	4.76
THR12	THR7	5.40
THR12	THR12	3.08
ILE13	THR12	4.35
ILE13	THR14	5.10
THR14	THR14	2.51
LEU15	THR14	4.58
SER20	SER20	3.71
ASP21	SER20	4.75
THR22	THR22	2.42
ILE23	THR22	3.63
GLU24	THR22	3.46
ASN25	THR22	2.45
VAL26	THR22	4.63
LEU50	TYR59	4.94
GLU51	TYR59	2.20
GLY53	THR22	4.52
ARG54	THR22	5.68
ARG54	TYR59	5.31
THR55	THR55	2.05
LEU56	THR55	4.50
SER57	THR55	4.17
SER57	SER57	3.89
ASP58	THR55	2.80
ASP58	SER57	3.91
TYR59	THR55	4.98
TYR59	SER57	5.23
ASN60	SER57	4.89
ILE61	SER57	5.94
GLN62	SER65	2.10
LYS63	SER65	5.25
GLU64	SER65	5.35
SER65	SER65	3.10
THR66	SER65	3.78
THR66	THR66	3.26
LEU67	THR66	4.55

Table C- 16: List of fitted rates for Ubiquitin in AOT reverse micelles using the full buildup equation (Equation 4-1)

Assignment	NOE	NOE R^2	ROE	ROE R^2	G3 6.1 ppm	G3 6.1 ppm R^2	G3 5.4 ppm	G3 5.4 R^2	No Correction	Corrected Ratio
Q2HN	2.12E-03	1.00	6.71E-04	0.84	1.86E-03	1.00	1.55E-03	1.00	-3.17	-0.86
I3HN	1.70E-04	0.99	4.16E-04	0.05	1.64E-04	0.97	2.23E-04	0.88	-0.41	-0.38
F4HN	2.55E-04	0.99	2.62E-04	0.44			2.21E-04	0.88	-0.97	
V5HN	2.28E-04	1.00			1.82E-04	0.99	1.72E-04	0.94		
K6HN	1.57E-04	1.00			1.24E-04	1.00	1.24E-04	0.98		
T7HN	5.59E-04	0.99	6.43E-04	0.96	5.34E-04	0.99	1.67E-04	0.95	-0.87	-0.12
L8HN	1.82E-03	1.00	2.30E-03	0.98	1.77E-03	1.00	1.34E-03	0.98	-0.79	-0.41
T9HN	2.48E-03	1.00	2.46E-03	0.95	2.15E-03	0.99	4.07E-04	0.99	-1.00	-0.06
G10HN	1.50E-03	0.98	1.33E-03	0.98	1.34E-03	0.99	5.36E-04	0.99	-1.12	-0.16
K11HN	3.31E-03	0.99	2.21E-03	0.94	2.89E-03	1.00	6.74E-04	0.93	-1.50	-0.09
T12HN	1.07E-02	0.90	1.23E-03	0.46	9.20E-03	0.92	5.98E-03	0.99	-8.69	-0.56
I13HN	2.93E-04	0.99	4.98E-04	0.77	2.10E-04	1.00	1.66E-04	0.95	-0.59	-0.22
T14HN	5.39E-03	0.99	1.60E-03	0.96	3.87E-03	1.00	2.93E-03	1.00	-3.37	-0.45
L15HN	2.86E-04	1.00	5.94E-04	0.87	1.80E-04	0.99	2.26E-04	0.84	-0.48	-0.22
E16HN	3.35E-04	1.00			2.41E-04	1.00	4.16E-04	0.90		
V17HN	3.02E-03	1.00	4.91E-03	0.99	2.92E-03	1.00	2.36E-03	1.00	-0.61	-0.38
E18HN	3.91E-04	1.00	1.02E-03	0.96	3.10E-04	1.00	3.59E-04	0.96	-0.38	-0.26
S20HN	3.26E-03	1.00	2.55E-03	0.98	1.45E-03	0.95	1.68E-03	0.98	-1.28	-0.23
D21HN	7.53E-04	0.99	9.96E-04	0.79	3.80E-04	0.99	5.22E-04	0.99	-0.76	-0.22
T22HN	1.38E-03	0.99	1.78E-03	0.97	7.87E-04	0.99	2.27E-04	0.84	-0.77	-0.06

N25HN	2.22E-03	1.00	2.65E-03	0.94	1.25E-03	0.99	1.38E-04	0.96	-0.83	-0.02
K27HN	1.57E-04	0.99			1.41E-04	0.99				
Q31HN	5.03E-05	0.96			4.73E-05	0.94	4.73E-05	0.84		
D32HN	1.85E-04	0.84	3.30E-04	0.68	1.44E-04	0.56	1.03E-04	0.66	-0.56	-0.21
K33HN	3.32E-03	0.99			2.90E-03	0.96	2.91E-03	0.99		
I36HN	9.44E-05	0.50	3.72E-04	0.61			4.57E-05	0.73	-0.25	
D39HN	5.02E-03	1.00			4.55E-03	1.00	3.69E-03	0.99		
Q40HN	4.54E-04	0.99	5.44E-04	0.76	4.06E-04	0.99	4.57E-04	0.99	-0.83	-0.64
Q41HN	4.79E-04	0.99	8.02E-04	0.92	3.65E-04	1.00	5.26E-04	0.96	-0.60	-0.35
L43HN	2.73E-03	1.00	4.07E-03	0.99	2.51E-03	1.00	2.17E-03	1.00	-0.67	-0.42
I44HN	1.15E-04	0.99			1.35E-04	0.98	1.88E-04	0.92		
A46HN	1.23E-03	0.99			1.11E-03	1.00	9.39E-04	0.99		
G47HN	3.48E-04	0.99	6.18E-04	0.96	3.24E-04	1.00	3.09E-04	0.99	-0.56	-0.44
Q49HN	2.17E-04	1.00	6.42E-04	0.92	1.99E-04	1.00	2.32E-04	0.94	-0.34	-0.29
E51HN	4.51E-03	0.99	5.47E-03	0.99	4.18E-03	1.00	3.63E-03	1.00	-0.83	-0.50
D52HN	1.94E-03	0.99	2.01E-03	0.95	1.65E-03	0.98	1.37E-03	0.97	-0.97	-0.43
R54HN	5.14E-04	0.98	3.76E-04	0.85	3.57E-04	0.99	5.08E-04	0.97	-1.37	-0.52
T55HN	9.13E-04	0.98	9.27E-04	0.94	7.83E-04	0.99	6.28E-04	1.00	-0.98	-0.42
L56HN	4.93E-04	0.98			3.58E-04	0.99	3.66E-04	0.96		
S57HN	1.27E-03	0.99	1.11E-03	0.95	8.95E-04	0.99	7.05E-04	1.00	-1.15	-0.31
D58HN	2.21E-03	0.98	2.18E-03	0.94	1.92E-03	0.98	1.49E-03	0.98	-1.01	-0.41
Y59HN	4.86E-04	0.98			3.29E-04	0.99	3.97E-04	0.99		

N60HN	8.50E-04	0.96	1.02E-03	0.83	7.88E-04	0.93	6.40E-04	0.97	-0.83	-0.44
I61HN	2.51E-04	1.00	5.69E-04	0.75	2.18E-04	0.99	3.06E-04	0.93	-0.44	-0.34
Q62HN	1.78E-03	0.99	1.90E-03	0.94	9.67E-05	0.90	6.87E-04	0.99	-0.94	-0.02
K63HN	3.54E-03	1.00	~ 1.705e-016	-12.91	2.99E-03	1.00	2.43E-03	1.00		
E64HN	3.98E-04	0.98	3.31E-04	0.48	1.60E-04	0.97	4.52E-04	0.90	-1.20	-0.20
S65HN	1.91E-03	0.99	1.79E-03	0.95	7.11E-05	0.95	7.36E-04	0.99	-1.07	-0.01
T66HN	2.06E-03	0.99	3.09E-03	0.98	1.16E-04	0.93	9.16E-04	1.00	-0.67	-0.02
L67HN	2.49E-04	0.99			9.13E-05	0.99	1.68E-04	0.91		
H68HN	3.36E-04	1.00	4.74E-04	0.83	3.09E-04	1.00	2.67E-04	0.99	-0.71	-0.44
L69HN	4.98E-04	1.00	6.77E-04	0.79	4.15E-04	1.00	3.47E-04	0.99	-0.73	-0.35
V70HN	2.37E-04	1.00	3.82E-04	0.46	2.05E-04	0.99	3.37E-04	0.87	-0.62	-0.46
L71HN	1.03E-03	0.99	2.13E-03	0.97	9.51E-04	0.98	7.73E-04	0.97	-0.48	-0.29
R72HN	3.99E-04	0.99	4.96E-04	0.91	3.13E-04	1.00	5.17E-04	0.92	-0.80	-0.47
L73HN	8.28E-05	0.97	4.20E-04	0.63	7.52E-05	0.95			-0.20	
R74HN	9.14E-04	1.00	1.24E-03	0.96	6.82E-04	0.99	6.86E-04	0.98	-0.74	-0.40
G75HN	3.61E-03	1.00			3.24E-03	1.00	2.64E-03	1.00		
G76HN	9.46E-04	1.00	4.19E-04	0.96	7.89E-04	1.00	9.83E-04	0.95	-2.26	-1.08

Table C- 17: List of fitted rates for Ubiquitin in AOT reverse micelles using the only points in the linear regime using (4-3)

Assignment	NOE	NOE R^2	ROE	ROE R^2	G3 6.1 ppm	G3 6.1 ppm R^2	G3 5.4 ppm	G3 5.4 R^2	No Correction	Corrected Ratio
Q2HN	1.87E-03	0.99	4.50E-04	0.77	1.74E-03	1.00	1.61E-03	0.99	-4.16	
I3HN	1.34E-04	0.91	2.25E-04	-4.71	9.46E-05	0.97	8.68E-05	0.85	-0.59	
F4HN	1.89E-04	0.94	1.34E-04	0.12			1.12E-04	0.71	-1.41	
V5HN	1.87E-04	0.95			1.69E-04	0.95	1.54E-04	0.89		
K6HN	1.31E-04	0.98			1.11E-04	0.83	9.76E-05	0.64		
T7HN	4.51E-04	0.99	4.83E-04	0.95	4.38E-04	0.96	1.82E-04	0.97	-0.94	-0.18
L8HN	1.56E-03	0.99	1.78E-03	0.97	1.60E-03	0.99	1.30E-03	0.98	-0.88	-0.57
T9HN	2.11E-03	0.99	1.64E-03	0.98	1.87E-03	1.00	4.18E-04	0.99	-1.29	-0.08
G10HN	1.15E-03	0.99	8.50E-04	0.81	9.89E-04	0.98	4.81E-04	0.99	-1.35	-0.22
K11HN	2.85E-03	0.99	1.41E-03	0.92	2.51E-03	0.99	7.41E-04	0.98	-2.02	-0.13
T12HN	9.41E-03	1.00			8.02E-03	1.00	5.49E-03	1.00	-7.62	-0.60
I13HN	2.40E-04	0.99	3.07E-04	0.90	2.08E-04	0.93	1.20E-04	0.91	-0.78	-0.22
T14HN	4.76E-03	1.00	1.11E-03	0.96	3.60E-03	1.00	2.88E-03	0.99	-4.28	-0.59
L15HN	2.32E-04	0.98	3.34E-04	0.84	1.59E-04	0.88	1.26E-04	0.78	-0.69	-0.23
E16HN	2.88E-04	0.95			2.52E-04	0.94	2.61E-04	0.90		
V17HN	2.73E-03	0.99	4.01E-03	0.99	2.83E-03	1.00	2.58E-03	1.00	-0.68	-0.60
E18HN	3.36E-04	0.99	7.80E-04	0.72	3.08E-04	0.98	2.94E-04	0.98	-0.43	-0.34
S20HN	2.96E-03	0.99	1.88E-03	0.99	1.38E-03	0.95	1.70E-03	0.99	-1.58	-0.27
D21HN	5.97E-04	0.99	6.61E-04	0.80	3.24E-04	0.97	3.90E-04	0.98	-0.90	-0.27
T22HN	1.12E-03	0.98	1.23E-03	1.00	6.06E-04	0.99	7.36E-05	-0.02	-0.90	-0.02

I23HN	2.29E-04	0.93			1.53E-04	0.97	9.38E-05	0.79		-0.35
N25HN	1.93E-03	0.99	1.77E-03	0.90	1.14E-03	0.99	1.43E-04	0.87	-1.09	-0.03
K27HN	1.08E-04	0.86			8.22E-05	0.86				
Q31HN	6.51E-05	0.69			6.32E-05	0.17	9.86E-05	0.64		
D32HN	1.58E-04	0.81	2.27E-04	0.84	1.71E-04	0.90	1.85E-04	0.87	-0.70	-0.85
K33HN	2.82E-03	0.95			2.43E-03	0.90	2.45E-03	0.95		
I36HN	9.48E-05	-1.25	2.85E-04	0.64			1.37E-04	0.56	-0.33	
D39HN	4.45E-03	0.99			4.20E-03	1.00	3.80E-03	0.99		
Q40HN	3.37E-04	0.99	4.36E-04	-0.54	3.08E-04	0.98	3.09E-04	0.97	-0.77	-0.62
Q41HN	3.92E-04	0.98	5.61E-04	0.90	3.36E-04	0.99	3.74E-04	0.98	-0.70	-0.50
L43HN	2.43E-03	1.00	3.32E-03	0.99	2.33E-03	1.00	2.23E-03	1.00	-0.73	-0.60
I44HN	8.86E-05	0.75			8.15E-05	0.52	6.64E-05	0.78		
A46HN	1.05E-03	0.94			1.02E-03	0.97	9.34E-04	0.99		
G47HN	2.82E-04	0.99	5.16E-04	0.92	2.56E-04	0.98	2.73E-04	0.99	-0.55	-0.45
Q49HN	2.06E-04	0.87	5.50E-04	0.96	2.25E-04	0.95	2.18E-04	0.88	-0.37	-0.41
E51HN	3.94E-03	1.00	4.21E-03	1.00	3.78E-03	1.00	3.49E-03	1.00	-0.93	-0.68
D52HN	1.92E-03	0.96	1.34E-03	0.96	1.86E-03	0.99	1.79E-03	0.98	-1.43	-1.12
R54HN	3.25E-04	0.95	2.86E-04	0.81	2.29E-04	0.93	2.43E-04	0.88	-1.14	-0.48
T55HN	6.71E-04	0.93	5.77E-04	0.87	5.31E-04	0.94	4.73E-04	0.93	-1.16	-0.49
L56HN	3.31E-04	0.94			2.29E-04	0.92	1.90E-04	0.92		
S57HN	1.01E-03	0.98	7.68E-04	0.95	6.50E-04	0.96	6.23E-04	0.97	-1.32	-0.40
D58HN	1.77E-03	0.97	1.39E-03	0.92	1.45E-03	0.94	1.30E-03	0.95	-1.27	-0.56
Y59HN	3.30E-04	0.93			2.32E-04	0.96	2.42E-04	0.91		

N60HN	9.06E-04	0.89	4.65E-04	-30.02	8.95E-04	0.88	8.68E-04	0.93	-1.95	-1.61
I61HN	2.49E-04	1.00	4.46E-04	-0.71	2.31E-04	0.94	2.45E-04	0.99	-0.56	-0.48
Q62HN	1.41E-03	0.97	1.21E-03	0.88	1.27E-04	0.85	6.47E-04	0.97	-1.16	-0.03
K63HN	3.21E-03	0.99			2.92E-03	1.00	2.67E-03	0.99		
E64HN	2.60E-04	0.93	1.49E-04	0.26	1.33E-04	0.84	1.70E-04	0.91	-1.74	-0.33
S65HN	1.52E-03	0.97	1.14E-03	0.96	1.14E-04	0.60	6.85E-04	0.97	-1.34	-0.03
T66HN	1.72E-03	0.99	2.29E-03	0.98	1.05E-04	0.75	7.71E-04	0.98	-0.75	-0.02
L67HN	1.92E-04	0.96			7.12E-05	0.53	1.11E-04	0.65		
H68HN	3.01E-04	0.99	3.62E-04	0.48	2.98E-04	0.99	3.02E-04	1.00	-0.83	-0.81
L69HN	4.48E-04	0.99	4.85E-04	0.86	4.44E-04	0.99	3.88E-04	0.98	-0.92	-0.64
V70HN	2.16E-04	1.00	2.89E-04	-1.07	1.98E-04	0.98	2.18E-04	0.89	-0.75	-0.61
L71HN	9.70E-04	0.95	1.68E-03	0.87	1.07E-03	0.98	1.05E-03	0.99	-0.58	-0.69
R72HN	3.18E-04	0.99	3.82E-04	0.88	2.92E-04	1.00	2.82E-04	0.99	-0.83	-0.62
L73HN	5.06E-05	0.65	3.17E-04	0.21	9.25E-06	0.07			-0.16	
R74HN	8.15E-04	0.98	9.58E-04	0.93	7.24E-04	0.98	7.80E-04	0.97	-0.85	-0.64
G75HN	3.28E-03	0.99			3.09E-03	1.00	2.83E-03	0.99		
G76HN	8.24E-04	1.00	3.08E-04	0.73	7.67E-04	1.00	7.47E-04	1.00	-2.68	-1.62

REFERENCES

1. Reddy, C. K., A. Das, and B. Jayaram. 2001. Do water molecules mediate protein-DNA recognition? Journal of Molecular Biology 314(3):619-632.
2. Chaplin, M. 2006. Do we underestimate the importance of water in cell biology? Nature Reviews Molecular Cell Biology 7:861. Perspective.
3. Pal, S. K., and A. H. Zewail. 2004. Dynamics of water in biological recognition. Chemical Reviews 104:2099-2123.
4. Grant, W. D. 2004. Life at low water activity. Philosophical transactions of the Royal Society of London. Series B, Biological sciences 359:1249-1266; discussion 1266-1247.
5. Hospital, A., M. Candotti, J. L. Gelpí, and M. Orozco. 2017. The Multiple Roles of Waters in Protein Solvation. The Journal of Physical Chemistry B 121(15):3636-3643.
6. Mattos, C. 2002. Protein-water interactions in a dynamic world. Trends in biochemical sciences 27:203-208.
7. Lilley, T. H. 2004. So, why is water biologically important? Philosophical transactions of the Royal Society of London. Series B, Biological sciences 359:1321-1322; discussion 1323-1328.
8. Bellissent-Funel, M.-C., A. Hassanali, M. Havenith, R. Henchman, P. Pohl, F. Sterpone, D. van der Spoel, Y. Xu, and A. E. Garcia. 2016. Water Determines the Structure and Dynamics of Proteins. Chemical Reviews 116(13):7673-7697.
9. Finney, J. L. 2004. Water? What's so special about it? Philosophical transactions of the Royal Society of London. Series B, Biological sciences 359:1145-1163; discussion 1163-1145, 1323-1148.
10. Ikura, T., Y. Urakubo, and N. Ito. 2004. Water-mediated interaction at a protein–protein interface. Chemical Physics 307(2):111-119.
11. Pace, C. N., S. Treviño, E. Prabhakaran, and J. M. Scholtz. 2004. Protein structure, stability and solubility in water and other solvents. Philosophical transactions of the Royal Society of London. Series B, Biological sciences 359:1225-1234; discussion 1234-1225.
12. Mitra, L., J.-B. Rouget, B. Garcia-Moreno, C. a. Royer, and R. Winter. 2008. Towards a quantitative understanding of protein hydration and volumetric properties. Chemphyschem : a European journal of chemical physics and physical chemistry 9:2715-2721.
13. Sinha, S. K., and S. Bandyopadhyay. 2011. Dynamic properties of water around a protein-DNA complex from molecular dynamics simulations. The Journal of chemical physics 135:135101.
14. King, J. T., and K. J. Kubarych. 2012. Site-specific coupling of hydration water and protein flexibility studied in solution with ultrafast 2D-IR spectroscopy. J Am Chem Soc 134(45):18705-18712.
15. Rahaman, O., S. Melchionna, D. Laage, and F. Sterpone. 2013. The effect of protein composition on hydration dynamics. Phys Chem Chem Phys 15(10):3570-3576.
16. Laage, D., T. Elsaesser, and J. T. Hynes. 2017. Water Dynamics in the Hydration Shells of Biomolecules. Chem Rev 117(16):10694-10725.
17. Bowron, D. T. 2004. Structure and interactions in simple solutions. Philosophical transactions of the Royal Society of London. Series B, Biological sciences 359:1167-1179; discussion 1179-1180.
18. Fayer, M. D. 2011. Water in a crowd. Physiology 26(6):381-392.
19. Haider, K., L. Wickstrom, S. Ramsey, M. K. Gilson, and T. Kurtzman. 2016. Enthalpic Breakdown of Water Structure on Protein Active-Site Surfaces. The Journal of Physical Chemistry B 120(34):8743-8756.
20. Halling, P. J. 2004. What can we learn by studying enzymes in non-aqueous media? Philosophical transactions of the Royal Society of London. Series B, Biological sciences 359:1287-1296; discussion 1296-1287, 1323-1288.

21. Pizzitutti, F., M. Marchi, F. Sterpone, and P. J. Rossky. 2007. How protein surfaces induce anomalous dynamics of hydration water. The Journal of chemical physics B 111(26):7584-7590.
22. Rand, R. P. 2004. Probing the role of water in protein conformation and function. Philosophical transactions of the Royal Society of London. Series B, Biological sciences 359:1277-1284; discussion 1284-1275.
23. Raschke, T. M. 2006. Water structure and interactions with protein surfaces. Current Opinions in Structural Biology 16(2):152-159.
24. Smith, J. C., F. Merzel, A.-N. Bondar, A. Tournier, and S. Fischer. 2004. Structure, dynamics and reactions of protein hydration water. Philosophical transactions of the Royal Society of London. Series B, Biological sciences 359:1181-1189; discussion 1189-1190.
25. Vaitheeswaran, S., H. Yin, J. C. Rasaiah, and G. Hummer. 2004. Water clusters in nonpolar cavities. Proceedings of the National Academy of Sciences of the United States of America 101(49):17002-17005.
26. Vodolazkaya, N. A., N. O. Mchedlov-Petrossyan, N. V. Salamanova, Y. N. Surov, and A. O. Doroshenko. 2010. Molecular spectroscopy studies of solvent properties of dispersed 'water pools' Fluorescein and 2,7-dichlorofluorescein in reversed AOT-based microemulsions. Journal of Molecular Liquids 157:105-112.
27. Fayer, M. D., and N. E. Levinger. 2010. Analysis of water in confined geometries and at interfaces. Annual Review of Analytical Chemistry 3:89-107.
28. Duboue-Dijon, E., and D. Laage. 2014. Comparative study of hydration shell dynamics around a hyperactive antifreeze protein and around ubiquitin. Journal of Chemical Physics 141(22):22D529.
29. Li, T., A. A. Hassanali, Y. T. Kao, D. Zhong, and S. J. Singer. 2007. Hydration dynamics and time scales of coupled water-protein fluctuations. J Am Chem Soc 129(11):3376-3382.
30. Smith, J. C., F. Merzel, C. S. Verma, and S. Fischer. 2002. Protein hydration water: Structure and thermodynamics. Journal of Molecular Liquids 101(1):27-33.
31. Modig, K., E. Liepinsh, G. Otting, and B. Halle. 2004. Dynamics of protein and peptide hydration. Journal of the American Chemical Society 126:102-114.
32. Dahanayake, J. N., and K. R. Mitchell-Koch. 2018. Entropy connects water structure and dynamics in protein hydration layer. Physical chemistry chemical physics 20(21):14765-14777.
33. Ebbinghaus, S., S. J. Kim, M. Heyden, X. Yu, U. Heugen, M. Gruebele, D. M. Leitner, and M. Havenith. 2007. An extended dynamical hydration shell around proteins. Proceedings of the National Academy of Sciences 104(52):20749-20752.
34. Merzel, F., and J. C. Smith. 2002. Is the first hydration shell of lysozyme of higher density than bulk water? Proceedings of the National Academy of Sciences of the United States of America 99:5378-5383.
35. Zhang, L., L. Wang, Y.-T. Kao, W. Qiu, Y. Yang, O. Okobiah, and D. Zhong. 2007. Mapping hydration dynamics around a protein surface. Proceedings of the National Academy of Sciences of the United States of America 104:18461-18466.
36. Qiu, W., Y. T. Kao, L. Zhang, Y. Yang, L. Wang, W. E. Stites, D. Zhong, and A. H. Zewail. 2006. Protein surface hydration mapped by site-specific mutations. Proceedings of the National Academy of Sciences 103(38):13979-13984.
37. Carugo, O. 2016. When proteins are completely hydrated in crystals. International journal of biological macromolecules 89:137-143.
38. Fayer, M. D. 2012. Dynamics of Water Interacting with Interfaces, Molecules, and Ions. Accounts of Chemical Research 45(1):3-14.
39. Privalov, P. L., and C. Crane-Robinson. 2017. Role of water in the formation of macromolecular structures. European Biophysics Journal 46(3):203-224.

40. Park, S., D. E. Moilanen, and M. D. Fayer. 2008. Water dynamics--the effects of ions and nanoconfinement. The Journal of Physical Chemistry B 112(17):5279-5290.
41. Zhu, Z., H. Guo, X. Jiang, Y. Chen, B. Song, Y. Zhu, and S. Zhuang. 2018. Reversible Hydrophobicity–Hydrophilicity Transition Modulated by Surface Curvature. The Journal of Physical Chemistry Letters 9(9):2346-2352.
42. Nucci, N. V., and J. M. Vanderkooi. 2005. Temperature dependence of hydrogen bonding and freezing behavior of water in reverse micelles. The journal of physical chemistry. B 109:18301-18309.
43. Kauzmann, W. 1959. Some factors in the interpretation of protein denaturation. Advances in protein chemistry 14:1-63.
44. Tanford, C. 1979. Interfacial free energy and the hydrophobic effect. Proceedings of the National Academy of Sciences of the United States of America 76:4175-4176.
45. Tanford, C. 1997. How protein chemists learned about the hydrophobic factor. Protein Science 6(6):1358-1366.
46. Chandler, D. 2005. Interfaces and the driving force of hydrophobic assembly. Nature 437(7059):640-647.
47. Huang, D. M., and D. Chandler. 2000. Temperature and length scale dependence of hydrophobic effects and their possible implications for protein folding. Proceedings of the National Academy of Sciences 97(15):8324. 10.1073/pnas.120176397.
48. Huang, D. M., and D. Chandler. 2002. The Hydrophobic Effect and the Influence of Solute−Solvent Attractions. The Journal of Physical Chemistry B 106(8):2047-2053.
49. Sharp, K. A., A. Nicholls, R. F. Fine, and B. Honig. 1991. Reconciling the magnitude of the microscopic and macroscopic hydrophobic effects. Science 252(5002):106-109.
50. Ben-Naim, A. 2011. The Rise and Fall of the Hydrophobic Effect in Protein Folding and Protein-Protein Association, and Molecular Recognition. Open Journal of Biophysics 01(01):1-7.
51. Rodier, F., R. P. Bahadur, P. Chakrabarti, and J. Janin. 2005. Hydration of protein-protein interfaces. Proteins 60(1):36-45.
52. Levy, Y., and J. N. Onuchic. 2006. Water mediation in protein folding and molecular recognition. Annual review of biophysics and biomolecular structure 35:389-415.
53. Clore, G. M., A. Bax, P. T. Wingfield, and A. M. Gronenborn. 1990. Identification and localization of bound internal water in the solution structure of interleukin 1 beta by heteronuclear three-dimensional 1H rotating-frame Overhauser 15N-1H multiple quantum coherence NMR spectroscopy. Biochemistry 29(24):5671-5676.
54. Dwyer, J. J., a. G. Gittis, D. a. Karp, E. E. Lattman, D. S. Spencer, W. E. Stites, and B. García-Moreno E. 2000. High apparent dielectric constants in the interior of a protein reflect water penetration. Biophysical journal 79:1610-1620.
55. Armstrong, B. D., J. Choi, C. Lopez, D. A. Wesener, W. Hubbell, S. Cavagnero, and S. Han. 2011. Site-specific hydration dynamics in the nonpolar core of a molten globule by dynamic nuclear polarization of water. Journal of the American Chemical Society 133(15):5987-5995.
56. Jiang, Y., V. Ruta, J. Chen, A. Lee, and R. MacKinnon. 2003. The principle of gating charge movement in a voltage-dependent K+ channel. Nature 423(6935):42-48.
57. Luecke, H., H. T. Richter, and J. K. Lanyi. 1998. Proton transfer pathways in bacteriorhodopsin at 2.3 angstrom resolution. Science 280(5371):1934-1937.
58. Dey, A., F. E. Jenny, M. W. W. Adams, E. Babini, Y. Takahashi, K. Fukuyama, K. O. Hodgson, B. Hedman, and E. I. Solomon. 2007. Solvent tuning of electrochemical potentials in the active sites of HiPIP versus ferredoxin. Science 318:1464-1468.
59. Bartlett, G. J., C. T. Porter, N. Borkakoti, and J. M. Thornton. 2002. Analysis of catalytic residues in enzyme active sites. Journal of Molecular Biology 324(1):105-121.
60. Garcia-Moreno, B., J. J. Dwyer, A. G. Gittis, E. E. Lattman, D. S. Spencer, and W. E. Stites. 1998. Solvent penetration may be responsible for the high dielectric constant inside a protein. Biophysical Journal 74(2):A132-A132.

61. Rashin, A. A., and B. Honig. 1984. On the environment of ionizable groups in globular proteins. Journal of Molecular Biology 173(4):515-521.
62. Chong, Y., A. Kleinhammes, and Y. Wu. 2016. Protein dynamics and thermodynamics crossover at 10°C: Different roles of hydration at hydrophilic and hydrophobic groups. Chemical Physics Letters 664:108-113.
63. Sterpone, F., G. Stirnemann, and D. Laage. 2012. Magnitude and molecular origin of water slowdown next to a protein. Journal of the American Chemical Society 134(9):4116-4119.
64. Roy, V. P., and K. J. Kubarych. 2017. Interfacial Hydration Dynamics in Cationic Micelles Using 2D-IR and NMR. Journal of Physical Chemistry B 121(41):9621-9630.
65. Biswas, R., and B. Bagchi. 2018. Anomalous water dynamics at surfaces and interfaces: synergistic effects of confinement and surface interactions. Journal of physics. Condensed matter 30(1):013001.
66. Moilanen, D. E., N. E. Levinger, D. B. Spry, and M. D. Fayer. 2007. Confinement or the nature of the interface? Dynamics of nanoscopic water. Journal of the American Chemical Society 129:14311-14318.
67. Meister, K., S. Strazdaite, A. L. DeVries, S. Lotze, L. L. Olijve, I. K. Voets, and H. J. Bakker. 2014. Observation of ice-like water layers at an aqueous protein surface. Proceedings of the National Academy of Sciences 111(50):17732-17736.
68. Piletic, I. R., D. E. Moilanen, D. B. Spry, N. E. Levinger, and M. D. Fayer. 2006. Testing the core/shell model of nanoconfined water in reverse micelles using linear and nonlinear IR spectroscopy. The journal of physical chemistry. A 110:4985-4999.
69. Lum, K., D. Chandler, and J. D. Weeks. 1999. Hydrophobicity at Small and Large Length Scales. The Journal of Physical Chemistry B 103:4570-4577.
70. Clark, D. S. 2004. Characteristics of nearly dry enzymes in organic solvents: implications for biocatalysis in the absence of water. Philosophical transactions of the Royal Society of London. Series B, Biological sciences 359:1299-1307; discussion 1307, 1323-1298.
71. Cametti, C., S. Marchetti, C. M. Gambi, and G. Onori. 2011. Dielectric relaxation spectroscopy of lysozyme aqueous solutions: analysis of the delta-dispersion and the contribution of the hydration water. Journal of Physical Chemistry B 115(21):7144-7153.
72. Nickels, J. D., H. O'Neill, L. Hong, M. Tyagi, G. Ehlers, K. L. Weiss, Q. Zhang, Z. Yi, E. Mamontov, J. C. Smith, and A. P. Sokolov. 2012. Dynamics of protein and its hydration water: neutron scattering studies on fully deuterated GFP. Biophysical Journal 103(7):1566-1575.
73. Zaccai, G. 2004. The effect of water on protein dynamics. Philosophical transactions of the Royal Society of London. Series B, Biological sciences 359:1269-1275; discussion 1275, 1323-1268.
74. Das, D. K., A. Patra, and R. K. Mitra. 2016. Preferential solvation of lysozyme in dimethyl sulfoxide/water binary mixture probed by terahertz spectroscopy. Biophysical chemistry 216:31-36.
75. Halle, B. 2004. Protein hydration dynamics in solution: a critical survey. Philosophical Transactions of the Royal Society B: Biological Sciences 359:1204-1207,1323-1328.
76. Makarov, V. A., B. K. Andrews, P. E. Smith, and B. M. Pettitt. 2000. Residence times of water molecules in the hydration sites of myoglobin. Biophysical Journal 79(6):2966-2974.
77. Fuller, W., T. Forsyth, and A. Mahendrasingam. 2004. Water-DNA interactions as studied by X-ray and neutron fibre diffraction. Philosophical transactions of the Royal Society of London. Series B, Biological sciences 359:1237-1247; discussion 1247-1238.
78. Amann-Winkel, K., M. C. Bellissent-Funel, L. E. Bove, T. Loerting, A. Nilsson, A. Paciaroni, D. Schlesinger, and L. Skinner. 2016. X-ray and Neutron Scattering of Water. Chemical Reviews 116(13):7570-7589.

79. Halle, B. 2004. Biomolecular cryocrystallography: Structural changes during flash-cooling. Proceedings of the National Academy of Sciences of the United States of America 101(14):4793-4798.
80. Nakasako, M. 2004. Water-protein interactions from high-resolution protein crystallography. Philosophical transactions of the Royal Society of London. Series B, Biological sciences 359:1191-1204; discussion 1204-1196.
81. Sheu, S. Y., and D. Y. Yang. 2010. Determination of protein surface hydration shell free energy of water motion: theoretical study and molecular dynamics simulation. The Journal of Physical Chemistry B 114(49):16558-16566.
82. Guillot, B. 2002. A reappraisal of what we have learnt during three decades of computer simulations on water. Journal of Molecular Liquids 101(1):219-260.
83. Armstrong, B. D., and S. Han. 2007. A new model for Overhauser enhanced nuclear magnetic resonance using nitroxide radicals. The Journal of chemical physics 127(10):104508.
84. Armstrong, B. D., and S. Han. 2009. Overhauser dynamic nuclear polarization to study local water dynamics. Journal of the American Chemical Society 131(13):4641-4647.
85. Franck, J. M., R. Kausik, and S. Han. 2013. Overhauser Dynamic Nuclear Polarization-Enhanced NMR Relaxometry. Microporous and mesoporous materials : the official journal of the International Zeolite Association 178:113-118.
86. Franck, J. M., M. Sokolovski, N. Kessler, E. Matalon, M. Gordon-Grossman, S. I. Han, D. Goldfarb, and A. Horovitz. 2014. Probing water density and dynamics in the chaperonin GroEL cavity. Journal of the American Chemical Society 136(26):9396-9403.
87. Cheng, C. Y., and S. Han. 2013. Dynamic nuclear polarization methods in solids and solutions to explore membrane proteins and membrane systems. Annu Rev Phys Chem 64:507-532.
88. Qin, Y., L. Wang, and D. Zhong. 2016. Dynamics and mechanism of ultrafast water-protein interactions. Proceedings of the National Academy of Sciences 113(30):8424-8429.
89. Otting, G., and K. Wuthrich. 1989. Studies of protein hydration in aqueous solution by direct NMR observation of individual protein-bound water molecules. Journal of the American Chemical Society 111(5):1871-1875.
90. Otting, G., E. Liepinsh, and K. Wuthrich. 1991. Protein hydration in aqueous solution. Science 254(5034):974-980.
91. Wüthrich, K., G. Otting, and E. Liepinsh. 1992. Protein hydration in aqueous solution. Faraday discussions 93:35-45.
92. Grzesiek, S., and A. Bax. 1993. Measurement of amide proton exchange rates and NOEs with water in 13C/15N-enriched calcineurin B. Journal of biomolecular NMR 3(6):627-638.
93. Otting, G. 1997. NMR studies of water bound to biological molecules. Progress in Nuclear Magnetic Resonance Spectroscopy 31:259-285.
94. Macura, S., and R. R. Ernst. 1980. Elucidation of cross relaxation in liquids by two-dimensional N.M.R. spectroscopy. Molecular Physics 41:95-117.
95. Deverell, C., R. E. Morgan, and J. H. Strange. 1970. Studies of chemical exchange by nuclear magnetic relaxation in the rotating frame. Molecular Physics 18:553-559.
96. Bothner-By, A. A., R. L. Stephens, J. Lee, C. D. Warren, and R. W. Jeanloz. 1984. Structure determination of a tetrasaccharide: transient nuclear Overhauser effects in the rotating frame. Journal of the American Chemical Society 103(3):811-813.
97. Bax, A., and D. G. Davis. 1985. Practical Aspects of Two-Dimensional Transverse NOE Spectroscopy. Journal of Magnetic Resonance 63(1):207-213.
98. Bax, A., and S. Grzesiek. 2007. ROESY. eMagRes.
99. Ayant, Y., E. Belorizky, J. Aluzon, and J. Gallice. 1975. Calcul des densités spectrales résultant d'un mouvement aléatoire de translation en relaxation par interaction dipolaire magnétique dans les liquides. J. Physique 36(10):991-1004.

100. Ayant, Y., E. Belorizky, P. Fries, and J. Rosset. 1977. Effet des interactions dipolaires magne´tiques intermole´culaires sur la relaxation nucle´aire de mole´cules polyatomiques dans les liquides. J. Physique 38:325-337.
101. Brüschweiler, R., and P. E. Wright. 1994. Water self-diffusion model for protein-water NMR cross-relaxation. Chemical Physics Letters 229:75-81.
102. Halle, B. 2003. Cross-relaxation between macromolecular and solvent spins: The role of long-range dipole couplings. The Journal of Chemical Physics 119:12372.
103. Braun, D., M. Schmollngruber, and O. Steinhauser. 2017. Revival of the Intermolecular Nuclear Overhauser Effect for Mapping Local Protein Hydration Dynamics. Journal of physical Chemistry Letters 8(14):3421-3426.
104. Gruschus, J. M., and J. A. Ferretti. 2001. Quantitative measurement of water diffusion lifetimes at a protein/DNA interface by NMR. Journal of Biomolecular NMR 20(2):111-126.
105. Dobson, C. M., L.-Y. Lian, C. Redfield, and K. D. Topping. 1986. Measurement of hydrogen exchange rates using 2D NMR spectroscopy. Journal of Magnetic Resonance 69(2):201-209.
106. van de Ven, F. J. M., H. G. J. M. Janssen, A. Gräslund, and C. W. Hilbers. 1988. Chemically relayed nuclear overhauser effects. Connectivities between resonances of nonexchangeable protons and water. Journal of Magnetic Resonance 79(2):221-235.
107. Bax, A., V. Sklenář, and M. F. Summers. 1986. Direct identification of relayed nuclear overhauser effects. Journal of Magnetic Resonance 70(2):327-331.
108. Jeener, J., B. Meier, P. Bachmann, and R. Ernst. 1979. Investigation of exchange processes by two‐dimensional NMR spectroscopy. The Journal of chemical physics 71(11):4546-4553.
109. Luisi, P. L., M. Giomini, M. P. Pileni, and B. H. Robinson. 1988. Reverse micelles as hosts for proteins and small molecules. Biochimica et biophysica acta 947:209-246.
110. De, T. K., and A. Maitra. 1995. Solution behaviour of Aerosol OT in non-polar solvents. Advances in Colloid and Interface Science 59:95-193.
111. Valdez, D., J. Y. Le Huerou, M. Gindre, W. Urbach, and M. Waks. 2001. Hydration and protein folding in water and in reverse micelles: Compressibility and volume changes. Biophysical Journal 80:2751-2760.
112. Sedgwick, M. A., D. C. Crans, and N. E. Levinger. 2009. What Is Inside a Nonionic Reverse Micelle? Probing the Interior of Igepal Reverse Micelles Using Decavanadate. Langmuir 25:5496-5503.
113. Trivedi, R., and U. B. Kompella. 2010. Nanomicellar formulations for sustained drug delivery: strategies and underlying principles. Nanomedicine (Lond) 5(3):485-505.
114. Fuglestad, B., K. Gupta, A. J. Wand, and K. A. Sharp. 2016. Characterization of Cetyltrimethylammonium Bromide/Hexanol Reverse Micelles by Experimentally Benchmarked Molecular Dynamics Simulations. Langmuir 32(7):1674-1684.
115. Brian Fuglestad, Bryan S. Marques, Christine Jorge, Nicole E. Kerstetter, Kathleen G. Valentine, and A. J. Wand. 2018. Reverse Micelle Encapsulation of Proteins for NMR Spectroscopy. Methods in Enzymology.
116. Nucci, N. V., K. G. Valentine, and A. J. Wand. 2014. High-resolution NMR spectroscopy of encapsulated proteins dissolved in low-viscosity fluids. Journal of Magnetic Resonance 241:137-147.
117. Nucci, N. V., B. S. Marques, S. Bedard, J. Dogan, J. M. Gledhill Jr., V. R. Moorman, R. W. Peterson, K. G. Valentine, A. L. Wand, and A. J. Wand. 2011. Optimization of NMR spectroscopy of encapsulated proteins dissolved in low viscosity fluids. Journal of Biomolecular Nmr 50:421-430.
118. Ehrhardt, M. R., P. F. Flynn, and A. J. Wand. 1999. Preparation of encapsulated proteins dissolved in low viscosity fluids. Journal of Biomolecular NMR 14(1):75-78.

119. Babu, C. R., P. F. Flynn, and A. J. Wand. 2001. Validation of protein structure from preparations of encapsulated proteins dissolved in low viscosity fluids. Journal of the American Chemical Society 123(11):2691-2692.
120. Flynn, P. F., and A. J. Wand. 2001. High-resolution nuclear magnetic resonance of encapsulated proteins dissolved in low viscosity fluids. Nuclear Magnetic Resonance of Biological Macromolecules, Pt B 339:54-70.
121. Babu, C. R., P. F. Flynn, and A. J. Wand. 2003. Preparation, characterization, and NMR spectroscopy of encapsulated proteins dissolved in low viscosity fluids. Journal of Biomolecular Nmr 25(4):313-323.
122. Peterson, R. W., M. S. Pometun, Z. S. Shi, and A. J. Wand. 2005. Novel surfactant mixtures for NMR spectroscopy of encapsulated proteins dissolved in low-viscosity fluids. Protein Science 14(11):2919-2921.
123. Shi, Z. S., R. W. Peterson, and A. J. Wand. 2005. New reverse micelle surfactant systems optimized for high-resolution NMR Spectroscopy of encapsulated proteins. Langmuir 21(23):10632-10637.
124. Kielec, J. M., K. G. Valentine, C. R. Babu, and A. J. Wand. 2009. Reverse Micelles in Integral Membrane Protein Structural Biology by Solution NMR Spectroscopy. Structure 17(3):345-351.
125. Nucci, N. V., M. S. Pometun, and A. J. Wand. 2011. Site-resolved measurement of water-protein interactions by solution NMR. Nature Structural and Molecular Biology 18:245-249.
126. Nucci, N. V., M. S. Pometun, and A. J. Wand. 2011. Mapping the hydration dynamics of ubiquitin. Journal of the American Chemical Society 133(32):12326-12329.
127. O'Brien, E. S., N. V. Nucci, B. Fuglestad, C. Tommos, and A. J. Wand. 2015. Defining the Apoptotic Trigger THE INTERACTION OF CYTOCHROME c AND CARDIOLIPIN. Journal of Biological Chemistry 290(52):30879-30887.
128. Valentine, K. G., G. Mathies, S. Bedard, N. V. Nucci, I. Dodevski, M. A. Stetz, T. V. Can, R. G. Griffin, and A. J. Wand. 2014. Reverse Micelles As a Platform for Dynamic Nuclear Polarization in Solution NMR of Proteins. Journal of the American Chemical Society 136(7):2800-2807.
129. Valentine, K. G., R. W. Peterson, J. S. Saad, M. F. Summers, X. Z. Xu, J. B. Ames, and A. J. Wand. 2010. Reverse Micelle Encapsulation of Membrane-Anchored Proteins for Solution NMR Studies. Structure 18(1):9-16.
130. Tan, H. S., I. R. Piletic, and M. D. Fayer. 2005. Orientational dynamics of water confined on a nanometer length scale in reverse micelles. The Journal of Chemical Physics 122(17):174501.
131. Baruah, B., J. M. Roden, M. Sedgwick, N. M. Correa, D. C. Crans, and N. E. Levinger. 2006. When is water not water? Exploring water confined in large reverse micelles using a highly charged inorganic molecular probe. Journal of the American Chemical Society 128:12758-12765.
132. Crans, D. C., and N. E. Levinger. 2012. The conundrum of pH in water nanodroplets: sensing pH in reverse micelle water pools. Accounts of chemical research 45(10):1637-1645.
133. Wiebenga-Sanford, B. P., J. DiVerdi, C. D. Rithner, and N. E. Levinger. 2016. Nanoconfinement's Dramatic Impact on Proton Exchange between Glucose and Water. The Journal of Physical Chemistry Letters 7(22):4597-4601.
134. Zhou, H. X., and K. A. Dill. 2001. Stabilization of proteins in confined spaces. Biochemistry 40(38):11289-11293.
135. Dodevski, I., N. V. Nucci, K. G. Valentine, G. K. Sidhu, E. S. O'Brien, A. Pardi, and A. J. Wand. 2014. Optimized Reverse Micelle Surfactant System for High-Resolution NMR Spectroscopy of Encapsulated Proteins and Nucleic Acids Dissolved in Low Viscosity Fluids. Journal of the American Chemical Society 136(9):3465-3474.

136. Senske, M., A. E. Smith, and G. J. Pielak. 2016. Protein Stability in Reverse Micelles. Angewandte Chemie (International ed. in English) 55(11):3586-3589.
137. Marques, B. S., N. V. Nucci, I. Dodevski, K. W. Wang, E. A. Athanasoula, C. Jorge, and A. J. Wand. 2014. Measurement and control of pH in the aqueous interior of reverse micelles. Journal of Physical Chemistry B 118(8):2020-2031.
138. Lefebvre, B. G., W. Liu, R. W. Peterson, K. G. Valentine, and A. J. Wand. 2005. NMR spectroscopy of proteins encapsulated in a positively charged surfactant. Journal of Magnetic Resonance 175(1):158-162.
139. Levitt, M., and B. H. Park. 1993. Water: now you see it, now you don't. Structure 1(4):223-226.
140. Kajander, T., P. C. Kahn, S. H. Passila, D. C. Cohen, L. Lehtio, W. Adolfsen, J. Warwicker, U. Schell, and A. Goldman. 2000. Buried charged surface in proteins. Structure 8(11):1203-1214.
141. Denisov, V. P., J. L. Schlessman, B. García-Moreno E, and B. Halle. 2004. Stabilization of internal charges in a protein: water penetration or conformational change? Biophysical journal 87:3982-3994.
142. Warshel, A., P. K. Sharma, M. Kato, Y. Xiang, H. Liu, and M. H. Olsson. 2006. Electrostatic basis for enzyme catalysis. Chemical Reviews 106(8):3210-3235.
143. Keinan, S., J. M. Nocek, B. M. Hoffman, and D. N. Beratan. 2012. Interfacial hydration, dynamics and electron transfer: multi-scale ET modeling of the transient [myoglobin, cytochrome b5] complex. Physical Chemistry Chemical Physics 14(40):13881-13889. 10.1039/C2CP41949A.
144. Schlessman, J. L., C. Abe, A. Gittis, D. A. Karp, M. A. Dolan, and E. B. Garcia-Moreno. 2008. Crystallographic study of hydration of an internal cavity in engineered proteins with buried polar or ionizable groups. Biophysical Journal 94(8):3208-3216.
145. Franck, J. M., A. Pavlova, J. a. Scott, and S. Han. 2013. Quantitative cw Overhauser effect dynamic nuclear polarization for the analysis of local water dynamics. Progress in nuclear magnetic resonance spectroscopy 74:33-56.
146. Peng, J. W. 2012. Exposing the Moving Parts of Proteins with NMR Spectroscopy. Journal of physical Chemistry Letters 3(8):1039-1051.
147. Cotton, F. A., E. E. Hazen, and M. J. Legg. 1979. Staphylococcal nuclease: proposed mechanism of action based on structure of enzyme-thymidine 3',5'-bisphosphate-calcium ion complex at 1.5-A resolution. Proceedings of the National Academy of Sciences of the United States of America 76:2551-2555.
148. Nguyen, D. M., R. Leila Reynald, A. G. Gittis, and E. E. Lattman. 2004. X-ray and thermodynamic studies of staphylococcal nuclease variants I92E and I92K: insights into polarity of the protein interior. Journal of Molecular Biology 341(2):565-574.
149. Chimenti, M. S., C. A. Castaneda, A. Majumdar, and B. Garcia-Moreno. 2011. Structural Origins of High Apparent Dielectric Constants Experienced by Ionizable Groups in the Hydrophobic Core of a Protein. Journal of Molecular Biology 405(2):361-377.
150. Gilson, M. K., and B. H. Honig. 1986. The dielectric constant of a folded protein. Biopolymers 25(11):2097-2119.
151. García-Moreno, B., J. J. Dwyer, a. G. Gittis, E. E. Lattman, D. S. Spencer, and W. E. Stites. 1997. Experimental measurement of the effective dielectric in the hydrophobic core of a protein. Biophysical chemistry 64:211-224.
152. Fitch, C. A., D. A. Karp, K. K. Lee, W. E. Stites, E. E. Lattman, and B. Garcia-Moreno. 2002. Experimental pK(a) values of buried residues: Analysis with continuum methods and role of water penetration. Biophysical Journal 82(6):3289-3304.
153. Isom, D. G., B. R. Cannon, C. A. Castañeda, A. Robinson, and B. García-Moreno. 2008. High tolerance for ionizable residues in the hydrophobic interior of proteins. Proceedings of the National Academy of Sciences of the United States of America 105:17784-17788.

154. Isom, D. G., C. A. Castaneda, P. D. Velu, and B. Garcia-Moreno. 2010. Charges in the hydrophobic interior of proteins. Proceedings of the National Academy of Sciences of the United States of America 107(37):16096-16100.
155. Damjanovic, A., B. R. Brooks, and E. B. Garcia-Moreno. 2011. Conformational Relaxation and Water Penetration Coupled to Ionization of Internal Groups in Proteins. Journal of Physical Chemistry A 115(16):4042-4053.
156. Damjanovic, A., B. Garcia-Moreno, E. E. Lattman, and A. E. Garcia. 2005. Molecular dynamics study of water penetration in staphylococcal nuclease. Proteins-Structure Function and Bioinformatics 60(3):433-449.
157. Damjanovic, A., B. Garcia-Moreno, E. E. Lattman, and A. E. Garcia. 2005. Molecular dynamics study of hydration of the protein interior. Computer Physics Communications 169(1-3):126-129.
158. Karp, D. A., A. G. Gittis, M. R. Stahley, C. A. Fitch, W. E. Stites, and B. Garcia-Moreno. 2007. High apparent dielectric constant inside a protein reflects structural reorganization coupled to the ionization of an internal Asp. Biophysical Journal 92(6):2041-2053.
159. Damjanovic, A., X. W. Wu, B. Garcia-Moreno, and B. R. Brooks. 2008. Backbone Relaxation Coupled to the Ionization of Internal Groups in Proteins: A Self-Guided Langevin Dynamics Study. Biophysical Journal 95(9):4091-4101.
160. Abel, E. W., T. P. J. Coston, K. G. Orrell, V. Šik, and D. Stephenson. 1986. Two-dimensional NMR exchange spectroscopy. Quantitative treatment of multisite exchanging systems. Journal of Magnetic Resonance 70(1):34-53.
161. Bai, Y., J. S. Milne, L. Mayne, and S. W. Englander. 1993. Primary structure effects on peptide group hydrogen exchange. Proteins: Structure, Function, and Bioinformatics(17):75-86.
162. Liepinsh, E., and G. Otting. 1996. Proton exchange rates from amino acid side chains—implications for image contrast. Magnetic resonance in medicine 35(1):30-42.
163. Smallcombe, S. H., S. L. Patt, and P. A. Keifer. 1995. WET Solvent Suppression and Its Applications to LC NMR and High-Resolution NMR Spectroscopy. Journal of Magnetic Resonance, Series A 117(2):295-303.
164. Spencer, D. S., D. Weiss, W. E. Stites, B. Garcia-Moreno, J. J. Dwyer, A. G. Gittis, and E. E. Lattman. 1998. The pK(a) of buried ionizable groups in staph nuclease: An experimental measure of the dielectric constant of a protein interior. Biophysical Journal 74(2):A170-A170.
165. Gardner, K. H., and L. E. Kay. 1998. The use of 2H, 13C, 15N multidimensional NMR to study the structure and dynamics of proteins. Annual review of biophysics and biomolecular structure 27:357-406.
166. Renner, C., M. Schleicher, L. Moroder, and T. A. Holak. 2002. Practical aspects of the 2D 15N-{1H}-NOE experiment. Journal of Biomolecular NMR 23(1):23-33. journal article.
167. Wang, C., M. Rance, and A. G. Palmer. 2003. Mapping Chemical Exchange in Proteins with MW > 50 kD. Journal of the American Chemical Society 125(30):8968-8969.
168. Damjanovic, A., J. L. Schlessman, C. A. Fitch, A. E. Garcia, and B. Garcia-Moreno. 2007. Role of flexibility and polarity as determinants of the hydration of internal cavities and pockets in proteins. Biophysical Journal 93(8):2791-2804.
169. Alexandrescu, A. T., W. Jahnke, R. Wiltscheck, and M. J. Blommers. 1996. Accretion of structure in staphylococcal nuclease: an 15N NMR relaxation study. Journal of Molecular Biology 260(4):570-587.
170. Hyberts, S. G., S. A. Robson, and G. Wagner. 2013. Exploring signal-to-noise ratio and sensitivity in non-uniformly sampled multi-dimensional NMR spectra. Journal of Biomolecular NMR 55(2):167-178.
171. Hyberts, S. G., H. Arthanari, S. A. Robson, and G. Wagner. 2014. Perspectives in magnetic resonance: NMR in the post-FFT era. Journal of Magnetic Resonance 241:60-73.

172. Hyberts, S. G., S. A. Robson, and G. Wagner. 2017. Interpolating and extrapolating with hmsIST: seeking a tmax for optimal sensitivity, resolution and frequency accuracy. Journal of Biological NMR.
173. Hyberts, S. G., K. Takeuchi, and G. Wagner. 2010. Poisson-gap sampling and forward maximum entropy reconstruction for enhancing the resolution and sensitivity of protein NMR data. Journal of the American Chemical Society 132(7):2145-2147.
174. Donoho, D. L. 1995. De-noising by soft-thresholding. IEEE transactions on information theory 41(3):613-627.
175. Hyberts, S. G., A. G. Milbradt, A. B. Wagner, H. Arthanari, and G. Wagner. 2012. Application of iterative soft thresholding for fast reconstruction of NMR data non-uniformly sampled with multidimensional Poisson Gap scheduling. Journal of Biomolecular NMR 52(4):315-327.
176. Donoho, D. L. 2006. Compressed sensing. IEEE Transactions on information theory 52(4):1289-1306.
177. Shchukina, A., P. Kasprzak, R. Dass, M. Nowakowski, and K. Kazimierczuk. 2016. Pitfalls in compressed sensing reconstruction and how to avoid them. Journal of Biomolecular NMR:1-20.
178. Rovnyak, D., J. Hoch, A. Stern, and G. Wagner. 2004. Resolution and sensitivity of high field nuclear magnetic resonance spectroscopy. Journal of Biomolecular NMR 30(1):1-10.
179. Palmer, M. R., C. L. Suiter, G. E. Henry, J. Rovnyak, J. C. Hoch, T. Polenova, and D. Rovnyak. 2015. Sensitivity of nonuniform sampling NMR. The Journal of Physical Chemistry B 119(22):6502-6515.
180. Stetz, M. A., and A. J. Wand. 2016. Accurate determination of rates from non-uniformly sampled relaxation data. Journal of biomolecular NMR 65(3-4):157-170.
181. Melacini, G., R. Boelens, and R. Kaptein. 1999. Water-macromolecule interactions by NMR: a quadrature-free constant-time approach and its application to CI2. J Biomol NMR 15(3):189-201.
182. Dalvit, C. 1996. Homonuclear 1D and 2D NMR Experiments for the Observation of Solvent–Solute Interactions. Journal of Magnetic Resonance, Series B 112(3):282-288.
183. Denisov, V. P., G. Carlström, K. Venu, and B. Halle. 1997. Kinetics of DNA hydration. Journal of molecular biology 268(1):118-136.
184. Melacini, G., R. Boelens, and R. Kaptein. 1999. Band-selective editing of exchange-relay in protein-water NOE experiments. Journal of Biomolecular NMR 13(1):67-71.
185. Melacini, G., R. Kaptein, and R. Boelens. 1999. Editing of chemical exchange-relayed NOEs in NMR experiments for the observation of protein–water interactions. Journal of Magnetic Resonance 136(2):214-218.
186. Cai, S., S. Y. Stevens, A. P. Budor, and E. R. Zuiderweg. 2003. Solvent interaction of a Hsp70 chaperone substrate-binding domain investigated with water-NOE NMR experiments. Biochemistry 42(38):11100-11108.
187. Adrover, M., G. Martorell, S. R. Martin, D. Urosev, P. V. Konarev, D. I. Svergun, X. Daura, P. Temussi, and A. Pastore. 2012. The role of hydration in protein stability: comparison of the cold and heat unfolded states of Yfh1. Journal of Molecular Biology 417(5):413-424.
188. Geen, H., and R. Freeman. 1991. Band-selective radiofrequency pulses. Journal of Magnetic Resonance 93(1):93-141.
189. Zwahlen, C., S. J. F. Vincent, L. Di Bari, M. H. Levitt, and G. Bodenhausen. 1994. Quenching spin diffusion in selective measurements of transient overhauser effects in nuclear magnetic resonance. Applications to oligonucleotides. Journal of the American Chemical Society 116(1):362-368.
190. Denisov, V. P., and B. Halle. 1995. Hydrogen exchange and protein hydration: the deuteron spin relaxation dispersions of bovine pancreatic trypsin inhibitor and ubiquitin. Journal of Molecular Biology
245(5):698-709.

191. Denisov, V. P., and B. Halle. 1995. Protein hydration dynamics in aqueous solution: a comparison of bovine pancreatic trypsin inhibitor and ubiquitin by oxygen-17 spin relaxation dispersion. Journal of Molecular Biology 245(5):682-697.
192. Makarov, V., B. M. Pettitt, and M. Feig. 2002. Solvation and hydration of proteins and nucleic acids: a theoretical view of simulation and experiment. Accounts of chemical research 35:376-384.
193. Fogarty, A. C., and D. Laage. 2014. Water Dynamics in Protein Hydration Shells: The Molecular Origins of the Dynamical Perturbation. The Journal of Physical Chemistry B 118(28):7715-7729.
194. Sattler, M., J. Schleucher, and C. Griesinger. 1999. Heteronuclear multidimensional NMR experiments for the structure determination of proteins in solution employing pulsed field gradients. Progress in Nuclear Magnetic Resonance Spectroscopy 34:93-158.
195. Baryshnikova, O. K., T. C. Williams, and B. D. Sykes. 2008. Internal pH indicators for biomolecular NMR. J Biomol NMR 41(1):5-7.
196. Marion, D., L. E. Kay, S. W. Sparks, D. A. Torchia, and A. Bax. 1989. Three-dimensional heteronuclear NMR of nitrogen-15 labeled proteins. Journal of the American Chemical Society 111(4):1515-1517.
197. Kasinath, V., K. G. Valentine, and A. J. Wand. 2013. A 13C labeling strategy reveals a range of aromatic side chain motion in calmodulin. Journal of the American Chemical Society 135(26):9560-9563.
198. Ayala, I., R. Sounier, N. Usé, P. Gans, and J. Boisbouvier. 2009. An efficient protocol for the complete incorporation of methyl-protonated alanine in perdeuterated protein. Journal of Biomolecular NMR 43(2):111-119.
199. Gelis, I., A. M. J. J. Bonvin, D. Keramisanou, M. Koukaki, G. Gouridis, S. Karamanou, A. Economou, and C. G. Kalodimos. 2007. Structural Basis for Signal-Sequence Recognition by the Translocase Motor SecA as Determined by NMR. Cell 131(4):756-769.
200. Tugarinov, V., and L. E. Kay. 2003. Ile, Leu, and Val Methyl Assignments of the 723-Residue Malate Synthase G Using a New Labeling Strategy and Novel NMR Methods. Journal of the American Chemical Society 125(45):13868-13878.
201. Fathi, H., J. P. Kelly, V. R. Vasquez, and O. A. Graeve. 2012. Ionic Concentration Effects on Reverse Micelle Size and Stability: Implications for the Synthesis of Nanoparticles. Langmuir 28(25):9267-9274.
202. Shortle, D., W. E. Stites, and a. K. Meeker. 1990. Contributions of the large hydrophobic amino acids to the stability of staphylococcal nuclease. Biochemistry 29:8033-8041.
203. Xu, Y., Z. Lin, C. Ho, and D. Yang. 2005. A General Strategy for the Assignment of Aliphatic Side-Chain Resonances of Uniformly 13C,15N-Labeled Large Proteins. Journal of the American Chemical Society 127(34):11920-11921.
204. Hyberts, S. G., H. Arthanari, and G. Wagner. 2012. Applications of non-uniform sampling and processing. Topics in Current chemistry 316:125-148.
205. Goddard, T. D., Kneller, D.G. SPARKY 3. University of California, San Francisco, CA.
206. DeLano, W. L. 2009. The PyMOL molecular graphics viewing system. Delano Scientific LLC, Palo Alto, CA.
207. Palmer, A. G. r., J. Cavanagh, P. E. Wright, and M. Rance. 1991. Sensitivity improvement in proton-detected two-dimensional heteronuclear correlation NMR spectroscopy. Journal of Magnetic Resonance 93(1):151-170.
208. Delaglio, F., S. Grzesiek, G. W. Vuister, G. Zhu, J. Pfeifer, and A. Bax. 1995. NMRPipe: a multidimensional spectral processing system based on UNIX pipes. Journal of Biomolecular NMR 6(3):277-293.
209. Rahi, S. J., and K. Sharp. 2006. Mapping Complicated Surfaces onto a Sphere. International Journal of Computational Geometry and Applications 17:305-329.